
Novae a theoretical and observational study

Monika D. Soraisam



München 2016

Novae **a theoretical and observational study**

Monika D. Soraisam

Dissertation
an der Fakultät für Physik
der Ludwig-Maximilians-Universität
München

vorgelegt von
Monika D. Soraisam
aus Imphal, Manipur, Indien

München, den 26. Februar 2016

Erstgutachter: Prof. Dr. Rashid Sunyaev
Zweitgutachter: Prof. Dr. Gerhard Börner
Tag der mündlichen Prüfung: 31. Mai 2016

Contents

Zusammenfassung	xi
Summary	xiv
1 Introduction	1
1.1 Novae	1
1.1.1 Evolution of CVs	2
1.1.2 Theory of nova explosions	5
1.1.3 Progress of the nova	6
1.2 SNe Ia and the enigma of their progenitors	7
1.2.1 Single degenerate scenario	9
1.2.2 Double degenerate and other scenarios	11
1.3 Scope for novae in modern time-domain surveys	12
2 Constraining the role of novae as progenitors of type Ia supernovae	13
2.1 Introduction	13
2.2 Relation between supernova and nova rates	14
2.3 Statistics of novae in M31	18
2.3.1 SN Ia rate in M31	18
2.3.2 Nova rate in M31	19
2.3.3 Contribution of novae to the SN Ia rate	20
2.3.4 Fast novae	22
2.4 Temporal sampling and completeness of nova surveys	22
2.5 Discussion	27
2.6 Conclusions	32
3 Upper limits on mass accumulation by white dwarfs in the unstable nuclear burning regime	35
3.1 Introduction	35
3.2 Derivation of $f(M_{\text{WD}})$	35
3.3 Incompleteness correction of Arp's survey of M31 (1953-1955)	36
3.4 Nova rate distribution in M31	38

3.5	Constraints on mass accumulation in the nova regime using the M31 nova sample	39
3.6	Summary	40
4	Populations of post-nova supersoft X-ray sources	41
4.1	Introduction	41
4.2	WD mass distribution in novae in M31	43
4.3	Post-outburst SSS phase of Novae	46
4.4	Post-nova SSS population in M31	47
4.4.1	Luminosity function	51
4.4.2	Effective temperature distribution	54
4.5	Comparison with <i>XMM-Newton</i> observations of M31	56
4.6	Discussion	57
4.7	Summary and conclusions	60
5	A novel method for transient detection in high-cadence optical surveys and its application for a systematic search for novae in M31	63
5.1	Introduction	63
5.2	iPTF M31 data	66
5.3	Spatial recurrence map of the raw detections	67
5.4	The method	69
5.4.1	Source detection using WAVDETECT	69
5.4.2	Applicability of WAVDETECT	72
5.4.3	Characteristics of WAVDETECT detections in the time-domain context	75
5.5	A systematic search for novae in the iPTF M31 observations	79
5.5.1	Lightcurve construction via forced photometry	79
5.5.2	Lightcurve filtering for novae	80
5.6	Results	82
5.7	Discussion	86
5.8	Summary	87
6	Conclusions and outlook	89
A	A quick primer of the expansion of the universe	93
B	Nova light-curve template	95
C	Peak magnitudes of novae	101
	Bibliography	105
	Acknowledgments	120

List of Figures

1.1	Artist's impression of a CV	2
1.2	Stability conditions for the hydrogen shell burning on the WD surface . . .	10
2.1	Variation of the ignition mass of the nova and the mass-loss timescale with the mass of the WD	15
2.2	Cumulative and differential t_2 distributions of novae produced by a successful SN Ia progenitor	17
2.3	Maximal contribution of novae to the SN Ia rate of M31 as a function of assumed mass accretion rate	21
2.4	Detection efficiency for novae in M31 as a function of their decline time t_2 .	23
2.5	Cumulative detection efficiency of fast novae with $t_2 \leq 10$ days in M31 . .	26
2.6	Comparison of the ignition mass of nova computed by different authors . .	28
2.7	Comparison of observed maximum-magnitude rate-of-decline relation with the results of multicycle nova models of Yaron et al. (2005)	29
3.1	Detection efficiency η of Arp's survey of M31 (1953-1955)	37
3.2	Observed differential nova rate distribution in M31	38
3.3	Constraints on the fraction of mass that can be accreted in the nova regime at different WD masses	40
4.1	Theoretical decline time t_2 of novae as a function of the WD mass from Yaron et al. (2005)	44
4.2	(<i>left panel</i>) The inferred WD mass distribution in novae in M31 using the nova samples of Arp (1956) and Darnley et al. (2004) and (<i>right panel</i>) assumed theoretical WD mass distributions in novae	45
4.3	(<i>left panel</i>) Evolution of the post-nova (unabsorbed) soft X-ray luminosity in the 0.2-1.0 keV band for different WD masses. (<i>right panel</i>) Peak soft X-ray luminosity of the light curves as a function of the WD mass	48
4.4	(<i>left panel</i>) Evolution of the effective temperature (T_{eff}) of post-nova SSSs from the nova evolutionary tracks of Wolf et al. (2013). (<i>right panel</i>) Peak effective temperature as a function of the WD mass	49
4.5	Cumulative (<i>left panel</i>) and differential (<i>right panel</i>) luminosity functions of the post-nova SSSs in M31 for the different WD mass distribution models .	52

4.6	Cumulative effective temperature distribution of post-nova SSSs in M31 with unabsorbed luminosity $L_x \gtrsim 10^{36}$ erg/s (<i>left panel</i>) and the corresponding differential distribution (<i>right panel</i>)	53
4.7	Effective temperature – luminosity plot for the post-nova SSSs in M31 . . .	55
5.1	A section of a typical M31 field difference image from the iPTF pipeline, containing the bulge	64
5.2	The outer part, half a degree northward of the center of M31, of the typical difference image from the iPTF pipeline	65
5.3	Distribution of the observation epochs of the iPTF M31 data	66
5.4	The number of sources detected by the iPTF DI pipeline against the difference image number for the M31 field	67
5.5	The spatial recurrence image zoomed in on the bulge of M31	68
5.6	The outer part of the spatial recurrence image, about half a degree northward of the center of M31	70
5.7	The hits image formed by registering the total number of occurrences of any raw detection in the M31 field from the iPTF DI pipeline	71
5.8	The hits image zoomed in on the bulge with the WAVDETECT sources	73
5.9	The outer part of the hits image, half a degree northward of the M31 center, with the WAVDETECT sources	74
5.10	Background pixel value distribution of the hits image	76
5.11	Distribution of counts in the source regions for the detections made by WAVDETECT	77
5.12	Distribution of the magnitudes for the sources detected in the reference image and those WAVDETECT sources with counterparts in the reference image	78
5.13	Examples of lightcurves of the candidates constructed via forced photometry using DAOPHOT	81
5.14	Lightcurves of the eight candidates obtained from the nova selection algorithm	83
5.15	Lightcurve obtained using DAOPHOT for the candidate at the position of missed nova M31N 2013-10b	85
B.1	Raw (<i>left panel</i>) and transformed (<i>right panel</i>) light curves of the Galactic nova sample selected from the S class of the catalog compiled by Strobe et al. (2010)	96
B.2	Raw (<i>left panel</i>) and transformed (<i>right panel</i>) light curves of the M31 nova sample from the WeCAPP catalog	97
B.3	Raw (<i>left panel</i>) and transformed (<i>right panel</i>) light curves of the M31 nova sample from the PTF catalog	98
B.4	Co-aligned template light curves from the three different nova samples . . .	99
C.1	Relation between the maximum magnitude and the rate of decline for extragalactic novae.	102

List of Tables

4.1	Models of the WD mass distribution in novae	43
4.2	Theoretical nova rate for the different WD mass distribution models.	50
4.3	Monte Carlo simulation results for different models of WD mass distribution in novae in M31	56
5.1	Summary of WAVDETECT detections	79
5.2	iPTF recovery of M31 novae reported between 09/2013 and 01/2014	84
C.1	Mean nova peak magnitudes and their standard deviations	103

Zusammenfassung

Die vorliegende Arbeit präsentiert Studien von Novae, die sowohl theoretische als auch Beobachtungsaspekte beinhalten. Da Novae auf Weißen Zwergen (WZn) beheimatet sind, wurde Interesse an ihnen im Zusammenhang mit möglichen Vorgängern von Supernovae der Klasse Ia (SNe Ia) generiert. Bei einer Novaexplosion wird der WZ nicht zerstört. Stattdessen stellt er nach dem optischen Ausbruch weiterhin durch stabile Nukleosynthese innerhalb des übriggebliebenen Wasserstoffmantels Energie zur Verfügung. Demzufolge verschiebt sich das elektromagnetische Spektrum der Novaemission zu höheren Energien, bei denen diese länger anhält als im optischen Bereich. Eine Konsequenz ist, dass die Mehrheit der beobachteten superweichen Röntgenquellen als Novae identifiziert werden konnten. Diese Tatsache ist für die Galaxie M31 besonders stark gesichert.

Für hohe Massenakkretionsraten innerhalb des instabilen Nukleosyntheseregimes (oder Novaregimes) gibt es Hinweise darauf, dass der WZ signifikant an Masse gewinnen kann. Dies bereitet den Weg für SN Ia-Vorgängermodelle innerhalb des einfach degenerierten (ED) Szenarios, die Novae beinhalten. Aufbauend auf der Statistik von Novae in M31, dem am häufigsten benutzten Ziel für Novadurchmusterungen, untersuchen wir die mögliche Rolle von Novae bei der Produktion von SNe Ia. Unter Zuhilfenahme von multizyklischen Novaevolutionsmodellen und der beobachteten Novarate in M31, schätzen wir die höchstmögliche Rate von SNe Ia ab, die Novae produzieren können, wenn man annimmt, dass alle involvierten WZe die Chandrasekhar-Masse erreichen. Der Vergleich dieser Rate mit der von Beobachtungen abgeleiteten Rate von SNe Ia in M31 schränkt den möglichen Beitrag des Novakanals zur SN Ia-Rate auf weniger als 2–7% ein.

Zudem zeigen wir, dass eine genauere Diagnose mit der Statistik von schnellen Novae, die sich durch Abklingzeiten von $t_2 \lesssim 10$ Tage auszeichnen, gestellt werden kann. Die meisten Novae auf einem typischen ED SN Ia-Vorgänger, der innerhalb des Novaregimes akkretiert, sind schnell. Da der WZ innerhalb des Novaregimes an Masse gewinnt, produziert er insbesondere immer häufiger Novae und mit sinkenden Abklingzeiten. Deshalb untersuchen wir wie effizient schnelle Novae in Novadurchmusterungen von M31 mit einem Teleskop der PTF-Klasse (Palomar Transient Factory) detektiert werden können, mit dem Ziel Voraussetzungen für zukünftige Vermessungen mit hoher Kadenz, die auf Novae abzielen, zu formulieren. Wir finden heraus, dass eine Durchmusterung mit einer limitierenden Magnitude von $m_R \approx 22$ und Beobachtungen mindestens jede zweite Nacht etwa 90% der innerhalb des ED-Szenarios erwarteten schnellen Novae detektiert. Bezeichnen wir den Anteil der SNe Ia, der die letzte Zehntel-Sonnenmasse vor der SN Ia-Explosion innerhalb

des Novaregimes ansammelt, als f , dann sollten solche Durchmusterungen in M31 in etwa $1000 \times f$ schnelle Novae pro Jahr detektieren.

Die Population der schnellen Novae, auf deren Bedeutung oben hingewiesen wurde, ist bis heute für keine Galaxie gemessen. Sie fehlt auch in der neuesten gemessenen Rate für M31. Für eine erste Näherung verwenden wir eine ältere Vermessung von M31 durch Arp (1956), um den Bereich der WZ-Population mit hohen Massen zu untersuchen, der eine Rolle für Novae spielt. Innerhalb des ED-Szenarios ist es möglich, dass ein SN Ia-Vorgänger verschiedene Nukleosyntheseregime durchläuft (stabiles, instabiles, und Windregime). Durch den Vergleich der beobachteten WZ-Massenverteilung in Novae mit der durch das ED-Szenario vorhergesagten erhalten wir Grenzen für den Anteil der Masse, der von einem SN Ia-Vorgänger innerhalb des Novaregimes angesammelt werden kann. Für kleine WZ-Massen ($\lesssim 1.30 M_{\odot}$) ist eine signifikante Massenakkretion innerhalb des Novaregimes, von der Größenordnung 10–60%, möglich. Für massereichere WZe verengen sich die Grenzen für Massenansammlung innerhalb dieses Regimes auf $\sim 2\%$.

Gegeben die länger anhaltende Signatur der Novaexplosion im weichen Röntgenstrahlungsbereich, untersuchen wir im nächsten Schritt die Population der superweichen Röntgenquellen in M31, die nach einer Nova entstehen. Hierfür benutzen wir theoretische Modelle für die Evolution der Systeme nach der Novaexplosion. Abhängig von der WZ-Massenverteilung in Novae, erhalten wir zu jedem Zeitpunkt 250–600 post-Nova Röntgenquellen mit Leuchtkräften von $L_X \geq 10^{36}$ erg/s bei Photonenenergien von 0.2–1.0 keV, wenn wir Absorption ignorieren. Ihre kombinierte Leuchtkraft beträgt etwa 10^{39} erg/s. Ferner leiten wir die Verteilungen ihrer Leuchtkräfte und effektiven Temperaturen her. Die erstere zeigt eine signifikante Verteilung bei $\log(L_X) \sim 37.7\text{--}38$ mit einer Kante bei $\approx 2 \times 10^{38}$ erg/s. Die letztere Verteilung ist in etwa ein Potenzgesetz mit einem Exponenten 4–6 bis zu einer maximalen effektiven Temperatur von $\approx 1.5 \times 10^6$ K. Wir vergleichen unsere Vorhersagen mit dem beobachteten Resultat der *XMM-Newton*-Messung der zentralen Region von M31 und finden eine gute Übereinstimmung.

Um die Population der schnellen Novae in M31 zu charakterisieren, unternehmen wir eine Analyse der Daten von M31, die von der intermediate Palomar Transient Factory (iPTF) gemessen wurden. Zu diesem Zweck entwickeln wir eine neue Methode für die effiziente Detektion von Kandidaten für vergängliche und variable Quellen in den Ergebnissen von Datenanalysepipelines in der Zeitdomäne, wobei wir die Kontamination durch Artefakte signifikant reduzieren. Die Methode ist besonders relevant um Regionen handhaben zu können, die mit fehlerhaften Detektionen aus den Datenanalysepipelines dicht bevölkert sind, wie zum Beispiel die Bulge von Galaxien und die galaktische Ebene.

Zur Illustration der Methode verwenden wir fünfmonatige iPTF-Beobachtungen von M31, die den Bulge beinhalten. Die iPTF-Datenanalysepipeline produziert $\sim 10^5$ Detektionen in den Differenzbildern dieser Beobachtungen, wobei mehrfache Detektionen der selben Quelle enthalten sind. Nachdem wir diese Detektionen auf ein leeres Bild der analysierten Region projizieren, erhalten wir ein Analogon zu einer astronomischen Röntgenaufnahme. In diesem Bild erscheinen die Kandidaten für variable Quellen als lokale Anhäufungen von rohen Detektionen, umgeben von einem Hintergrund aus Artefakten. Wir benutzen einen waveletbasierten Algorithmus namens WAVDETECT, der für die Analyse

von *Chandra*-Daten entwickelt wurde, um die einzelnen Kandidaten für variable Quellen zu identifizieren. Wir wenden unsere Methode für eine systematische Suche nach Novae in M31 an. Hierfür erstellen wir die Lichtkurven aller Kandidaten und verwenden dann einen Lichtkurvenselektionsalgorithmus, basierend auf den erwarteten Eigenschaften von Novae. Wir finden acht Novakandidaten, die wir alle als tatsächliche Novae bestätigen können.

Die Implementierung unserer Methode, inklusive der Lichtkurvenselektion, ist automatisch, was es möglich macht den Grad der Vollständigkeit der resultierenden Quellen zu quantifizieren. Dies wird in der Zukunft, nach der Analyse eines etwa zehnmal größeren Datensatzes von M31, geschehen. Unsere Methode wird somit die Suche nach Novae, insbesondere nach schnellen Novae, inklusive einer Vollständigkeitsanalyse ermöglichen. Die abgeleiteten Raten werden es uns ermöglichen, stärker einzuschränken welche Rolle Novae im Kontext von SN Ia-Vorgängern spielen und eine verlässlichere Verteilung der WZ-Massen am massereichen Ende zu erhalten.

Summary

In this thesis, we present studies relating to novae that include both theoretical and observational aspects. Being hosted by accreting white dwarfs (WDs), they have drawn attention in the context of the supernova Ia (SN Ia) progenitor problem. In the case of the nova explosion, the WD host is not disrupted. Instead, it continues to supply energy, even after the optical outburst, via stable nuclear burning of the remnant hydrogen envelope that survived the outburst. Accordingly, nova emission progresses toward the harder part of the electromagnetic spectrum, where it lasts longer than in the optical regime. As a consequence, novae are found to constitute the majority of the observed supersoft X-ray sources (SSSs). This is particularly well established for the galaxy M31.

For high mass accretion rates in the unstable nuclear burning regime (or nova regime), there is evidence that significant mass accumulation by the WD is possible. This paved the way for SN Ia progenitor models in the single degenerate (SD) scenario involving novae. Based on the statistics of novae in M31, which is the most frequently used target for nova surveys, we investigate the role that novae may play in producing SNe Ia. Using multicycle nova evolution models and the observationally inferred nova rate in M31, we estimate the maximal SN Ia rate that novae can produce, assuming that all of the involved WDs reach the Chandrasekhar mass. Comparing this rate to the observationally inferred SN Ia rate for M31 constrains the contribution of the nova channel to the SN Ia rate to $\lesssim 2\text{--}7\%$.

Additionally, we demonstrate that a more powerful diagnostic can be obtained from statistics of fast novae, which are characterized by decline times $t_2 \lesssim 10$ days. Most novae resulting from a typical SD SN Ia progenitor accreting in the nova regime are fast. Specifically, as the WD in the nova grows in mass, it produces novae more frequently and with decreasing decline times. We therefore investigate how efficiently fast novae can be detected in nova surveys of M31 by a PTF (Palomar Transient Factory) class telescope, with the aim to formulate requirements for future high-cadence surveys directed toward fast novae. We find that a survey with a limiting magnitude of $m_R \approx 22$, detects $\approx 90\%$ of fast novae expected in the SD scenario, with observations at least every second night. If f is the fraction of SNe Ia accreting in the nova regime for accumulation of the final tenth of a solar mass preceding the SN Ia explosion, then such surveys should be detecting fast novae in M31 on the order of $\gtrsim 1000 \times f$ per year.

The population of fast novae, whose importance has been highlighted above, is to date unconstrained for any galaxy. Most recent nova rate measurement in M31 is also devoid of them. However, for a first approximation, we make use of an older survey of M31 by Arp

(1956), to probe the high-mass end of the WD population involved in novae. In the context of the SD scenario, it is possible for a SN Ia progenitor to pass through different nuclear burning regimes (stable, unstable, and wind regimes). Comparing the observed WD mass distribution in novae with that predicted for the SD scenario, we obtain constraints on the fraction of mass that can be accumulated in the nova regime by the SN Ia progenitor. For low WD masses ($\lesssim 1.30 M_{\odot}$), significant mass accumulation, at the level of 10–60%, is possible in the nova regime. For the more massive WDs, the constraints tighten to $\sim 2\%$ for mass accumulation in this regime.

Given the longer-lasting electromagnetic signature of the nova explosion in the soft X-ray regime, we venture into exploring the population of post-nova SSSs in M31. To this end, we make use of theoretical post-nova evolution models. Depending on the assumed WD mass distribution in novae, we obtain at any instant 250–600 post-nova SSSs with a luminosity of $L_x \geq 10^{36}$ erg/s at photon energies of 0.2–1.0 keV, ignoring absorption. Their combined luminosity is of the order of 10^{39} erg/s. We also derive the distributions of their luminosities and effective temperatures. The former exhibits a significant steepening at $\log(L_x) \sim 37.7\text{--}38$ with a cut-off at $\approx 2 \times 10^{38}$ erg/s. The latter distribution is roughly a power law with logarithmic differential slope 4–6 up to the maximum effective temperature of $\approx 1.5 \times 10^6$ K. We compare our predictions with the observational results of the *XMM-Newton* monitoring of the central region of M31, obtaining a good agreement.

To characterize the population of fast novae in M31, we undertake an analysis of the M31 data from the intermediate Palomar Transient Factory (iPTF) Survey. In this pursuit, we develop a new method for efficiently detecting candidates for transients and variable sources from the outputs of time-domain data pipelines, significantly reducing the contamination by artifacts. The method is particularly relevant for handling regions that are crowded by a large number of false detections from the data pipelines, such as the bulges of galaxies and the Galactic plane.

To illustrate the methodology, we use iPTF M31 observations, with a baseline of five months, covering the bulge. The iPTF pipeline produces $\sim 10^5$ detections from the difference images of these observations, including multiple detections from the same source. Projecting these raw detections onto a blank image of the analyzed field, we obtain an analogue of an X-ray image. In this image, the candidates for variable sources appear as clusters of raw detections on top of a background of artifacts. We then make use of a wavelet-based tool called **WAVDETECT**, developed for the analysis of *Chandra* data, to identify the unique candidates for variable sources. We apply our method to conduct a systematic search for novae in M31. To this end, we construct lightcurves of all candidates and apply a lightcurve selection algorithm based on the expected properties of novae. We find eight nova candidates, which we have verified to be confirmed novae in all cases.

The implementation of our method, including the lightcurve selection, is automated, which makes it possible to quantify the sample completeness. This will be done in the future, following the analysis of a ~ 10 -fold larger iPTF data set. Our method will thus facilitate the search for novae, in particular fast ones, including a completeness estimate. The derived rates will enable us to put more stringent constraints on the role novae play in the context of SN Ia progenitors, and to obtain a more reliable WD mass distribution

in novae at the massive end.

Chapter 1

Introduction

In this thesis, we present the study of various aspects of novae, from both theoretical and observational perspectives. We address one of the important propositions put forth concerning novae, with relevance extending to supernova Ia (SN Ia) cosmology, that novae could be one of the elusive progenitors of SNe Ia – that they can explain the SN Ia rates in galaxies. Further, we explore their population in different regimes of the electromagnetic spectrum, particularly in the optical and the soft X-rays. We undertake a major initiative analyzing data from one of the most important present-day optical surveys in the time domain, to uncover the population of fast novae, the importance of which will be elucidated in the course of the following chapter. During this pursuit, we formulate a novel method for efficient detection of transients in high-cadence optical surveys.

Through this introductory chapter, we lay the premises for the work presented in the remainder of the thesis. We give a brief summary of the origin and evolution of nova systems, the mechanism of the nova outbursts and their consequent electromagnetic imprints. We further go over the aspects of SNe Ia, in particular their progenitor problem, in connection to novae. We end the chapter outlining the prospects of novae in the present ripe era of time-domain astronomy.

1.1 Novae

When making astronomical observations, using even the least powerful telescopes such as ones operated by amateur astronomers, a class of events that are transient in nature and yet make frequent appearances are novae. Certainly facilitating this feat are their high luminosities, around 10^4 – $10^5 L_{\odot}$. Novae¹ are the best-known and the grandest among the variability phenomena manifested by objects known as cataclysmic variables (CVs; Warner 1995). CVs are close binaries consisting of a white dwarf (WD; the primary component) and a low-mass companion star (the secondary component) that fills its Roche-lobe. As the material overflowing the Roche-lobe from the secondary star has angular momentum,

¹It is to be noted that the term novae is used to refer both to the astrophysical event as well as the object exhibiting the event; in either case, the context makes it clear.

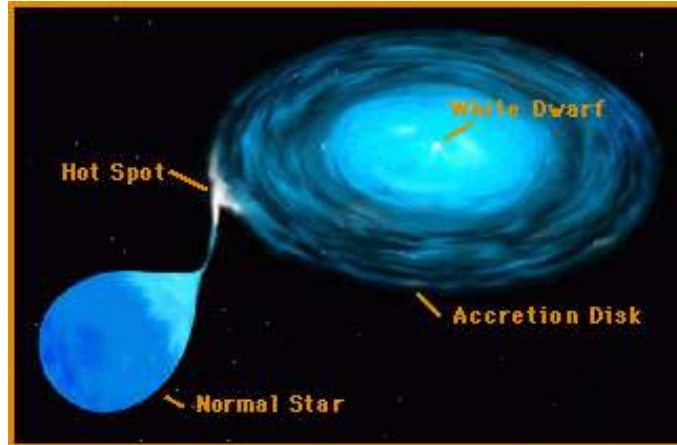


Figure 1.1: Artist’s impression of a CV. Shown are the WD, its companion star, and the accretion disk. The hot spot is where the stream of material from the secondary star impacts the accretion disk. (Image credit: NASA)

it is transported on to the WD via an accretion disk (see Fig. 1.1). In Sect. 1.1.1, we briefly summarize the evolution of these systems, thus preparing the ground for describing the physical process, namely thermonuclear runaway, that produces the nova phenomenon. The latter is detailed in Sect. 1.1.2. We note that there are also symbiotic novae (see Mikolajewska 2010), where the underlying systems are interacting binaries containing a WD that accretes mass from the wind of an evolved secondary (a red giant or asymptotic giant branch, AGB, star). There are, however, only a very small number of these symbiotic novae, and therefore we do not discuss the evolution of symbiotic systems here. Moreover, for this thesis work, what is important is the physical process responsible for the nova phenomenon (that will become clear in the following chapters), which is the same in symbiotic novae (and hence their name).

Novae, being a relatively commonly occurring phenomenon in the astrophysical universe, provide an ideal observatory for consolidating the theoretical understanding of various aspects of astrophysics, like binary evolution (Iben & Tutukov 1984b), mass accretion onto compact objects (Nariai et al. 1980), thermonuclear runaways (Starrfield et al. 1972), enrichment of the interstellar medium (Gehrz et al. 1998), in particular with lithium (Tajitsu et al. 2015). Most importantly, with the realization that some of the WDs in nova systems have very large masses, much attention has been drawn by these objects, particularly in the context of the SN Ia progenitor problem. In this regard, we discuss various important aspects of SNe Ia and their progenitor models in Sect. 1.2.

1.1.1 Evolution of CVs

It is generally believed that the progenitors of CVs are binaries, in which, following a common envelope event (see Taam & Sandquist 2000 for a review on the common envelope process), the initially more massive primary is converted into a WD and the binary separa-

tion is reduced to a distance comparable to a solar radius, R_{\odot} . Subsequently, the evolution of a CV, in particular the transfer of mass from the secondary star on to the primary WD, is driven by angular momentum loss (Warner 1995; Bode & Evans 2008). This process affects the orbital periods of the CVs, and accordingly their orbital period distribution provides a way to probe the evolution of CVs. The distribution is characterized by two notable features – the so-called period gap at $\sim 2\text{--}3$ hr, and a sharp cut-off at ~ 80 min called the period minimum. The existence of these features is incorporated within the standard model of CV evolution (Knigge 2011). We closely follow Bode & Evans (2008) and Knigge (2011) in the following discussion.

For a binary system, the orbital angular momentum, J_{orb} , is given by

$$J_{\text{orb}} = M_1 M_2 \left(\frac{Ga}{M_1 + M_2} \right)^{1/2}, \quad (1.1)$$

where M_1 and M_2 are the WD and secondary star mass, respectively, and a is their orbital separation. G is the gravitational constant. The Roche-lobe radius, R_{L} , for the secondary star relates to the orbital separation as (Iben & Tutukov 1984a)

$$R_{\text{L}} = 0.52 \left(\frac{M_2}{M_1 + M_2} \right)^{0.44} a. \quad (1.2)$$

The relation between the radius, R_2 , and mass of the donor/secondary star can be parameterized as (Iben & Tutukov 1984b)

$$R_2 = \rho M_2^{1-\epsilon}, \quad (1.3)$$

where ρ and ϵ are parameters to be determined by fitting to observations.

We assume that all the mass lost by the secondary star is accreted by the WD. Setting $R_{\text{L}} = R_2$ and using Eqs. (1.2) and (1.3) in (1.1), we obtain the rate of change of the orbital angular momentum of the binary as

$$\frac{\dot{J}_{\text{orb}}}{J_{\text{orb}}} = \frac{\dot{M}_2}{M_2} \left(1.28 - \frac{\epsilon}{2} - \frac{M_2}{M_1} \right). \quad (1.4)$$

All close binaries lose angular momentum due to gravitational wave radiation (GWR) at a rate given by (see Webbink 1976; Bode & Evans 2008)

$$-\frac{\dot{J}_{\text{GWR}}}{J_{\text{GWR}}} = \frac{32G^3}{5c^5} \frac{M_1 M_2 (M_1 + M_2)}{a^4}, \quad (1.5)$$

where c is the speed of light.

The mass transfer rate, \dot{M}_2 , driven by GWR alone is found not sufficient to explain the observed rates for systems above the period gap (Warner 1995); below the gap, it is considered to be the dominant mechanism. For CVs above the gap, magnetic braking (MB; see Knigge et al. 2011 for various models of the mechanism) has been invoked as

the main driver of angular momentum loss. The basic principle of magnetic braking is the following. Any low-mass star, the secondary star in the case of CVs, is associated with a magnetized stellar wind that siphons off the spin angular momentum, J_s , of the star. The latter results from the interaction between the stellar magnetic field and ionized particles in the wind that exerts a spin-down torque on the star. In the CV, the secondary star is tidally locked with the WD, and therefore the overall effect of the magnetized stellar wind from the donor is the loss of orbital angular momentum at the rate equal to $\dot{J}_{\text{MB}} = \dot{J}_s$.

One of the earliest and most popular recipes for MB is that by Verbunt & Zwaan (1981), which we briefly summarize in the following. The equatorial rotation speed of the low-mass star, obtained empirically by Skumanich (1972), is

$$v = ft^{-1/2}, \quad (1.6)$$

where t is the age of the star and f is the constant of proportionality. The spin angular momentum of the secondary star is given by

$$J_s = fk^2 M_2 R_2 t^{-1/2}, \quad (1.7)$$

where k is the radius of gyration of the secondary star. Differentiating this equation with respect to time, we obtain

$$\frac{\dot{J}_s}{J_s} \equiv \frac{\dot{J}_{\text{MB}}}{J_{\text{MB}}} = -\frac{v^2}{2f^2}. \quad (1.8)$$

Further, since the system is tidally locked, we have

$$v = \frac{R_2}{a} \left(\frac{G(M_1 + M_2)}{a} \right)^{1/2}. \quad (1.9)$$

From Eqs. (1.9) and (1.8), we finally have

$$-\frac{\dot{J}_{\text{MB}}}{J_{\text{MB}}} = \frac{GR_2^2(M_1 + M_2)}{2a^3 f^2}. \quad (1.10)$$

One can estimate the mass transfer rate, \dot{M} , from the secondary star to the WD in a CV using Eqs. (1.10) or (1.5), depending on whether it is above or below the period gap, respectively, in Eq. (1.4). Based on the observed orbital period distribution of novae, Townsley & Bildsten (2005) claim that in 50% of nova systems, $\dot{M} \simeq 10^{-9} M_\odot \text{ yr}^{-1}$, and the remaining 50% are distributed evenly between higher and lower values of \dot{M} . The period gap is thought to arise when the efficiency of MB drops sharply as the secondary star becomes fully convective when M_2 decreases to $\sim 0.2\text{--}0.3 M_\odot$. This happens at orbital periods of about 3 hr. Below the period gap, GWR becomes effective in removing the orbital angular momentum of the CV, driving the secondary star to come into contact with the Roche-lobe. The period minimum is attributed to the loss of thermal equilibrium caused by mass-loss in the secondary star that has become sub-stellar around this period (Knigge 2011). In this case, the radius of the secondary star stops shrinking in response to

mass-loss. This leads to an increase in the orbital period of the system in order to contain the secondary star (Bode & Evans 2008). Accordingly, at the period minimum, the systems bounce back, hence they are termed period bouncers, evolving back toward longer periods. The latter results in a spike at the period distribution around the minimum period with a sharp cut-off (Gänsicke et al. 2009).

1.1.2 Theory of nova explosions

At the mass accretion rates found in nova systems (cf. 1.2.1), the hydrogen-rich material transferred by the secondary star gets continually accumulated on the surface of the WD. Over a long period of time, the layer at the bottom of the accreted envelope is compressed by the strong surface gravity of the WD, eventually becoming electron-degenerate and thus setting the stage for a runaway once nuclear burning occurs in the layer. Thermonuclear runaway (TNR) in degenerate matter is a consequence of its equation of state, where pressure is independent of temperature. Since nuclear burning is more sensitive to temperature than density (see below), any slight perturbation to the temperature will enhance the burning without an increase in pressure such that the temperature gets further amplified, leading to a runaway process.

During the initial accretion phase in the nova system, the prevalent conditions of temperature, T , and density, ρ , at the base of the accreted envelope on the WD ensue nuclear burning through the proton-proton chain, whose energy generation rate, q , is given by (Prialnik 2000)

$$q \propto \rho T^4. \quad (1.11)$$

Once the temperature reaches $\sim 2 \cdot 10^7$ K, the CNO (carbon, nitrogen, oxygen) cycle takes over (Warner 1995), powering the final stages of the TNR. The energy generation rate for the CNO cycle is given by (Prialnik 2000)

$$q \propto \rho T^{16}. \quad (1.12)$$

The CNO cycle involves four proton captures and two β^+ decays (see Prialnik 2000). While the former is sensitive to temperature, the latter does not depend on external conditions. At very high temperatures ($\gtrsim 10^8$ K), the energy generation rate is limited by the decay times of unstable β^+ nuclei. Further, convection that develops in the burning layer, given the high temperature sensitivity of q (Eq. 1.12), extends to the surface, depositing the longer-lived (compared to the convective turn-over time scale of ~ 100 s; see Warner 1995) β^+ nuclei and bringing fresh CNO nuclei into the burning shell². Thus, the β^+ nuclei get mixed throughout the envelope and deposit the energy released from their decay. The runaway process is quenched once the temperature in the envelope reaches the Fermi temperature, where the equation of state turns into that of an ideal gas; at this stage, the degeneracy at the burning layer is lifted. Furthermore, the energy released from the β^+ decay causes the expansion of the envelope and ejection of material off the WD surface.

²There may also be dredge-up of CNO nuclei from the WD core. The mixing process is still an unresolved issue in nova theory (see Bode & Evans 2008).

Below, we derive a simplified relation for the ignition condition of a nova outburst, closely following (Prialnik 2000). As discussed above, TNR will be effected once the bottom layer (at some radius $r = r_b$) of the envelope attains electron degeneracy and nuclear burning is ignited. Let T_{ign} denote the ignition temperature. Then the temperature at the bottom layer T_b must satisfy $T_b \gtrsim T_{\text{ign}}$. When electron degeneracy is established in this layer, the ideal gas pressure becomes equal to that of degenerate gas. Therefore, at this layer we have

$$RT_b \left(\frac{\rho}{\mu_e} \right)_{r_b} \approx K \left(\frac{\rho}{\mu_e} \right)_{r_b}^{5/3}, \quad (1.13)$$

where R is the gas constant, ρ is the density, μ_e^{-1} is the mean number of free electrons per nucleon, and K is the constant of proportionality in the equation of state of the degenerate gas. This equation gives ρ/μ_e in terms of T_b . Then, putting $T_b = T_{\text{ign}}$, we obtain a relation for the critical pressure, P_{crit} , above which TNR develops,

$$P_{\text{crit}} \approx \frac{(RT_{\text{ign}})^{5/2}}{K^{3/2}}. \quad (1.14)$$

Putting in the values of the constants and setting $T_{\text{ign}} \sim 10^7$ K, we obtain $P_{\text{crit}} \sim 10^{18}$ dyn cm $^{-2}$ (Prialnik 2000). The envelope mass, M_{ign} , required to balance the pressure P_{crit} , that is the ignition mass for the nova outburst, can be estimated as (assuming the envelope thickness to be negligible)

$$P_{\text{crit}} \approx \frac{GM_{\text{WD}}M_{\text{ign}}}{4\pi R^4}, \quad (1.15)$$

where M_{WD} and R are the WD mass and radius, respectively. For the WD, $M_{\text{WD}} \propto R^{-3}$, and therefore we have from Eq. (1.15)

$$M_{\text{ign}} \propto M_{\text{WD}}^{-7/3}. \quad (1.16)$$

This equation implies that more massive WDs require smaller ignition mass for the nova outburst. Further, for a given mass accretion rate, \dot{M} , nova outbursts will recur after a time period given by $t_{\text{rec}} = M_{\text{ign}}/\dot{M}$. As \dot{M} is independent of the WD mass, more massive WDs will thus produce novae more frequently, the importance of which is discussed in detail in Chapter 2. In general, novae have been empirically classified as recurrent novae if their recurrence period t_{rec} is less than ~ 100 years.

It is to be noted that the above ignition condition, Eq. (1.15), is only a simplification; there are additional factors that influence the nova process. In particular, the mass accretion rate affects the ignition condition through compressional heating; on the other hand, a high intrinsic luminosity of the WD will lead to a quicker runaway, reducing the envelope mass required for ignition (Prialnik & Kovetz 1995).

1.1.3 Progress of the nova

At the peak of the TNR, the bolometric luminosity of the nova reaches the maximum value. At this stage, the envelope has expanded only slightly, such that the huge amount of luminosity ($\sim 10^4\text{--}10^5 L_\odot$) is being radiated through a small surface area. Accordingly, the effective temperature is of the order of $10^5\text{--}10^6$ K, and thus the nova emission peaks in the EUV and soft X-rays during this time. Furthermore, their luminosities at this stage approach or exceed the Eddington limit, which further aids in the hydrodynamic expansion of the envelope (Warner 1995). At maximum expansion, the envelope reaches a radius of $\sim 10\text{--}100 R_\odot$, and the effective temperature peaks in the visual. During this time, the nova resembles the planetary nebula phase in the evolution of an AGB star toward a WD, but with the direction of evolution reversed, and the nova follows the core mass-luminosity relationship (see Warner 1995). The bolometric luminosity after the nova outburst remains constant as a consequence of the invariance in the mass of the WD core. Some fraction of the envelope mass gets ejected during the initial expansion phase (specifically during the explosion); following this, mass from the envelope is believed to be continually lost through a wind, the mechanism of which is still uncertain. However, it is thought to be some combination of optically thick winds (Bath & Shaviv 1976; Kato & Hachisu 1994), super-Eddington winds (Shaviv 2001; Wolf et al. 2013), and frictional drag in the envelope due to the secondary star (MacDonald 1980). The decrease in the envelope mass shrinks its radius, revealing the deeper, hotter regions of the envelope. This results in the hardening of the spectrum. The decline in the visual luminosity is thus due to the redistribution of the flux to shorter wavelengths at constant bolometric luminosity. As a consequence, the novae become observable again as soft X-ray sources after their optical outburst. In Chapter 4, we explore the population of these post-nova soft X-ray sources.

In the following, we briefly outline the general trend of spectroscopic development in novae during the optical outburst phase, as was established by the influential work of Williams (1992). The nova spectra after the optical outburst can be traced through the emission lines that develop during the two stages of mass ejection (first discretely and then by winds, see above), with the central hot WD providing the energy for photoionization of the ejecta. Following the nova outburst, the characteristics of the later spectra are determined by which of the two groups of non-Balmer lines are strongest, FeII lines, or He/N lines. The Balmer lines themselves are generally the most intense lines in the spectra of all novae without distinction. The He/N lines are formed in the discrete ejecta, expelled during the outburst maximum, while the FeII lines are formed in the ejecta due to the subsequent winds. The FeII spectra evolve slowly, frequently show P-Cygni profiles (indicative of their formation in a wind), and exhibit typical expansion velocities < 2500 km/s. On the other hand, the He/N spectra evolve much faster, usually lack absorption components, and show expansion velocities typically > 2500 km/s. Depending on the parameters of the discrete ejecta and the wind, one of these emission line components will dominate the nova spectra. There are also some novae that do not conform to the above classification – a few evolve from one spectral class to the other, hence termed hybrids, and some show evidence for simultaneous emission from both components of the ejecta (see Williams 1992 for more

details).

1.2 SNe Ia and the enigma of their progenitors

SNe Ia, one of the most spectacular cosmic explosions, are characterized by the presence of a silicon absorption feature in their spectra around 6150 \AA , and absence of hydrogen and helium lines. These events boast of a vast amount of energy – near maximum optical light their luminosities reach $\sim 10^{43} \text{ erg/s}$ ($\sim 10 L_{\odot}$). The source of such energy is believed to be radioactive decay of ^{56}Ni , produced during the supernova nucleosynthesis, to ^{56}Co and the chain ending with the decay of ^{56}Co to stable ^{56}Fe (Colgate & McKee 1969). With the discovery of the nearest SN Ia to date, SN 2014J in M82 at a distance of $\approx 3.5 \text{ Mpc}$ (Fossey et al. 2014), a most conclusive piece of evidence in support of the above claim came through the detection of ^{56}Co in SN 2014J by Churazov et al. (2014), the first in any SN Ia.

SNe Ia are an important building-block in many astrophysical contexts. They are one of the main sources of chemical enrichment in the host galaxies, in particular iron enrichment given their iron yield of $\sim 0.7 M_{\odot}$ (Iwamoto et al. 1999). Besides their importance in the galactic chemistry, the enormous kinetic energy coupled to the explosion is one of the key players in regulating the gas dynamics in the host galaxy, bearing consequences for star formation and subsequently for the evolution of the galaxy (Davé et al. 2011). Further, the remnants of these explosions are considered to be the main candidates for accelerating cosmic rays, reaching energies of $\sim 10^{15} \text{ eV}$ (Helder et al. 2009).

However, no aspect has been as pivotal as the following in bringing SNe Ia into the limelight. This relates to one of the biggest discoveries of this century, not just in cosmology, but in the scientific world in general – that we are in a universe that is expanding at an accelerated rate. The cosmic expansion rate was traced using SNe Ia in the 2011 Nobel Prize-winning works of Perlmutter et al. (1999) and Riess et al. (1998). On this note, the key aspects of cosmology relevant for understanding its usage of SNe Ia are given in Appendix A.

The integral features of SNe Ia that facilitate their use in measuring the expansion rate of the universe are homogeneity of their emission and their high luminosity. The latter allows them to be detectable at distant galaxies. As regards the former, the luminosities of SNe Ia are not absolutely homogeneous per se; there are variations. However, there is a strong correlation between their luminosities and the width of the light curves, known as the Phillips relation (Phillips 1993), which allows their luminosities to be homogenized. As such, SNe Ia serve as standardizable candles – their intrinsic luminosities can be estimated. Subsequently, by measuring the flux (f) of the SN Ia, it is straightforward to obtain its luminosity distance (D_L) from the inverse-square-law formula as

$$D_L = \sqrt{\frac{L}{4\pi f}}, \quad (1.17)$$

where L is the luminosity of the SN Ia. The inverse-square-law formula takes the form

$$f = \frac{L/(1+z)^2}{4\pi r^2 a_0^2}, \quad (1.18)$$

in cosmology, where $a_0 = 1$ is the present-day scale factor, and r is the comoving distance (distance between objects measured along a path defined at the present time) to the SN Ia at redshift z , which can be calculated as

$$r = c \int_0^z \frac{dz'}{a_0 H(z')}, \quad (1.19)$$

with $H(z)$ given by the Friedmann equation, Eq. (A.12). Then, comparing Eqs. (1.17) and (1.19), we obtain

$$D_L(z) = a_0(1+z)r. \quad (1.20)$$

Substituting Eqs. (1.19) and (A.12) in Eq. (1.20), we finally obtain

$$D_L(z) = \frac{c(1+z)}{H_0} \int_0^z \frac{dz'}{\sqrt{\Omega_M(1+z')^3 + \Omega_{\text{rad}}(1+z')^4 + \Omega_{\text{DE}} e^{3 \int_0^z d \ln(1+z')(1+w_{\text{DE}}(z'))}}}. \quad (1.21)$$

The cosmological parameters appearing in the above equation are described in Appendix A. Thus, by measuring a large number of SNe Ia distributed at different redshifts, the cosmological parameters can be constrained.

This elegant use of SNe Ia, even though realized much earlier (Kowal 1968), could not be put to practice until the big-telescope boom happened, required to sample the high-redshift SNe Ia. At the present time, however, there is no dearth of SN Ia samples for cosmological use for a wide redshift range. Consequently, we are now at a time where systematic effects dominate statistics. One of the most important systematic uncertainties, which can in fact jeopardize the whole concept of SN Ia cosmology, is the fact that we do not yet know the progenitors of these explosions. This is, however, integral to ascertain that SNe Ia do not evolve with redshift. Of course, this issue of unresolved progenitors of SNe Ia is also important for the other astrophysical contexts, such as galactic evolution, as discussed above.

From the analysis of the observed SNe Ia, in particular their energies and chemical compositions, a broad agreement has emerged that a SN Ia is the thermonuclear explosion of a carbon-oxygen (CO) WD, whose source of ignition is considered to be mass accumulation, up to the Chandrasekhar mass (M_{ch}) limit (Hoyle & Fowler 1960; Mazzali et al. 2007). However, it is still not known how the WD reaches M_{ch} . Over the last five decades or so, many progenitor scenarios have been proposed. In the following subsections, we summarize one of the most popular scenarios, namely the single degenerate scenario, which is imperative in the nova context, and briefly touch upon the other alternative scenarios given in literature. Recent reviews by Maoz et al. (2014) and Wang & Han (2012) provide a comprehensive overview of the various progenitor models of SNe Ia.

1.2.1 Single degenerate scenario

In the single degenerate (SD) scenario (Whelan & Iben 1973), the WD is in a binary system with a non-degenerate companion. The companion can be a main-sequence star, a red giant, or even a helium star (see Wang & Han 2012). In this scenario, the mass accretion rate on the WD is a critical parameter that determines the growth of the WD mass (Fig. 1.2). As the WD in such a binary system accretes mass from its companion, nuclear burning of hydrogen is ignited at the base of the accreted hydrogen envelope after the critical temperature and pressure are reached. Calculations of several groups have led to the conclusion that stable nuclear burning of the accreted material at the same rate as it is supplied by the donor star is possible only in a rather narrow range of the mass accretion rates around $\text{few} \times 10^{-7} M_{\odot} \text{ yr}^{-1}$ (Nomoto 1982; Wolf et al. 2013; Kato et al. 2014). It has been argued that this is the regime allowing the most efficient build-up of mass on the WD. As a result of the energy released in the hydrogen fusion, the WD becomes a powerful source of soft X-ray emission, the so-called supersoft X-ray source (SSS; van den Heuvel et al. 1992; Kahabka & van den Heuvel 1997). For very large mass accretion rates not all the accreted material can be processed in the nuclear fusion and it has been argued whether the accreted envelope puffs up leading to a red-giant-like configuration (Cassisi et al. 1998) or a radiation driven wind from the WD blows away the excess mass (wind phase; Hachisu et al. 1996). The latter argument allows the WD to grow its mass at a rate equal to the steady nuclear-burning rate. At lower mass accretion rates, below the stability strip (the area between the two curves in Fig. 1.2), conditions at the base of the envelope of accreted material are insufficient for steady hydrogen fusion, and it undergoes regular thermonuclear runaways, resulting in nova explosions (cf. Sect. 1.1.2). The explosions may be accompanied by significant mass loss from the system (e.g., Prialnik & Kovetz 1995).

While numerous attempts to find the progenitors of individual SNe Ia have not (yet) yielded convincing detections, an alternative avenue has recently been explored with the aim to constrain the overall populations of accreting WDs in galaxies. In particular, Gilfanov & Bogdán (2010) demonstrated that the observed soft X-ray luminosity of early-type galaxies is too low to allow a significant population of hot ($T \gtrsim 5 \times 10^5$ K) accreting WDs with stable nuclear burning, which are required to explain the SN Ia rates in these galaxies. Populations of cooler WDs³ have been constrained by Woods & Gilfanov (2013, 2014) and Johansson et al. (2014) using the strength of He II recombination lines in the line emission spectra of passively evolving galaxies. Their work effectively excluded the parts of the parameter space corresponding to accreting WDs in and above the stability strip, at least in passively evolving galaxies.

Below the stability strip, theoretical modeling of nova explosions has demonstrated that at mass accretion rates $\lesssim 10^{-8}$ – $10^{-7} M_{\odot} \text{ yr}^{-1}$, the entire accreted mass is likely to be lost from the system during the explosion (e.g., Prialnik & Kovetz 1995; Yaron et al. 2005). However, close to the stability line, $\dot{M} \sim 10^{-7} M_{\odot} \text{ yr}^{-1}$, nova explosions are relatively weak and are not accompanied by significant mass loss. Therefore, mass accumulation by

³Such cooler sources may appear in the case of lower-mass WDs or a considerable expansion of the WD photosphere, cf. the wind regime.

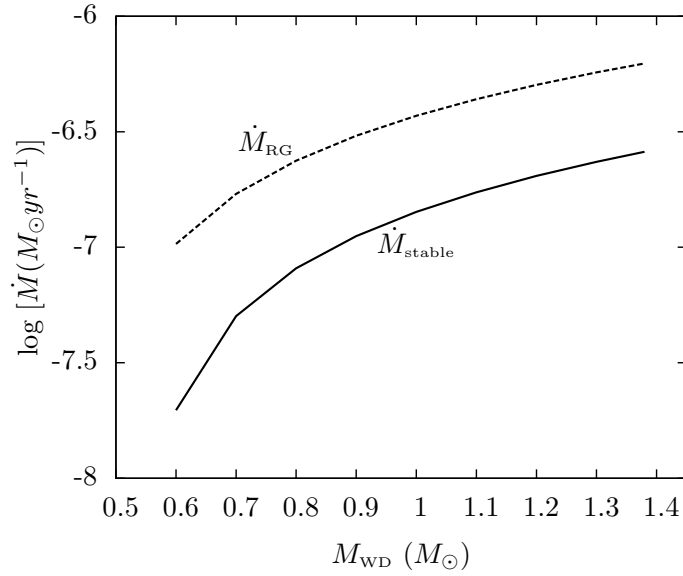


Figure 1.2: Stability conditions for the hydrogen shell burning on the WD surface. From Nomoto et al. (2007), $\dot{M}_{\text{stable}} = 3.066 \times 10^{-7} \left(\frac{M}{M_{\odot}} - 0.5357 \right) M_{\odot} \text{yr}^{-1}$ and $\dot{M}_{\text{RG}} = 6.682 \times 10^{-7} \left(\frac{M}{M_{\odot}} - 0.4453 \right) M_{\odot} \text{yr}^{-1}$. Below \dot{M}_{stable} the hydrogen burning is unstable, while \dot{M}_{RG} corresponds to the maximum hydrogen burning rate possible on the surface of the WD of the given mass. For a recent version of this plot, based on evolutionary calculations, see Wolf et al. (2013).

the WD may be possible in this regime (Hillman et al. 2015). Moreover, work by Starrfield (2014), Hillman et al. (2015), and others has contested the entire existence of the stability strip. Instead, they suggested that nuclear burning is unstable in the entire mass accretion rate range up to very high rates, where common envelopes form. In this picture, the nuclear burning proceeds in the form of flashes caused by regular thermonuclear runaways, with significant net mass accumulation by the WD. These results inspired a corresponding class of SN Ia progenitor models involving novae of various types (e.g., Starrfield et al. 1985; Hachisu & Kato 2001; Hillman et al. 2015). However, it was pointed out by some authors that the presence of a significant population of such systems with unstable nuclear burning in galaxies will result in nova rates that by far exceed the observed values (see Gilfanov & Bogdán 2011). Nevertheless, no detailed calculations have been performed in this regard. With our work, presented in Chapters 2 and 3 of this thesis, we effectively bridge this shortcoming, obtaining definite quantitative constraints for the role of novae in producing SNe Ia.

1.2.2 Double degenerate and other scenarios

One scenario that enjoys as much popularity as the SD one is the double degenerate (DD) scenario. In this scenario (Webbink 1984; Iben & Tutukov 1984b), the SN Ia explosion is produced by the merger of two CO WDs, driven by gravitational wave radiation. The less massive WD is thought to be tidally disrupted and then accreted by the more massive WD (e.g., Lorén-Aguilar et al. 2009; Pakmor et al. 2012). Variants on the driver of the WD encounters, other than gravitational waves, have also been invoked by different authors, for example head-on collision (Rosswog et al. 2009) or Kozai oscillations in the eccentricity of the binary in hierarchical triple systems (Thompson 2011). However, there are important details, such as the ignition conditions in the merger remnants or the conditions for operation of the special drivers of WD encounters, that are not well understood for this scenario (see Maoz et al. 2014 for details).

There are other exotic models for the SN Ia progenitors that have been proposed by different authors, albeit with substantial uncertainties in each case. These include thermonuclear explosions of sub-Chandrasekhar mass WDs, accreting helium from their companions, by double detonations – detonation of the accreted helium on the surface that in turn drives the ignition of carbon at the core (Fink et al. 2010). Further, explosions of super-Chandrasekhar mass WDs, supported by rotation, have been considered to explain the observation of SNe Ia much brighter than the normal ones (Silverman et al. 2011; Scalzo et al. 2012). Kashi & Soker (2011) proposed a progenitor model, the so-called core-degenerate model, involving a merger of the WD and the core of the AGB star during the common envelope phase. SNe Ia from single stars, resulting from ignition of the degenerate core of an AGB star, have also been explored (Iben & Renzini 1983).

1.3 Scope for novae in modern time-domain surveys

With the advance in computing technology, tremendous progress has been achieved in the theoretical modeling of novae compared to 4-5 decades ago, when the nova theory had been just conceived. Now it has become a routine task in simulations of the nova phenomenon to perform multi-cycle evolutionary calculations – an element necessary to erase the sensitivity of the models to initial conditions. On this note, we point out the significant contribution made by the Tel Aviv group (Prialnik & Kovetz 1995; Yaron et al. 2005). To date their models are most popular in the nova community. This is on account of the fact that their models are able to reproduce the entire range of observed properties of novae. In this respect, a most interesting facet of the nova models, relevant in the present most-active era of time-domain astronomy, is their prediction of fast declining novae – from a day to few hours (see Chapter 2 for details). Some of such novae may also be quite faint, that is, significantly fainter than the typical brightness of observed fast novae (Kasliwal et al. 2011).

The upcoming large-scale surveys, in particular the Large Synoptic Survey Telescope (LSST) project (the LSST Science Collaboration; <http://www.lsst.org/files/docs/SRD.pdf>), with gigantic telescopes will be able to afford both the cadence and depth necessary to pick up novae from the entire predicted ranges – in both temporal and brightness. In general, for all novae, a comprehensive coverage during their rise and initial decline will also become possible; this is the phase that captures the most crucial physics of the nova outburst. Therefore, observation of the lightcurves, coupled with early spectroscopic follow-up, of this early nova phase will enable us to probe directly the explosion itself. Such an effort no doubt will allow us to consolidate the existing theoretical models of novae, for example to resolve some of the critical issues that persist in the present nova models, like mixing and the mechanism of the continued mass loss (cf. Sects. 1.1.2, 1.1.3). Moreover, there is always an open window for unforeseen discoveries, when hunting for these objects in the expected “big” data from these surveys. The following chapters will further throw light on the significance of high-cadence surveys in various contexts of our studies of novae. Realizing the worth of such efforts, we have already spearheaded work in this direction – in search for fast novae in high-cadence optical surveys. Chapter 5, in which we describe a new method for detecting transients in optical time-domain surveys, is one consequence of our efforts.

Chapter 2

Constraining the role of novae as progenitors of type Ia supernovae

2.1 Introduction

In Sect. 1.2, the importance of SNe Ia in various astrophysical contexts has been discussed. In particular, the landmark discovery of the accelerating expansion of the Universe came about by using SNe Ia to measure cosmological distances (Riess et al. 1998; Perlmutter et al. 1999). With the advent of the era of large-scale surveys yielding large samples of SNe Ia, the uncertainties in cosmological SN Ia studies are now dominated not by statistical, but by systematic effects. The cosmological distance measurements based on SNe Ia assume that the physical properties of their progenitors remain unchanged with redshift, although growing evidence points to the contrary (e.g., Milne et al. 2015). Hence, the lack of understanding of the nature of their progenitors is one of the important sources of systematic uncertainties (Howell 2011; see Sect. 1.2). Although it is established beyond reasonable doubt that these gigantic explosions are a result of the thermonuclear disruption of a CO WD near the Chandrasekhar mass limit, the details are still being debated. In particular, no consensus has been reached regarding how the WD, whose initial mass is likely to be below $\sim 1 M_{\odot}$, reaches the Chandrasekhar limit. To date, there are two main hypotheses — the single-degenerate (SD) scenario, in which a WD gains mass by accreting hydrogen-rich material from a non-degenerate companion before exploding as a SN Ia, and the double-degenerate (DD) scenario, in which two CO WDs coalesce driven by gravitational wave radiation producing a SN Ia (cf. Sects. 1.2.1, 1.2.2).

As discussed in Sect. 1.2.1, secular growth in the WD mass may be possible for those systems in the nova regime, where the WDs accrete mass at high \dot{M} 's. This led to novae being proposed as one of the viable candidates for SN Ia progenitors (e.g., Starrfield et al. 1985; Hachisu & Kato 2001; Hillman et al. 2015). In this respect, Gilfanov & Bogdán (2011) pointed out that this particular SN Ia progenitor model would come into conflict with the observed nova statistics in galaxies. In this chapter, we investigate the proposition made by Gilfanov & Bogdán (2011) in depth. In Sect. 2.2, we compute the number of novae

expected to be produced by a typical SD progenitor accreting in the unstable nuclear burning regime. To this end, we use the multicycle nova models of Prialnik & Kovetz (1995), Yaron et al. (2005) and Hillman et al. (2015). Using the predicted number of novae per SN Ia and the nova rate in M31 measured by the POINT-AGAPE survey (Darnley et al. 2006), we estimate the maximal contribution that novae can make to the SN Ia rate in Sect. 2.3. We then point out that, should the nova channel be responsible for a significant fraction of SNe Ia, the vast majority of novae would have short decay times; thus, an even more sensitive diagnostic can be provided by observations of fast novae. We address the completeness of nova surveys for fast novae in Sect. 2.4 and formulate requirements for future high-cadence surveys aimed to further examine the role of novae as SN Ia progenitors. Our results are discussed in the broader context of SN Ia models in Sect. 2.5. In this section, we also address the dependence of our results on the uncertainties of the multicycle nova models; in particular, we compare Yaron et al. (2005) models used in this chapter with the calculations of other groups and with observations. We conclude in Sect. 2.6.

2.2 Relation between supernova and nova rates

Assuming that an accreting WD spends some fraction of its accretion history in the unstable nuclear burning regime, one can estimate the number of novae n_{nov} it will produce while increasing its mass by ΔM_{wd} from the following obvious relation

$$\Delta M_{\text{acc}} n_{\text{nov}} \sim \Delta M_{\text{wd}}, \quad (2.1)$$

where ΔM_{acc} is the net mass gain by the WD per one nova explosion cycle.

However, the ignition mass of the nova, and hence ΔM_{acc} , depend on parameters of the WD and the binary system. To the first approximation, the main parameters are the WD mass M_{WD} , its temperature T_{WD} , and the accretion rate \dot{M} (Yaron et al. 2005), and we can rewrite Eq. (2.1) more accurately as

$$n_{\text{nov}} = \int_{M_i}^{M_{\text{ch}}} \frac{dM_{\text{WD}}}{\Delta M_{\text{acc}}(M_{\text{WD}}, \dot{M}, T_{\text{WD}})}. \quad (2.2)$$

Equation (2.2) gives the number of novae produced by an SD SN Ia progenitor while increasing its mass from some initial value M_i to the Chandrasekhar mass M_{ch} , assuming that the nuclear burning on the WD surface proceeds in the unstable regime.

The majority of multicycle nova evolution models give ignition mass rather than the accreted mass, as the former is much more straightforward to compute (e.g., Townsley & Bildsten 2004). For this reason we reformulate Eq. (2.2) in terms of the ignition mass ΔM_{ign} . Because of the mass loss during the nova explosion, $\Delta M_{\text{acc}} \leq \Delta M_{\text{ign}}$, and therefore we obtain a lower limit on the number of novae produced by one single degenerate SN Ia

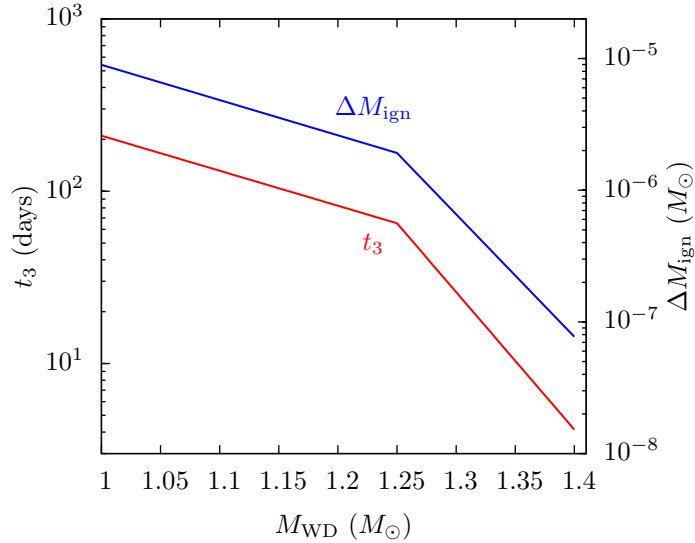


Figure 2.1: Variation of the ignition mass of the nova ΔM_{ign} and the mass-loss timescale t_{ml} (\approx decline time of the outburst by 3 magnitudes from optical peak, t_3) with the mass of the WD for the accretion rate $\dot{M} = 10^{-7} M_{\odot}\text{yr}^{-1}$ and WD core temperature 10^7 K, from Yaron et al. (2005).

progenitor

$$n_{\text{nov}} \geq \int_{M_i}^{M_{\text{ch}}} \frac{dM_{\text{WD}}}{\Delta M_{\text{ign}}(M_{\text{WD}}, \dot{M}, T_{\text{WD}})}. \quad (2.3)$$

Equation (2.3) gives an estimate of the total number of novae regardless of their individual characteristics. On the other hand, Fig. 2.1 shows that as the WD mass increases toward the Chandrasekhar limit, ΔM_{ign} decreases as well as t_3 – decline time of the optical light curve from the peak by 3 magnitudes. Therefore, as the WD mass grows, it produces more frequent nova explosions with shorter decline times, meaning that the majority of the novae relevant to the SN Ia progenitor problem should be characterized by fast decline. Thus, a more detailed diagnostic can be provided by the distribution of novae over the decline time of their light curves.

To obtain the latter, we note that in the multicycle nova evolution models of Yaron et al. (2005), for fixed mass accretion rate and WD core temperature, the light-curve decay timescale is determined solely by the WD mass. Therefore, the cumulative distribution of novae over decay time is given by

$$n_{\text{nov}} (\leq t_n) \geq \int_{M(t_n)}^{M_{\text{ch}}} \frac{dM_{\text{WD}}}{\Delta M_{\text{ign}}(M_{\text{WD}}, \dot{M}, T_{\text{WD}})}. \quad (2.4)$$

Here t_n is the time to decline by n mag from peak ($n = 2, 3$), $n_{\text{nov}}(\leq t_n)$ is the cumulative number of novae with decline time shorter than or equal to t_n and $M(t_n)$ is the WD mass

corresponding to the given decline time t_n (for the given values of \dot{M} and T_{WD}). As before, the inequality sign in Eq. (2.4) reflects the fact that the net accreted mass can be lower than the envelope ignition mass. The corresponding differential distribution is given by

$$\frac{dn_{\text{nov}}(t_n)}{dt_n} \geq \frac{1}{\Delta M_{\text{ign}}(M_{\text{WD}}, \dot{M}, T_{\text{WD}})} \frac{dM(t_n)}{dt_n}. \quad (2.5)$$

As before, this distribution gives the number of novae with particular temporal properties per one type Ia supernova.

In the following, we use the results of the multicycle nova evolutionary calculations by Yaron et al. (2005). Their results for the envelope ignition mass and t_3 timescale of the light curve are shown in Fig. 2.1. We carry out calculations for three values of the mass accretion rates – 10^{-7} , 10^{-8} and $10^{-9} M_{\odot} \text{ yr}^{-1}$ and assume WD core temperature of 10^7 K. Our choice is explained below. In addition, some of the calculations in Sect. 2.3 are done for the mass-accretion rate of $5 \times 10^{-7} M_{\odot} \text{ yr}^{-1}$, which is not tabulated in Yaron et al. (2005). To this end, we use the results of Hillman et al. (2015) that are based on a modified version of the code of Prialnik & Kovetz (1995). We estimate the nova ignition masses using their plot of the nova cycle duration against the mass-accretion rate (Fig. 2 in Hillman et al. 2015). As a proxy for the nova decline time t_3 , we use the flash duration plotted in their Fig. 7. We verified that the so-obtained nova ignition masses and t_3 timescales are consistent (albeit not identical) with the interpolation of Yaron et al. (2005) results.

The mass loss during the nova explosion becomes more significant at lower mass-accretion rates (e.g., Yaron et al. 2005; Hillman et al. 2015). Therefore, in the context of the problem of SN Ia progenitors, only relatively high mass-accretion rates ($\sim 10^{-7} M_{\odot} \text{ yr}^{-1}$) are relevant. We therefore assumed the mass-accretion rate of $10^{-7} M_{\odot} \text{ yr}^{-1}$ in our baseline configuration, but also considered lower values of 10^{-8} and $10^{-9} M_{\odot} \text{ yr}^{-1}$ to investigate the trends with \dot{M} . Some of the calculations in Sect. 2.3 are done for $\dot{M} = 5 \times 10^{-7} M_{\odot} \text{ yr}^{-1}$ to allow direct comparison of predictions of the Hillman et al. (2015) model with observations.

Our choice of the WD core temperature is motivated by the results of Townsley & Bildsten (2004), who studied the effect of accretion on the thermal state of the WD and found an equilibrium WD core temperature of $\sim 8\text{--}10 \times 10^6$ K for accretion rates in the range $10^{-9} - 10^{-8} M_{\odot} \text{ yr}^{-1}$, the temperature increasing with \dot{M} . Their calculations only covered the mass-accretion rates typical for classical novae and did not extend beyond $10^{-8} M_{\odot} \text{ yr}^{-1}$. However, at high mass-accretion rates, $\gtrsim 10^{-7} M_{\odot} \text{ yr}^{-1}$, the properties of nova outbursts do not strongly depend on the core temperature because the overlying hot He layer from previous outbursts acts as a heat barrier (Townsley & Bildsten 2004; Wolf et al. 2013). We therefore assumed a core temperature of 10^7 K in our baseline configuration. We investigate the dependence of our results on the core temperature in more detail in Sect. 2.3.

Yaron et al. (2005) provided two timescales characterizing the light-curve decay rate – the duration of the mass-loss phase t_{ml} and the decline time of the bolometric luminosity by 3 mag from maximum $t_{3,\text{bol}}$. From an observational point of view, however, the timescale of interest is the decline time of the optical light from the nova. From the comparison

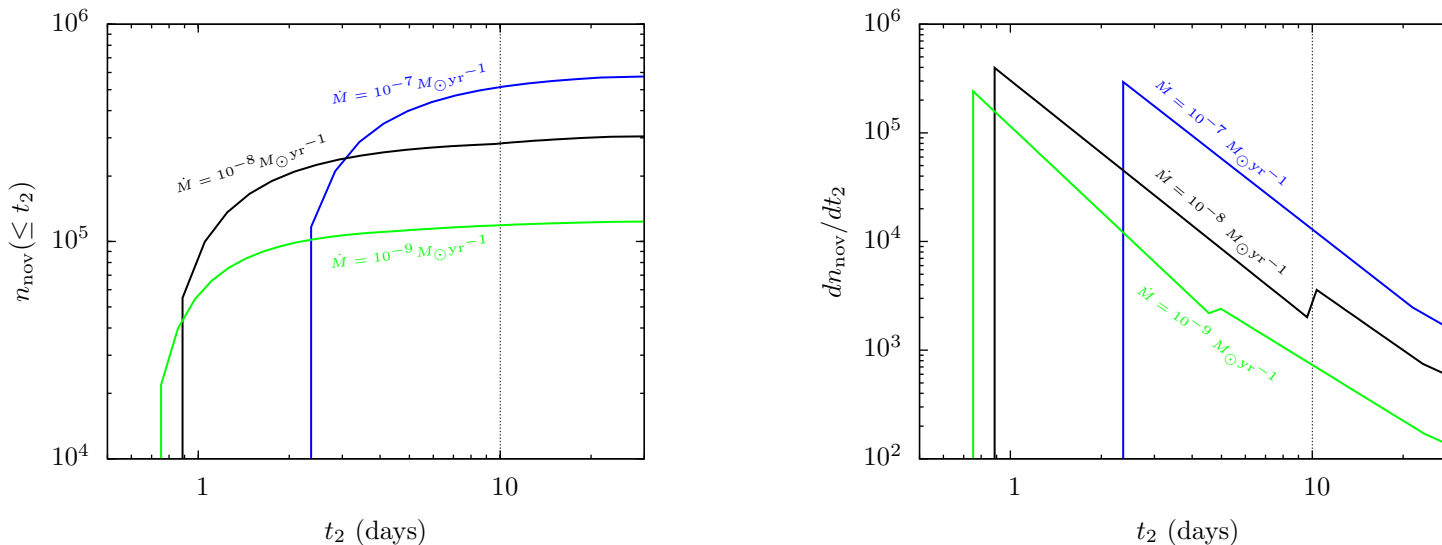


Figure 2.2: Cumulative (*left*) and differential (*right*) t_2 distributions of novae produced by one successful SN Ia progenitor, assuming that it accreted in the unstable nuclear burning regime throughout its entire accretion history. The numbers near the curves indicate the mass-accretion rate. The discontinuities in the differential distributions are caused by the discontinuity in the slope of log-linear interpolation of t_2 and M_{WD} values from Yaron et al. (2005) tabulation. They do not affect the cumulative distribution in any significant way, as can be seen in the left panel. The sharp drop in the distributions at low t_2 values corresponds to the fastest novae produced by the WD near the Chandrasekhar mass limit.

of the results from Yaron et al. (2005) with observations, it is known that t_{ml} and $t_{3,\text{bol}}$ bracket t_3 (Prialnik & Kovetz 1995; Yaron et al. 2005; Kasliwal et al. 2011). The shorter of these two, t_{ml} , is much closer to the observed t_3 than $t_{3,\text{bol}}$. We therefore proceed with t_{ml} as an approximation to t_3 . We investigate how our results change if we use the longer $t_{3,\text{bol}}$ in Sect. 2.3. For extragalactic novae, where the survey sensitivity¹ becomes a problem, it is easier in practice to measure t_2 (the time to decline by 2 mag from peak) than t_3 . For fast novae, the two quantities are approximately related by $t_2 \approx t_3/2.1$, for the slow novae by $t_2 \approx t_3/1.75$, with the transition at $t_3 = 50$ days following Duerbeck (in Bode & Evans 2008). We mostly use t_2 throughout the remainder of the chapter.

For each value of the mass-accretion rate we log-linearly interpolated the ignition mass ΔM_{ign} , t_{ml} and $t_{3,\text{bol}}$ between the grid values of the WD mass (0.4, 0.65, 1.0, 1.25, and 1.4 M_{\odot}) in Yaron et al. (2005). The lower integration limit in Eq. (2.4) was conservatively assumed to be equal to 1.0 M_{\odot} . For $\dot{M} = 10^{-7} M_{\odot} \text{ yr}^{-1}$; this corresponds to slow novae with $t_3 \approx 200$ days. As the differential distribution of novae over t_2 is sufficiently steep, $dn_{\text{nov}}/dt_2 \propto t_2^{-2}$ (see discussion of Fig. 2.2 below), the choice of the initial WD mass is not very important when considering the integrated nova rates, as long as it is not too close to the Chandrasekhar mass.

The so-computed cumulative and differential t_2 distributions of novae are shown in Fig. 2.2. As expected, a significant fraction of novae produced by a successful SD SN Ia progenitor have short t_2 times. For example, in our baseline calculation ($\dot{M} = 10^{-7} M_{\odot} \text{ yr}^{-1}$) we obtain the total predicted number of novae per one SN Ia $\sim 6.5 \times 10^5$. Of these, more than 60% have $t_2 \lesssim 5$ days and about 80% have t_2 shorter than 10 days. The predicted number of novae grows with the mass-accretion rate, reaching $\sim 7.7 \times 10^5$ for $\dot{M} = 5 \times 10^{-7} M_{\odot} \text{ yr}^{-1}$.

2.3 Statistics of novae in M31

M31 has been a hot spot for the observation of novae since the work of Hubble (1929). We have chosen this galaxy for our analysis because of its many detections. We start this section by reviewing recent supernova and nova rate measurements in M31 and then proceed with constraining the contribution of the nova channel to the observed SN Ia rate using the results of the previous section.

2.3.1 SN Ia rate in M31

The morphological type of M31 is Sb (de Vaucouleurs et al. 1991), for which Mannucci et al. (2005) reported the stellar mass specific SN Ia rate of $6.5 \times 10^{-4} \text{ SNe yr}^{-1}$ per $10^{10} M_{\odot}$. However, Hubble morphological classes are rather broad — indeed, for the adjacent morphological type Sbc/d, the quoted SN Ia rate is higher by a factor of ~ 2.5 . Therefore, there must inevitably be some spread in the SN Ia rates between galaxies of the

¹It is generally limited by the unresolved surface brightness of the host galaxy rather than the limiting magnitude of the survey as such (see Sect. 2.4).

same morphological type. Mannucci et al. (2005) used the morphological type of the galaxy as a proxy for its star formation rate (SFR). To the first approximation, the mass-specific SN Ia rate is determined by the current SFR (e.g., Sullivan et al. 2006; see also Maoz et al. 2014) in the absence of detailed knowledge of the star formation history of the galaxy. A more accurate and continuous characterization of the current SFR of the galaxy is its color, albeit also with considerable spread. In particular, Mannucci et al. (2005) used the $B - K$ color to quantify the dependence of the supernova rate on SFR. The extinction-corrected $B - K$ color of M31 within ~ 10 – 20 kpc from the galactic center is $B - K \approx 3.5$ mag (Battaner et al. 1986). From Fig. 5 in Mannucci et al. (2005) we find the mass-specific SN Ia rate of $\sim 1.0 \times 10^{-3}$ SNe yr $^{-1}$ per $10^{10} M_{\odot}$, which is somewhat higher than inferred from its morphological type. This number is compatible with the more recent result of Li et al. (2011), who obtained a mass-specific SN Ia rate of $(0.85_{-0.12}^{+0.13}) \times 10^{-3}$ SNe yr $^{-1}$ per $10^{10} M_{\odot}$ in their $B - K = 3.4$ – 3.7 mag bin for a galaxy of stellar mass $1.1 \times 10^{11} M_{\odot}$ (see below). Of course, the current SFR value can also be used directly. The SFR estimates for M31 are in the range ≈ 0.4 – $0.8 M_{\odot} \text{ yr}^{-1}$ (Barmby et al. 2006; Devereux et al. 1994), and with the Sullivan et al. (2006) calibration, we obtain an SN Ia rate of $(0.5$ – $0.6) \times 10^{-3}$ SNe yr $^{-1}$ per $10^{10} M_{\odot}$, also compatible with the above numbers.

From the physical point of view, the SN Ia rate of the galaxy is determined by the convolution of its star formation history with the delay time distribution (DTD) of SNe Ia (Maoz & Mannucci 2012). As the former is poorly known, we used the DTD value at the delay time equal to the mean stellar age of M31 to estimate its SN Ia rate. Olsen et al. (2006) found both the bulge and inner disk of M31 to be dominated by old (6–10 Gyr) stellar population, and Brown et al. (2006) found the outer disk to be dominated by 4–8 Gyr old stars. Then, taking the mean age for the M31 stellar population to be 8 Gyr and using the delay time distribution of Totani et al. (2008) we obtain a mass-specific rate of $\approx 0.7 \times 10^{-3}$ SNe yr $^{-1}$ per $10^{10} M_{\odot}$.

Thus, different estimations give approximately consistent values of the specific SN Ia rate in M31 in the range of $\approx (0.5$ – $1.0) \times 10^{-3}$ SNe yr $^{-1}$ per $10^{10} M_{\odot}$. In the following, we conservatively use the rate based on the result reported by Mannucci et al. (2005) for Sb galaxies, that is, 0.65×10^{-3} SNe yr $^{-1}$ per $10^{10} M_{\odot}$, which is one of the lower rate estimates from above. As the nova rates are directly proportional to the SN Ia rate (e.g., Eq. 2.3), any higher SN Ia rate will only strengthen our conclusions. With the stellar mass of M31 of $1.1 \times 10^{11} M_{\odot}$ (Barmby et al. 2007) we obtain its SN Ia rate, $\dot{N}_{\text{SNIa}} = 7.15 \times 10^{-3} \text{ yr}^{-1}$, which we use in our calculations below.

2.3.2 Nova rate in M31

Altogether, there are more than 900² novae detected in the direction of M31 (e.g., Hubble 1929; Arp 1956; see also Capaccioli et al. 1989). However, the majority of the existing nova catalogs lack an accurate incompleteness analysis, which renders them unsuitable for use in our calculations.

²http://www.mpe.mpg.de/~m31novae/opt/m31/M31_table.html (Pietsch et al. 2007)

Completeness of a nova survey is determined by the usual factors, such as spatial variation of the sensitivity caused by incomplete coverage of the survey, variation of the surface brightness of the galaxy, and extinction. In addition, it is determined by the factors related to the transient nature of the sought objects, such as temporal sampling of the survey and variation in the light-curve morphology. The most thorough completeness analysis to date among the nova surveys was performed for the nova catalog produced in the course of the recent POINT-AGAPE (Pixel-lensing Observations with the Isaac Newton Telescope – Andromeda Galaxy Amplified Pixels Experiment) survey (Darnley et al. 2004). The POINT-AGAPE nova catalog was produced by an automated detection pipeline, thus permitting an objective characterization of its completeness (many even relatively recent nova surveys relied on some form of a visual inspection of the images and/or light curves, which makes their completeness difficult to compute accurately). Darnley et al. (2006) carried out a careful analysis of the completeness of the detection pipeline and the survey itself. To this end, they seeded the raw POINT-AGAPE data with resampled light curves of their detected novae. This allowed them to compute the completeness of the POINT-AGAPE nova catalog and to obtain a robust estimate of the underlying global nova rate in M31. As a result of these analyses, they produced the global nova rate of $65_{-15}^{+16} \text{ yr}^{-1}$.

2.3.3 Contribution of novae to the SN Ia rate

With the nova rate known, we estimated the maximal SN Ia rate these novae can produce as follows

$$\dot{N}_{\text{Ia,nov}} \leq \frac{\dot{N}_{\text{nov}}}{n_{\text{nov}}}, \quad (2.6)$$

where $\dot{N}_{\text{Ia,nov}}$ is the SN Ia rate that may be produced by novae, n_{nov} is the number of novae produced by one successful SN Ia progenitor (cf. Eq. 2.3), and \dot{N}_{nov} is the observed nova rate. We note that Eq. (2.6) gives an upper limit on the nova contribution to the SN Ia rate for at least two reasons: (i) Eq. (2.3) gives only the lower limit of the number of novae per SN Ia, as discussed in Sect. 2.2; (ii) obviously, not all novae reach the Chandrasekhar mass limit.

However, before the nova rate of 65 yr^{-1} can be inserted into Eq. (2.6), the following should be considered. The POINT-AGAPE nova catalog does not contain very fast novae with $t_2 \lesssim 10$ days in the r' band. Therefore, as discussed in Darnley et al. (2006), their completeness modeling is only sensitive to novae with an r' -band t_2 between 9.80 days (the fastest nova in their catalog) and 213.12 days (the slowest nova). In this t_2 range, there was no strong evidence suggesting large variation in the completeness as a function of t_2 , the only variation being, as expected, spatial (Matt J. Darnley, private communication). Therefore, for a fair comparison, n_{nov} in Eq. (2.6) should be the number of novae with light-curve decay times in the range $10 \lesssim t_2 \lesssim 213$ days. Because of the steepness of the differential distribution dn_{nov}/dt_2 (Fig. 2.2), the latter is nearly equivalent to $t_2 \geq 10$ days³.

³Since the red bands contain the H-alpha emission line, which declines more slowly than the continuum, the quoted t_2 time may be somewhat overestimated compared to the t_2 measured in the V band (see Darnley

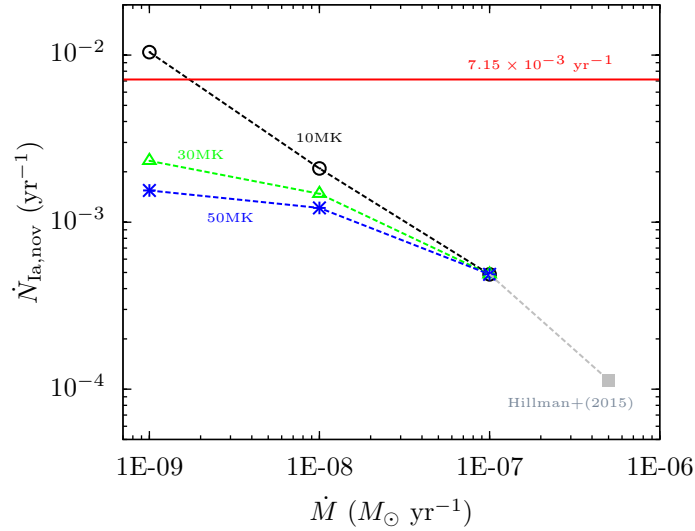


Figure 2.3: Maximal contribution of novae to the SN Ia rate of M31 as a function of assumed mass accretion rate for different values of WD core temperature as indicated by the numbers near the curves. The point at $\dot{M} = 5 \times 10^{-7} M_{\odot} \text{ yr}^{-1}$ (shown in gray) is computed from the models of Hillman et al. (2015); other points are computed based on Yaron et al. (2005) nova models. The red solid line shows the M31 supernova rate.

The maximal supernova rate computed from Eq. (2.6) is shown in Fig. 2.3. As can be seen, our baseline model ($\dot{M} = 10^{-7} M_{\odot} \text{ yr}^{-1}$) predicts the maximal SN Ia rate of $\approx 5.0 \times 10^{-4} \text{ yr}^{-1}$. For the mass-accretion rate of $\dot{M} = 5 \times 10^{-7} M_{\odot} \text{ yr}^{-1}$ considered by Hillman et al. (2015), the maximal SN Ia rate becomes $\approx 1.1 \times 10^{-4} \text{ yr}^{-1}$. Interestingly, for lower mass-accretion rates, observed population of novae could in principle explain a larger fraction of SNe Ia, and for very low rates, $\dot{M} \lesssim 10^{-9} M_{\odot} \text{ yr}^{-1}$, and low WD temperature, the predicted rate is compatible with the observed value. However, such low mass-accretion rates are believed to be irrelevant as regards the nature of SN Ia progenitors (Sect. 2.2). For the mass-accretion rates in the range $\sim (1 - 5) \times 10^{-7} M_{\odot} \text{ yr}^{-1}$, which are typically considered in this context, the maximal contribution of novae to the observed SN Ia rate is limited to $\approx 2 - 7\%$.

The upper limit on the contribution of novae to the SN Ia rate decreases by a few times if we use $t_{3,\text{bol}}$ instead of t_{ml} in the models of Yaron et al.. In this case, the supernova rate predicted in our baseline model is $\approx 1.8 \times 10^{-4} \text{ yr}^{-1}$, which is ~ 40 times lower than the observed SN Ia rate. At lower mass-accretion rates and WD temperatures, the maximal supernova rate is ~ 5 – 10 times short of the observed value.

In the above calculation, we ignored the possible difference of the observed novae in the WD composition. In particular, some fraction of the observed nova outbursts may be hosted by oxygen-neon (ONe) WDs (Truran & Livio 1986; Ritter et al. 1991; Gil-Pons

et al. 2006). An accurate accounting for this effect is beyond the scope of this work; we note, however, that it will increase the predicted rates (cf. Fig. 2.2) and will result in an even tighter constraint.

et al. 2003; Shore et al. 2013). For example, for the Galactic novae, Gil-Pons et al. (2003) estimated this fraction to be about $\sim 1/3$ of nova outbursts. The ONe WDs are known to undergo accretion-induced collapse upon reaching the Chandrasekhar mass limit, rather than producing SNe Ia, and therefore they should be excluded from our calculation of the contribution of novae to the supernova rate. This is not possible because the composition of the WD host in the majority of observed novae is unknown. However, Eq. (2.6) gives an upper limit for the nova contribution to the supernova rate and inclusion of some number of ONe novae in the nova rate does not invalidate it. Although the upper limit may be tightened somewhat by using the (unknown) pure CO nova rate, the results of Gil-Pons et al. (2003) suggest that the improvement will not be dramatic. Moreover, the POINT-AGAPE sample is dominated by the relatively slow novae with $t_2 \gtrsim 10$ days, which, according to the models of Yaron et al., are hosted by relatively lower mass WDs (cf. Fig. 2.1). Therefore the POINT-AGAPE sample is probably less contaminated by ONe novae (which are typically hosted by more massive WDs) than the overall population of novae.

2.3.4 Fast novae

About $\sim 80\%$ of the novae produced by a typical successful (unstably burning) SD SN Ia progenitor have short decay times, $t_2 \lesssim 10$ days (Sect. 2.2, Fig. 2.2). If a fraction f of the total number of SN Ia progenitors in M31 accrete in the unstable nuclear burning regime while accumulating their final $\Delta M \approx 0.1 M_\odot$ (i.e., from $M \approx 1.3 M_\odot$ to M_{ch}), fast novae with $t_2 \lesssim 10$ days⁴ should be produced at a rate of $\gtrsim 3.6 \cdot 10^3 \times f$, assuming $\dot{M} = 10^{-7} M_\odot/\text{yr}$. For example, if all the novae from the POINT-AGAPE sample were to reach the Chandrasekhar mass limit, the fast novae would be produced at a rate of $\sim 200 - 300 \text{ yr}^{-1}$.

Such fast novae have not been detected in the POINT-AGAPE survey, either because they are rare in M31 or because the survey was not sensitive to them, or a combination of these two reasons (Darnley et al. 2006). From results of other surveys, we know that some number of such fast novae do exist, an example being the famous M31N 2008-12a (Shafter et al. 2012; Darnley et al. 2014; Henze et al. 2014a; Tang et al. 2014a) (see also the MPE optical nova catalog from footnote 2), but their true frequencies in the bulge and the disk of the galaxy remain to be determined.

From the above it is obvious that statistics of fast novae could provide a powerful tool for investigating the populations of massive WDs with unstable nuclear burning and for further constraining their contribution to the observed SN Ia rates. Accurate determination of their frequency is, however, hindered because they are difficult to detect as a result of their short lifetimes; this demands surveys with a very high cadence. For example, the famous M31 nova, M31N 2008-12a, was only discovered to be a recurrent nova in 2008, although it explodes every year. This is discussed in the following section, where we

⁴We recall that in Yaron et al. (2005) models, the $t_2 \approx 10$ days corresponds to the WD mass of $\approx 1.3 M_\odot$, with the more massive WDs producing faster novae.

investigate how completeness of a nova survey depends on its temporal sampling.

2.4 Temporal sampling and completeness of nova surveys

In this section we investigate how efficiently fast novae can be detected in surveys of various sensitivity and cadence. Our goal is to identify typical requirements with respect to the temporal sampling and limiting magnitude of a modern CCD survey aimed to characterize the population of fast novae, rather than to substitute the actual completeness calculations. The latter should be performed taking into account the characteristics of the particular survey and parameters of its detection pipeline. We therefore do not include in our calculations the full complexity of the light-curve shapes, replacing it with a simple template (albeit derived from observed nova light curves), with its peak magnitude drawn from the range sampled by observed novae. We do, however, take into account spatially varying internal extinction in M31 and contribution of its unresolved surface brightness to the statistical noise in the image, that is, to the sensitivity in detecting novae. We conduct our simulations for a PTF-class telescope (1.2 m Samuel Oschin Telescope at the Palomar Observatory).

We employed the following procedure. First, based on observed novae, we produced a scalable light-curve template (Appendix B), which we used to model the light curve of a nova with a given peak magnitude and t_2 time. To draw the peak magnitude of the nova with the given t_2 , we produced an analog of the classic MMRD relation from a large, heterogenous set of observational data, with the main goal to sample the range of observed magnitudes as fully as possible (Appendix C). We then performed Monte Carlo simulations of the nova detection process. In these simulations, we randomly seeded a large number of novae distributed across the face of the galaxy for each value of t_2 and determined how often they are detected in a survey of a given limiting magnitude and temporal sampling⁵. The simulations were carried out in R band because this is the band used in many recent nova surveys of M31.

To determine the nova detection sensitivity, we considered the following. The noise in an image pixel containing $S = S_{\text{M31}} + S_{\text{sky}}$ counts (in DN unit) accumulated during the exposure time t_{exp} can be expressed as

$$\sigma = \frac{\sqrt{(S_{\text{M31}} + S_{\text{sky}}) \times g + \sigma_{\text{RDN}}^2 + d \times t_{\text{exp}}}}{g}, \quad (2.7)$$

where g is the gain, σ_{RDN} the readout noise, and d the dark current (see Howell 2006). For these, we assumed typical parameters of the PTF survey (Law et al. 2009) — 1.6 e-/DN, 12 e- and 0.1 e-/sec, respectively. For the S_{sky} we assumed typical Palomar sky brightness

⁵In some respect our approach is similar to the one used by Darnley et al. (2006) for their completeness analysis, with the difference that they used the very same novae detected in their survey, whereas here we used average statistical properties of a large compilation of novae.

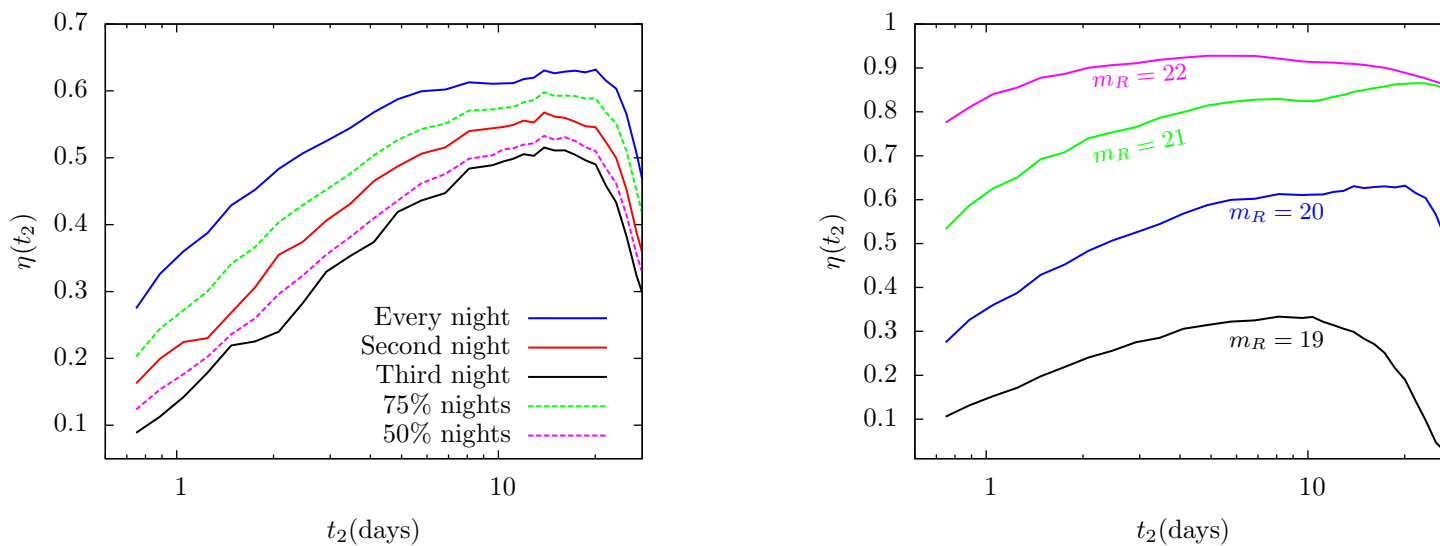


Figure 2.4: Detection efficiency for novae in M31 as a function of their decline time t_2 for surveys with the limiting magnitude of $m_R = 20$ and different temporal sampling (*left*) and for surveys of different limiting magnitudes with observations performed every night (*right*). The decline of the detection efficiency for slow novae is caused by their lower peak magnitudes and the finite time span of the simulated survey (see Sect. 2.4).

for photometric gray nights (Law et al. 2009; Laher et al. 2014). For the S_{M31} , we used the SDSS mosaic image of M31 from Tempel et al. (2011), which we converted from Sloan- r to R band using the relation from Blanton & Roweis (2007). We ran this image through SEXTRACTOR (Bertin & Arnouts 1996) to generate the unresolved surface brightness map of the galaxy. Since the SDSS mosaic image is sampled at a larger pixel scale ($3.96''$) than that of the PTF ($1.01''$), we reduced the pixel counts S from the SDSS image by ≈ 15.4 . The radius of the aperture used for measurement of a star is typically on the order of its FWHM (e.g., Mighell 1999), which is $\approx 2''$ for PTF images (Law et al. 2009). We therefore multiplied the pixel σ from Eq. (2.7) by a factor of ≈ 4 to obtain the effective rms noise for point source detection: $\sigma_{\text{ps}} = 4\sigma$. In our simulations, we conservatively assumed a $10\sigma_{\text{ps}}$ threshold for detecting novae.

We parameterized our simulations by the nominal limiting magnitude (m_{lim}) of the survey, which is related to the exposure time by the following for the sky-limited case that is typical of modern surveys

$$m_{\text{lim}} = ZP - 2.5 \times \log \left(\frac{5\sigma_{\text{sky}}}{t_{\text{exp}}} \right). \quad (2.8)$$

Here ZP is the zero point of the photometric calibration and σ_{sky} is the noise from the sky background in a typical aperture for star flux measurement. The latter is obtained from Eq. (2.7) with $S = S_{\text{sky}}$ and appropriate aperture correction as described above.

The intrinsic extinction map of M31 was computed based on the results of Tempel et al. (2011) to which a constant foreground reddening of $A_R = 0.15$ (Shafter et al. 2009) was added. The extinction was applied to all the seeded novae, depending on their spatial location in M31. However, its overall impact on the detection completeness does not exceed a few percent.

Taking into account the visibility of M31 from the northern hemisphere (between August and March), we assumed the survey duration to be 211 days. For every decline time t_2 in the range of interest, we seeded at every pixel of the SDSS image 20,000 novae occurring randomly in time within the survey time span. To each of the simulated novae, we assigned a peak magnitude that was drawn randomly from a Gaussian distribution with the mean and standard deviation as computed in Appendix C (Fig. C.1, Table C.1). The nova light curve was generated using the template derived in Appendix B, rescaled to have the desired t_2 and peak magnitude, Eq. (B.1) and then the extinction was applied. The detection efficiency was determined for every pixel of the SDSS image as the ratio of the number of detected novae, whose decline time t_2 could be measured, to the total number of seeded novae. To obtain the overall efficiency $\eta(t_2)$, these values were then averaged across the image, with the weights proportional to the stellar mass contained in the given pixel (i.e., we assumed that the nova rate scales with the stellar mass). To characterize the latter, we used the Spitzer 3.6 micron mosaic image of M31 by Barmby et al. (2006). We thus computed the completeness curves for every survey configuration we had set up, determined by the observing pattern (every night, second night, third night, 75% and 50% random coverage) and limiting magnitude (19 to 22 mag).

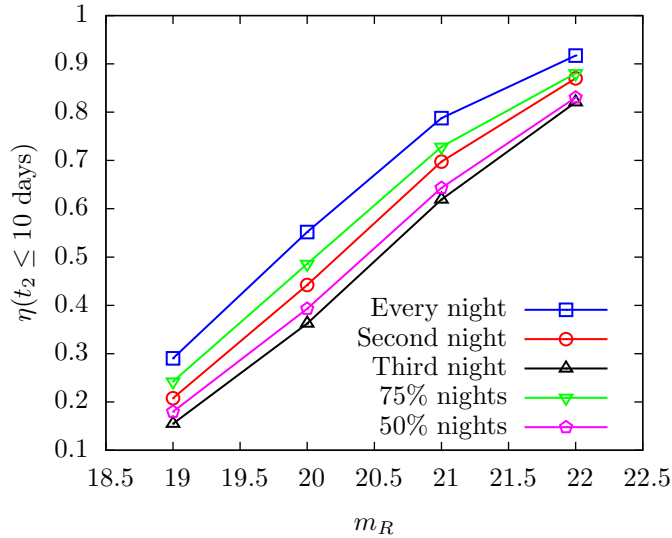


Figure 2.5: Fraction of all fast novae with $t_2 \leq 10$ days detected in surveys of different temporal sampling as a function of their limiting magnitude. It is assumed that the distribution of novae over decay times $dn_{\text{nov}}(t_2)/dt_2$ is given by Eq. (2.5) for a mass accretion rate of $\dot{M} = 10^{-7} M_{\odot} \text{ yr}^{-1}$.

The results of these simulations are plotted in Fig. 2.4. As expected, the detection efficiency declines toward short t_2 because novae with shorter t_2 times fade away faster and therefore are less likely to be detected than their longer lasting counterparts. On the other hand, the detection efficiency also drops toward long t_2 . This is caused by the combined effect of their lower peak magnitudes (Fig. C.1) and the finite observation time span. The latter is obviously determined by the survey duration. For example, a survey conducted in two consecutive years would have a better detection efficiency for slow novae than those shown in Fig. 2.4 (but the same for short novae).

The cumulative efficiency of the survey (i.e., the fraction of all novae with the t_2 time shorter than a given value that are detected in the survey) depends on dn_{nov}/dt_2 – the expected distribution of novae over t_2

$$\eta(\leq t'_2) = \left(\int_0^{t'_2} \eta(t_2) \frac{dn_{\text{nov}}}{dt_2} dt_2 \right) \left(\int_0^{t'_2} \frac{dn_{\text{nov}}}{dt_2} dt_2 \right)^{-1}. \quad (2.9)$$

The true distribution dn_{nov}/dt_2 is unknown, however. For example, in the “vanilla” SD scenario from Sect. 2.2, the distribution is given by Eq. (2.5). The result for $\dot{M} = 10^{-7} M_{\odot} \text{ yr}^{-1}$ is shown in Fig. 2.5 for surveys of different temporal sampling as a function of their limiting magnitude. This plot shows that a high-cadence survey with a limiting magnitude of $m_R = 22$ will detect about ≈ 80 – 90% of fast novae ($t_2 \leq 10$ days). To detect more than 50% of fast novae in a survey with observations conducted every night, its limiting magnitude has to be better than $m_R \approx 20$. If observations are carried out every third night, a limiting magnitude of $m_R \approx 20.5$ is required.

To see how the detection efficiency translates into absolute numbers of novae, we consider the recent PTF survey of M31 as an example. PTF has been conducting regular and frequent M31 observations during the corresponding visibility periods (approximately from July/August to December/January). From Fig. 2 of Cao et al. (2012) we estimate that the observing schedule typically covers $\approx 50\text{--}80\%$ of the nights during these periods every year. For the 5-sigma limiting magnitude of $m_R \approx 20.6$ (Law et al. 2009), we estimate from Fig. 2.5 the detection efficiency of $\sim 55\text{--}65\%$. The “vanilla” SD scenario predicts about ≈ 3600 fast ($t_2 \leq 10$ days) novae per year in M31. One should also take into account that the M31 visibility periods for the PTF telescope cover approximately 0.5 year. We therefore predict that the PTF survey of M31 should be detecting of the order of $\sim 1000 \times f$ fast ($t_2 \leq 10$ days) novae per observing season⁶, where, as before, f is the fraction of SNe Ia accreting in the unstable nuclear burning regime shortly before the explosion (at $M_{\text{WD}} > 1.3 M_{\odot}$). Furthermore, if all the observed POINT-AGAPE novae were to become SNe Ia (i.e., $f = 0.07$), a PTF program with regular monitoring of M31 several times per week should be detecting ~ 70 fast novae per observing season.⁶ These numbers are significantly larger than the currently observed rate of fast novae, suggesting that $f \ll 1$.

2.5 Discussion

With the progenitors of SNe Ia still eluding direct detection, there is a growing consensus that they may be a heterogeneous class of objects united by the final outcome – thermonuclear disruption of the WD. Among other possibilities, various types of accreting binary systems have been proposed as a candidate. The fate of the accreted material is mainly determined by the WD mass and the mass accretion rate (e.g., Fujimoto 1982; Nomoto et al. 2007; Wolf et al. 2013). In the picture that has become fairly standard, there is a rather narrow range of the mass-accretion rates around \sim a few $\times 10^{-7} M_{\odot} \text{ yr}^{-1}$ (varying with the WD mass) in which the nuclear burning is steady and proceeds at the rate determined by the supply of the material through the accretion process. Below this range, the nuclear burning is subject to thermal instability, giving rise to the phenomenon of novae. In the classical picture, copious amounts of material are lost in the nova explosion, especially at the lower mass-accretion rates ($\dot{M} \lesssim 10^{-7} - 10^{-8} M_{\odot} \text{ yr}^{-1}$ in the Yaron et al. (2005) calculations, for example), rendering the growth of the WD mass impossible or insignificant in the context of SN Ia progenitors. Importantly, several authors have found that the transition from unstable to stable burning is sharp – there is a discontinuity in the stability of burning, with the large amplitude flashes occurring very close to the stability strip (e.g., Wolf et al. 2013; Kato et al. 2014).

However, the main aspects of this picture have been contested by several authors. First,

⁶This estimate is valid for a random observing pattern. For the particular schedule of PTF observations in 2009–2010 shown in Fig. 2 of Cao et al. (2012), this needs to be decreased by a factor of a few because there were extended gaps in the observing schedule; more accurate calculations are beyond the scope of this work.

the existence of the stability strip has been questioned (e.g., Idan et al. 2013; Starrfield 2014; Hillman et al. 2015). In fact, no stable burning is reported in the Yaron et al. (2005) tables either, although the ejected mass becomes zero at the highest mass-accretion rates. Second, it has been suggested that mass accumulation at appreciable rates is possible in the broad range of the mass-accretion rates, including those traditionally considered to be associated with the nova regime. In fact, it has been claimed that any mass accumulation by the WD is associated with regular thermonuclear explosions (e.g., Starrfield 2014; Hillman et al. 2015). In a related development, progenitor models have been proposed that involve WDs accreting in the presumably unstable nuclear burning regime throughout or at least a part of their accretion history (e.g., Starrfield et al. 1985; Hachisu & Kato 2001; Hillman et al. 2015). Further support for these ideas is lent by the realization that recurrent novae (RNe) may host WDs with masses very close to the Chandrasekhar mass limit, the most famous example being RS Oph (Sokoloski et al. 2006; Hachisu & Kato 2001). This led to the suggestion that novae in general and recurrent novae in particular may be an important channel producing some (unknown) fraction of SNe Ia (see, for example, Wood-Vasey & Sokoloski 2006; Patat et al. 2011; Hachisu & Kato 2001; Pagnotta & Schaefer 2014).

In this chapter, we pointed out that the population of WDs with unstable nuclear burning, sufficient to account for a non-negligible fraction of SNe Ia, would reveal themselves through significantly enhanced nova rates in galaxies. We thus propose that the contribution of novae to the observed SN Ia rates can be assessed through the nova statistics in nearby galaxies. We demonstrated that given the completeness-corrected nova rate in M31 of $\approx 65 \text{ yr}^{-1}$ (Darnley et al. 2006), novae can only produce a small fraction of SNe Ia, at the maximal rate of $\lesssim (1-5) \times 10^{-4} \text{ yr}^{-1}$, assuming typical mass-accretion rates of progenitors in the range, $\dot{M} \sim (1-5) \times 10^{-7} M_{\odot} \text{ yr}^{-1}$. This constitutes no more than 2–7% of the total SN Ia rate in M31. Moreover, we predicted that M31 surveys of the PTF class should be detecting on the order of $1000 \times f$ fast ($t_2 \leq 10$ days) novae every year, where f is the fraction of SNe Ia accreting in the unstable nuclear burning regime shortly before the explosion (at $M > 1.3 M_{\odot}$). The fact that < 50 such fast novae have been recorded/detected in the course of about a century of M31 monitoring (see the optical nova catalog maintained by MPE from footnote 2) suggests that the fraction f is small, on the order of $f \lesssim 10^{-3}$. However, an accurate completeness analysis of the M31 PTF survey is needed before a robust quantitative conclusion can be made.

Equation (2.3) shows that the calculation of the total number of novae per SN Ia depends on the theory of thermonuclear burning on the WD surface only through the ignition mass ΔM_{ign} . This quantity is derived from sufficiently well understood physical principles and has been computed by a number of groups (for example, Fujimoto 1982; Townsley & Bildsten 2004; Yaron et al. 2005; Wolf et al. 2013; Kato et al. 2014 and others). A comparison of some of the results is shown in Fig. 2.6. The plot shows that results of different calculations agree quite well, within a factor of ~ 2 . The agreement is quite good even between authors drawing opposite conclusions regarding the existence of the stability strip. In the parameter range of interest, there is a good agreement between analytical (Fujimoto 1982) and more sophisticated numerical calculations, as well as between single flash (Fujimoto 1982; Starrfield 2014) and multicycle (Yaron et al. 2005; Wolf et al. 2013)

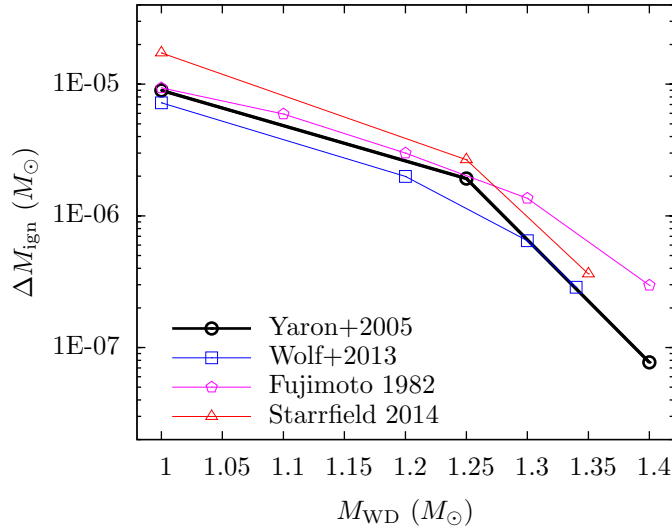


Figure 2.6: Comparison of the ignition mass of the nova as computed by different authors. The ignition mass is shown as a function of the WD mass for a mass accretion rate $\dot{M} = 10^{-7} M_{\odot} \text{ yr}^{-1}$. The Wolf et al. (2013) results are obtained from their Fig. 8; Fujimoto (1982) from their Fig. 7; Starrfield (2014) from their Figs. 2–3.

calculations. We note that the latter two probably provide a more accurate representation of the accreting WD, and their results agree to much better than a factor of ~ 2 . We thus conclude that the calculations of the total number of novae produced by an SD SN Ia progenitor presented in this chapter are sufficiently robust and do not depend on the details of the underlying nova models, including their conclusions regarding the existence of the stability strip.

In our calculations we used the results of Prialnik & Kovetz (1995) and Yaron et al. (2005), who computed the most extensive grid of multicycle nova evolutionary models to date. The ignition masses from their calculations agree well with the results of other groups, as already discussed above (Fig. 2.6). Furthermore, the grid of their models covers the parameter space occupied by the observed novae well and approximately reproduces observed correlations between various nova parameters (Prialnik & Kovetz 1995; see also Walder et al. 2008). The peak magnitudes and light-curve decay times predicted by their models are compared with observations in Fig. 2.7. Each curve in this plot corresponds to a given combination of \dot{M} and T_{WD} , with M_{WD} changing along the curve. \dot{M} extends from 10^{-7} to $10^{-11} M_{\odot} \text{ yr}^{-1}$, thus covering the typical range expected in nova host systems. Peak magnitudes in the visual band were computed from the peak bolometric luminosity reported in Prialnik & Kovetz (1995) and Yaron et al. (2005) by applying the bolometric correction of an A5V star, as is commonly done in such estimates (Shafter et al. 2009; Kasliwal et al. 2011). The light-curve decay times were computed from the mass-loss times as explained in Sect. 2.2.

Figure 2.7 shows that the observed range of the light-curve decay times t_2 is fully sampled by the nova models with WD masses varying from ≈ 0.4 – $0.65 M_{\odot}$ to ≈ 1.3 –

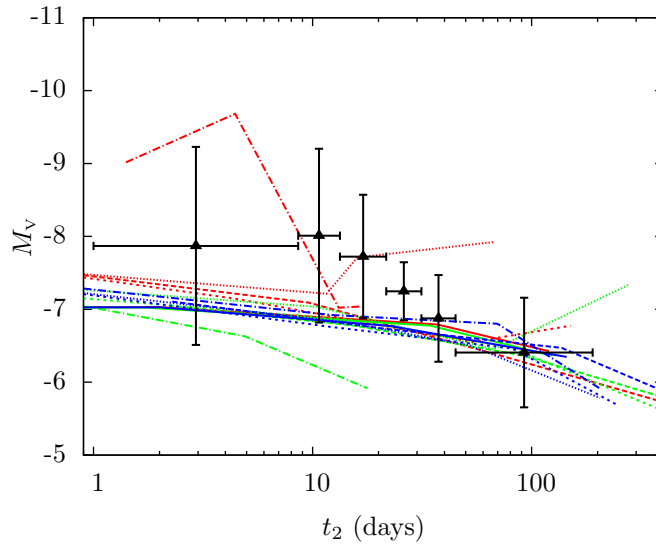


Figure 2.7: Comparison of the data shown in Fig. C.1 with the results of multicycle nova models of Yaron et al. (2005). The black triangles and vertical error bars show the average peak magnitudes and their rms deviation for the novae grouped in equipopulated bins over the t_2 time, and the curves are corresponding relations for the nova models of Yaron et al. (2005). The red, green and blue curves correspond to WD core temperature of 10^7 K, 3×10^7 K and 5×10^7 K, respectively. The solid curves are for $\dot{M} = 10^{-7} M_{\odot} \text{ yr}^{-1}$, dashed curves for $\dot{M} = 10^{-8} M_{\odot} \text{ yr}^{-1}$, short dashed curves for $\dot{M} = 10^{-9} M_{\odot} \text{ yr}^{-1}$, dotted curves for $\dot{M} = 10^{-10} M_{\odot} \text{ yr}^{-1}$, and dot-dashed curves for $\dot{M} = 10^{-11} M_{\odot} \text{ yr}^{-1}$.

$1.4 M_{\odot}$. The models also reproduce the average trend in the peak magnitude with t_2 quite well. The small offset in magnitude between the models and data is reduced further if one takes into account that the theoretical models may underestimate the true value by up to 0.75 mag, as discussed in Prialnik & Kovetz (1995). These models, however, do not reproduce the scatter seen in the observed data. This suggests that the scatter may be caused by additional factors, other than those already included in the calculations of Yaron et al. (2005) (e.g., orientation effects and interaction of the ejecta with the disk and the donor star). For this reason, we used the parameters of observed novae to draw the nova peak magnitudes in our Monte Carlo simulations in Sect. 2.4. However, the overall agreement between the models of Yaron et al. (2005) and the data suggests that the models reproduce the global characteristics of the nova light curves sufficiently well.

The famous recurrent nova M31N 2008-12a appears to be somewhat (by about ~ 1 – 2 mag) underluminous as compared to the predictions of Yaron et al. (2005) as well as to its counterparts with similarly short decay times (Fig. C.1). Of course, it may be just a faint tail of the distribution approximately centered near the value predicted by Yaron et al. (2005) for the corresponding range of decay times. However, there is another possibility: it might present the bright tail of the so far unknown population of fast and underluminous novae hosted by massive WDs near the Chandrasekhar mass limit. Although intriguing, this possibility seems at present less likely. The main argument is that M31N 2008-12a is up to three magnitudes brighter than the typical sensitivity limit of the PTF M31 survey, and despite about six years of continuous PTF observations (since August 2009), no other similar nova was discovered. A more quantitative analysis of the latter possibility is beyond the scope of this work.

Shafter et al. (2015) have undertaken a census of the recurrent nova population in M31 based on the positional coincidence of about $\sim 10^3$ novae recorded in modern astronomy. They identified 16 recurrent novae and candidates, but they estimated that the detection efficiency of the recurrent systems may be as low as $\sim 10\%$ of that of classical novae. Based on these data and assuming that recurrent nova systems typically accrete at $10^{-7} M_{\odot} \text{ yr}^{-1}$, they constrained their contribution to the SN Ia rate at the level of $\lesssim 2\%$. This upper limit is comparable to the limits we derived here. In particular, for the $10^{-7} M_{\odot} \text{ yr}^{-1}$ accretion rate, we constrained the contribution of all slow ($t_2 \gtrsim 10$ days) novae, irrespective of their recurrence times, to $\lesssim 7\%$.

The upper limit of ≈ 2 – 7% we obtained is comparable to the upper limits on other versions of the SD scenario. Based on the luminosity of unresolved soft X-ray emission in a sample of nearby elliptical galaxies observed by *Chandra*, Gilfanov & Bogdán (2010) constrained the contribution of supersoft X-ray sources (i.e., stably nuclear burning WDs located in the stability strip) to $\lesssim 5\%$. Johansson et al. (2014) used the recombination line $\lambda 4686 \text{ \AA}$ of HeII to limit the EUV emission from lower temperature sources – those that escaped the X-ray based analysis of Gilfanov & Bogdán (2010) due to their very soft spectra and absorption by the ISM. Such low-temperature sources can be associated with the low-mass WDs or with the rapidly accreting sources above the stability strip (Hachisu et al. 1996). In particular, Johansson et al. (2014) applied the diagnostics suggested by Woods & Gilfanov (2013) to stacked SDSS spectra of $\sim 10^4$ retired galaxies and constrained

the contribution of accreting WDs with photospheric temperature in the range $\sim (1.5\text{--}6) \times 10^5$ K to $\lesssim 5\text{--}10\%$. These upper limits can be tightened further and their photospheric temperature range can be extended using intrinsically brighter forbidden lines of metals (Woods & Gilfanov 2014). In particular, Johansson et al. (in preparation) used the $\lambda 6300$ Å forbidden line of neutral oxygen to derive an upper limit of about a few per cent on the contribution of accreting WDs with the photospheric temperature in the $\sim 10^5\text{--}10^6$ K range. Combined together, these constraints limit the role of the main variations of the SD scenario in producing SNe Ia. Even when (very conservatively) summed independently, their total contribution to the observed SN Ia rate cannot exceed $\lesssim 10\text{--}20\%$. Alternatively, a typical supernova could not have accreted more than $\lesssim 0.03\text{--}0.05 M_{\odot}$ in each of the above mentioned regimes – that is, below, in, or above the stability strip.

We assumed, as is commonly accepted (e.g., Maoz et al. 2014), that SNe Ia are produced by the WDs exploding at the Chandrasekhar mass. However, sub-Chandrasekhar (e.g., Woosley & Weaver 1994; Bildsten et al. 2007; Sim et al. 2010; Kromer et al. 2010) as well as super-Chandrasekhar (e.g., Howell et al. 2006; Liu et al. 2010; Kamiya et al. 2012) detonations are also being considered by a number of authors. If sub-Chandrasekhar detonations contribute significantly to the SN Ia rate, the nova-based constraints may need to be relaxed. Indeed, if a WD explodes before reaching the Chandrasekhar mass, the distribution shown in the right panel of Fig. 2.2 will be cut off at the t_2 time, corresponding to the explosion mass (cf. Fig. 2.1). Correspondingly, the upper limit on the contribution of novae to SN Ia production will increase, as n_{nov} in Eq. (2.6) decreases. For example, if a typical SN Ia progenitor WD explodes at $1.3 M_{\odot}$, the entire population of fast novae ($t_2 < 10$ days) will not be produced by the sub-Chandrasekhar supernova progenitors, but the constraints derived from the POINT-AGAPE survey will still hold in full. Obviously, in this scenario the observed fast novae are not the progenitors of sub-Chandrasekhar supernovae. If the typical explosion mass is even lower, for example, $1.1 M_{\odot}$, current nova statistics become unconstraining. In the super-Chandrasekhar models the result depends on the properties of nova explosions on the surface of a rotating WD, which are currently not well understood. However, at present there is no evidence that either sub- or super-Chandrasekhar models contribute dominantly to the SN Ia rates, therefore constraints on the nova-channel derived in this chapter should hold for the bulk of supernovae.

Finally, we note that we used M31 galaxy to tune our calculations and compare their results with observations because of its proximity and relatively well-known nova population. However, our results can be easily generalized to other galaxies of similar age. Observations of several nearby galaxies show that they have comparable nova rates per unit stellar mass (e.g., Shafter et al. 2014). As the same is true for the supernova rates in galaxies of similar morphological type, the constraints on the contribution of the nova channel to supernova rate are expected to apply to other nearby galaxies of similar age and morphological type.

2.6 Conclusions

We propose that the statistics of novae in nearby galaxies is a sensitive diagnostic of the population of accreting WDs with unstable nuclear burning and can be used to constrain the role of this channel in producing SNe Ia. Using multicycle nova models of Yaron et al. (2005), we computed the number and temporal distribution of novae produced by a successful SN Ia progenitor, assuming that it accretes in the unstable nuclear burning regime throughout its accretion history. We predicted the total number of novae to be $\approx 6.5\text{--}7.7 \times 10^5$ per supernova, assuming that a typical SN Ia progenitor accretes material at the rate of $\approx (1\text{--}5) \times 10^{-7} M_{\odot} \text{ yr}^{-1}$. Using the nova rate in M31 as measured by the POINT-AGAPE survey, $\approx 65 \text{ yr}^{-1}$ (Darnley et al. 2004, 2006), we estimated the maximal contribution of the nova channel in producing SNe Ia. Considering relatively slow novae, with light-curve decay times $t_2 \gtrsim 10$ days, whose characteristics are compatible with the observed novae from the POINT-AGAPE catalog (Darnley et al. 2006), we concluded that their contribution to the observed SN Ia rates cannot exceed $\approx (1\text{--}5) \times 10^{-4} \text{ yr}^{-1}$. This constitutes less than 2–7% of the total SN Ia rate in M31.

An even more sensitive diagnostic can be provided by fast novae, which originate from the most massive WDs and are characterized by the lowest ignition masses. To use their potential, high-cadence nova surveys are required. We investigated how the detection efficiency of a generic nova survey of M31 depends on its limiting magnitude and temporal sampling. We found that a survey with a limiting magnitude of $m_R \approx 22$ will detect about $\approx 80\text{--}90\%$ of the predicted fast novae ($t_2 \lesssim 10$ days) provided that observations are conducted at least every second or third night. To detect more than 50% of such novae in a survey with observations carried out every night, its limiting magnitude has to be $m_R \gtrsim 20$. Such surveys are expected to detect on the order of $\gtrsim 1000 \times f$ fast novae per observing season in M31, where f is the fraction of SN Ia progenitors that accreted in the unstable nuclear burning regime while accumulating the final $\Delta M \approx 0.1 M_{\odot}$ before the supernova explosion. This is significantly larger than the currently observed rate of fast novae in M31, suggesting that $f \ll 1$. However, high-cadence surveys with accurately characterized completeness are required to place robust constraints on the value of f . Existing and upcoming surveys such as the PTF, Pan-STARRS, and LSST are well-suited for this task.

The predicted number of novae per SN Ia should not depend strongly on the details of the underlying nova models because they are only determined by the ignition mass of the envelope. This quantity is derived from sufficiently well understood physical principles, and the results of computations by different groups agree quite well, even among those at odds about the existence of the stability strip. The division of the total number between slow and fast novae depends on the assumptions made about the shape of their light curves. To this end, we used the multicycle nova models of Yaron et al. (2005), which are known to sample the observed range of the nova decay times correctly and reproduce various correlations between observed nova properties. Calculations based on two different timescales tabulated in Yaron et al. (2005) – mass-loss and bolometric, give similar results leading to the same conclusions. Finally, in our incompleteness simulations we used the observed nova light curves and their peak magnitudes, therefore these results are independent of the theoretical

nova models.

Chapter 3

Upper limits on mass accumulation by white dwarfs in the unstable nuclear burning regime

3.1 Introduction

Binary evolution calculations predict that a typical successful supernova progenitor can pass through all three nuclear burning regimes (e.g., Chen et al. 2014). Accounting for this possibility, we derive in this chapter the constraint on the fraction of mass that can be accumulated at any given WD mass in the nova regime of the SD scenario; let us call it the constraint function, $f(M_{\text{WD}})$. To this end, we require a WD mass proxy in observed novae. As discussed in section 2.2, for a given mass accretion rate and core temperature of the WD, the nova decline time t_2 is a function of WD mass (see also Fig. 2.1). Furthermore, for a given supernova rate in M31 $\dot{N}_{\text{SNIa}} = 7.15 \times 10^{-3} \text{ yr}^{-1}$ (cf. 2.3.1), the *predicted* t_2 distribution of novae produced by these SNe Ia can be easily obtained from Eq. (2.5) (see also Fig. 2.2 right panel), by multiplying it with \dot{N}_{SNIa} . Comparing this distribution to the observed t_2 distribution, we can obtain the constraints on the mass accumulation by SN Ia progenitors in the nova regime.

3.2 Derivation of $f(M_{\text{WD}})$

We can use the information contained in the differential t_2 distribution of detected novae in order to constrain the fraction of mass which can be accumulated by WDs in the nova regime at different WD masses. To this end, we compare the observed and predicted differential t_2 distributions of the nova rate. In particular, we consider the following. In the SD scenario, as the WD mass increases from M_{WD} to $M_{\text{WD}} + \delta M_{\text{WD}}$, their population will produce (cf. Eqs. 2.4, 2.5)

$$\delta \dot{N}_{\text{pred}} = \dot{N}_{\text{SNIa}} \frac{\delta M_{\text{WD}}}{\Delta M_{\text{ign}}(M_{\text{WD}}, \dot{M}, T_{\text{WD}})} \quad (3.1)$$

nova events per year with the light curve decay time between t_2 and $t_2 + \delta t_2$ where $t_2 = t_2(M_{\text{WD}}, \dot{M}, T_{\text{WD}})$ is determined by the nova theory (Fig. 2.1) and

$$\delta t_2 = \frac{dt_2}{dM} \delta M_{\text{WD}} \quad (3.2)$$

with dt_2/dM also given by the theory. This can be compared with the observed rate of events in the corresponding t_2 interval, corrected for incompleteness of the survey:

$$\delta \dot{N}_{\text{obs}} = \frac{1}{\eta(t_2)} \frac{d\dot{N}_{\text{obs}}}{dt_2} \delta t_2. \quad (3.3)$$

Their ratio, $f = \delta \dot{N}_{\text{obs}} / \delta \dot{N}_{\text{pred}}$ equals:

$$f(M_{\text{WD}}) = \frac{1}{\eta(t_2)} \frac{d\dot{N}_{\text{obs}}}{dt_2} \frac{dt_2}{dM} \frac{1}{\dot{N}_{\text{SNIa}}} \Delta M_{\text{ign}}. \quad (3.4)$$

With Eq. (2.5), one can transform Eq. 3.4 to an obvious expression

$$f(M_{\text{WD}}) = \frac{1}{\eta(t_2)} \frac{d\dot{N}_{\text{obs}}}{dt_2} \left(\frac{d\dot{N}_{\text{pred}}}{dt_2} \right)^{-1}. \quad (3.5)$$

$f(M_{\text{WD}})$ has the following meaning. In order for the WD to increase its mass from M_{WD} to $M_{\text{WD}} + \delta M_{\text{WD}}$, it needs to accumulate mass δM_{WD} . $f(M_{\text{WD}})$ constrains the maximum fraction of this mass increment δM_{WD} which can be accumulated in the nova regime.

In order to estimate $f(M_{\text{WD}})$, we compute the observed differential rate of novae $d\dot{N}_{\text{obs}}/dt_2$ combining the nova sample of Darnley et al. (2004, 2006), which contains only $t_2 > 10$ days novae (see section 2.3.4), with the sample from Arp's survey of M31 (Arp 1956) for $t_2 \lesssim 10$ days. The latter sample lacks completeness information with respect to the decline times of novae, which is required for our computation of $f(M_{\text{WD}})$. To recover this information, we make an approximate incompleteness calculation as detailed in Sect. 3.3.

3.3 Incompleteness correction of Arp's survey of M31 (1953-1955)

We apply the method developed by Soraisam & Gilfanov (2015) for an approximate incompleteness calculation of Arp's survey of M31 (1953-1955) (Arp 1956). We carry out Monte-Carlo simulations taking into account the limiting magnitude and the observing pattern of the survey, and by using a scalable template nova light curve and the observed maximum magnitude – rate of decline relation from Appendices B and C. We then compute the fraction of detected novae as a function of the decline time t_2 .

Arp (1956) observed M31 for two seasons between June 1953 and January 1955 using the 60-inch telescope on Mount Wilson resulting in the discovery of 30 novae. The survey

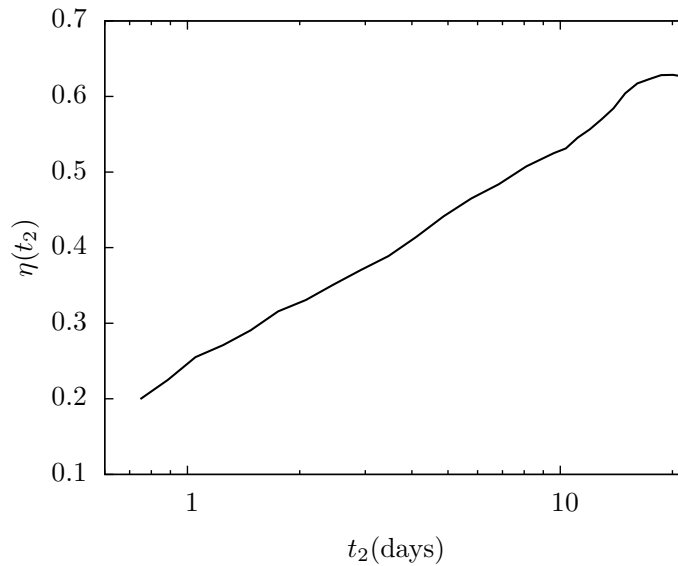


Figure 3.1: The detection efficiency η of Arp’s survey of M31 (1953-1955), approximately computed using the observation details provided in the original Arp’s publication and the online database of the Carnegie Observatories’ plate archive, as described in section 3.3. The detection efficiency is the fraction of novae with the given light curve decay time t_2 detected in the survey.

was carried out using photographic plates of 5×7 inch size at the focal plane with a plate scale of $24 \text{ arcsec mm}^{-1}$, thus covering ~ 1 square degree of the galaxy with an average limiting magnitude of $m_{pg} = 20$ (Capaccioli et al. 1989). The exposures were primarily centered at two points $10'$ on either side of the nucleus along the major axis. Additional exposures centered on the nucleus of the galaxy as well as $20'$ on either side of the nucleus along the major axis were also made. For our calculations, we have considered the primary exposures (which also include all the 30 detected novae in this survey) and the exposures centered on the nucleus, excluding a circular region of radius $2'$ in the innermost part, where Arp’s survey is known to be incomplete (Capaccioli et al. 1989).

The observing patterns for this survey are not described in the original Arp’s publication Arp (1956). However, the photographic plates from Arp’s survey are in the archive of the Carnegie Observatories and the details of the plates have been cataloged in their online database¹. From this database, we obtain the exact observing dates. The observing times for multiple plates taken on the same night are, however, not available. Nevertheless, Arp (1956) has described the observations each night to be repeated every hour or so, and therefore we assume the same for the plate entries in the database. The resulting completeness curve of Arp’s survey is shown in Fig. 3.1 as a function of the light curve decay time t_2 . We should note that the above calculations have not accounted for the spatial variations in the internal optical extinction in M31. However, extinction variations

¹<http://plates.obs.carnegiescience.edu/PAST/search/>

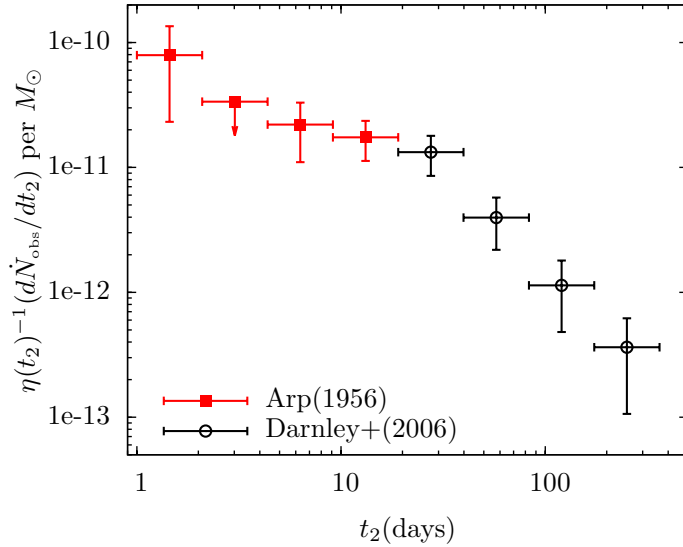


Figure 3.2: Observed differential nova rate distribution in M31 obtained using the nova sample of Arp (1956) for $t_2 \leq 20$ days and that of Darnley et al. (2004) for $t_2 > 20$ days, after correcting for incompleteness (see section 3.4 for details).

should not have a significant effect on their detection efficiency, as shown by Soraisam & Gilfanov (2015). Furthermore, the detection of novae by Arp was not automated and it involved some human intervention, as was the case for all pre-CCD surveys. Therefore, an accurate calculation of the completeness of Arp’s catalog is impossible. However, the approximate completeness computed here is a reasonable first approximation and allows us to estimate the population of fast novae in M31 (see below). The existing high cadence surveys such as the iPTF and Pan-STARRS, would allow a more efficient detection of fast novae. A more precise determination of their population in M31 then should be and will be performed using these modern facilities.

3.4 Nova rate distribution in M31

In order to obtain the t_2 distribution of novae in M31 we will combine the data of the Arp’s survey with the nova catalog of Darnley et al. (2004).

For the nova sample of Darnley et al. (2004) obtained from the POINT-AGAPE (Pixelensing Observations with the Isaac Newton Telescope – Andromeda Galaxy Amplified Pixels Experiment) survey of M31, Darnley et al. (2006) carried out a comprehensive analysis of the spatial completeness of the survey. However, this catalog is not complete for fast novae, due to insufficient cadence of the POINT-AGAPE survey (Darnley et al. 2006). We therefore combine the Arp’s sample of fast novae ($t_2 \leq 20$ days), corrected for incompleteness using the results in Sect. 3.3, and the nova sample of Darnley et al. (2004) for $t_2 > 20$ days, using the completeness value of $\approx 25\%$ obtained from Table 3 of Darnley et al. (2006) for correction. In particular, we use their $\theta = 1$ case. It is still an

open question whether the specific nova rates (per unit mass) in the bulge and disk of M31 differ much. Darnley et al. (2006) have shown that the overall nova rate in M31 derived from their data does not depend significantly on their ratio. Therefore, we assumed for simplicity that specific nova rates in the bulge and disk are same (i.e., $\theta = 1$ case of Darnley et al. 2006).

The nova samples of Arp (1956) and Darnley et al. (2004) are then normalized by the stellar mass contained in the field of view (FOV) of the corresponding survey. For Arp’s survey, we estimate the mass enclosed by the (primary) FOV using the Spitzer $3.6\mu\text{m}$ mosaic image of M31 from Barmby et al. (2006). This image is background subtracted and the contamination from foreground and background objects is insignificant, contributing less than $\sim 5\%$ to the luminosity within the FOV. Then, using the K-band mass-to-light ratio, M/L_K , of 0.80 (solar units) derived from Bell & de Jong (2001) using the color $B - R = 1.5$ for M31 (Walterbos & Kennicutt 1987), we calculate the mass enclosed assuming $K - [3.6] = 0.3$ (Barmby et al. 2006; see also Bogdán & Gilfanov 2010). We thus obtain the stellar mass within the FOV of the survey to be $\approx 6 \times 10^{10} M_\odot$. For the POINT-AGAPE survey, the mass is estimated using the fraction of stellar light enclosed by the survey FOV from Table 3 in Darnley et al. (2006), which gives us a value of $\approx 4 \times 10^{10} M_\odot$. The resulting combined t_2 distribution of the incompleteness corrected observed nova rate in M31, normalized to unit M_\odot , is shown in Fig. 3.2. Its total rate is $\approx 106 \text{ yr}^{-1}$; this value is larger than 75 yr^{-1} derived by Darnley et al. (2006) for their $\theta = 1$ model because of the contribution of the fast novae.

3.5 Constraints on mass accumulation in the nova regime using the M31 nova sample

After obtaining the observed t_2 distribution in novae in M31 (section 3.4), albeit with an approximately incompleteness-corrected fast nova sample from Arp (1956), it is straightforward to compute $f(M_{\text{WD}})$ using this distribution along with the predicted one from the SD scenario (Fig. 2.2). To this end, the theoretical distributions computed for one SN Ia is normalized to the SN Ia rate in M31, $7.15 \times 10^{-3} \text{ yr}^{-1}$. The results are shown in Fig. 3.3, for the mass accretion rates of 10^{-7} , 10^{-8} and $10^{-9} M_\odot \text{ yr}^{-1}$, assuming WD core temperature of 10^7 K (Sect. 2.2). Note that higher WD masses in Fig. 3.3 correspond to shorter t_2 times in Figs. 2.2 and 3.2.

From Fig. 3.3 one can see that for lower mass accretion rates (10^{-8} and $10^{-9} M_\odot \text{ yr}^{-1}$) and lower WD masses $M_{\text{WD}} \lesssim 1\text{--}1.1 M_\odot$, the nova regime can fully account for the mass required to be accreted at the given WD mass in the SD scenario. For $\dot{M} = 10^{-7} M_\odot \text{ yr}^{-1}$, $f(M_{\text{WD}})$ does not extend below $1 M_\odot$ since there is stable nuclear burning at the lower WD masses (see for example Wolf et al. 2013). Still, for all mass accretion rates, $10^{-9}\text{--}10^{-7} M_\odot \text{ yr}^{-1}$, quite significant, at the level of $\sim 10\text{--}60\%$, mass accumulation by WDs in the nova regime appears possible for WDs with masses $1.10 \lesssim M_{\text{WD}} \lesssim 1.30 M_\odot$. However, in the most massive WDs ($M_{\text{WD}} > 1.3 M_\odot$), this regime can only account for

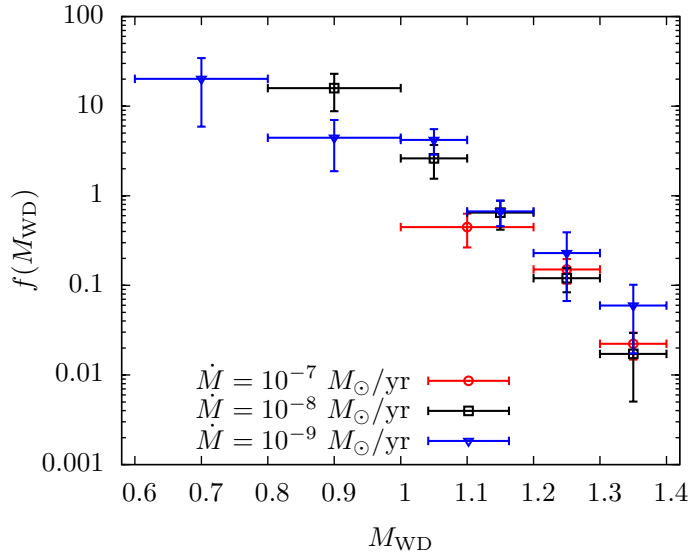


Figure 3.3: Constraints on the fraction of mass that can be accreted in the nova regime at different WD masses derived using the differential nova rates shown in Figs. 3.2 and 2.2. For $\dot{M} = 10^{-7} M_{\odot} \text{ yr}^{-1}$, there is stable nuclear burning at $\lesssim 1 M_{\odot}$, hence there is a cut-off at $\approx 1 M_{\odot}$.

$\sim 6\%$ of their mass accumulation for the lowest mass accretion rate $\dot{M} = 10^{-9} M_{\odot} \text{ yr}^{-1}$; the fraction decreases to a mere $\sim 2\%$ for the higher mass accretion rates 10^{-8} and $10^{-7} M_{\odot} \text{ yr}^{-1}$. These results thus constrain the occurrence of the SN Ia explosion in the nova regime.

3.6 Summary

Supplementing the slow ($t_2 > 10$ days) nova sample from Darnley et al. (2004, 2006), whose precise completeness information is available, with the fast nova sample from Arp (1956), we obtained the observed t_2 distribution in novae in M31. The latter sample lacked completeness information, and therefore, we made an approximate completeness calculation of Arp’s M31 survey (Sect. 3.3). In particular, this allowed us to probe the massive WDs, given the inverse relation between nova decline time and WD mass (cf. Fig. 2.1). Then using the observed and predicted t_2 distributions in novae, we have demonstrated in this chapter how constraints on mass accumulation in the nova regime of the SD scenario can be obtained (Sects. 3.2 and 3.5).

We find that considerable mass accumulation, at the level of $\sim 10\text{--}60\%$, is possible for WDs with masses $1.10 \lesssim M_{\text{WD}} \lesssim 1.30 M_{\odot}$. In the more massive WDs, the calculations presented in this chapter show that this regime can only account for $\sim 2\%$ of their mass accumulation, considering mass accretion rates relevant in the SD scenario, without coming into conflict with the observed nova statistics in M31 (Fig. 3.2). This result then implies that final stages of the mass accumulation and the SN Ia explosion in the majority of

SNe Ia cannot occur in the low \dot{M} regime, when the nuclear burning is unstable. With the present high cadence surveys that would be more sensitive to fast novae (for example the PTF survey), we would be able to obtain a larger sample of fast novae and to accurately quantify its completeness. Following this, we shall be able to improve the constraints above in the immediate future (cf. Chapter 5).

Chapter 4

Populations of post-nova supersoft X-ray sources

4.1 Introduction

After the optical outburst, novae are equally interesting to study through their supersoft X-ray emission during their retreat to quiescence. The post-outburst soft X-ray emission results from quiescent nuclear burning of the remnant hydrogen envelope on the WD at a nearly constant bolometric luminosity (cf. 1.1.3). This leads to the peak of the spectrum shifting to shorter wavelengths as the photosphere of the WD contracts, following the expansion of the envelope ejected during the nova (Sparks et al. 1976; Sala & Hernanz 2005b; Wolf et al. 2013). The soft X-ray emission also occurs during the peak of the TNR, but only for a very brief period that makes its detection more difficult (see Krautter 2002 and references therein). The post-outburst emission, however, lasts until the remnant envelope is nearly exhausted. Observations of the post-nova supersoft X-ray emission provide a means to verify the nova evolution models and to directly probe parameters of the WD and the nova explosion. For example, the duration of the post-outburst SSS phase sheds light on the WD mass and the mass ejected during the nova explosion, as was shown by Tang et al. (2014c) and Henze et al. (2015) for the recurrent nova M31N 2008-12a in M31. Such observational constraints will help fill the missing gaps in theoretical modelling of classical and recurrent novae (e.g., Starrfield et al. 1974a,b; Prialnik 1986; Prialnik & Kovetz 1995; José & Hernanz 1998; see also Bode & Evans 2008 for a detailed review on various aspects of novae).

On the theoretical front of the post-nova evolution study, Tuchman & Truran (1998) invoked the analogy of this phase with the post AGB phase of stellar evolution and derived a modified core mass – luminosity relation that accounted for the post-nova metal enrichment in the remnant envelope. They applied this relation to observed novae and found good agreement with the observed SSS duration of GQ Mus and V1974 Cyg. Further, Sala & Hernanz (2005b) modelled the post-nova evolution for various WD masses by constructing grids of stable hydrogen burning WD envelopes for four different chemical compositions.

The photospheric properties of the post-nova SSSs derived from observations, in particular the evolution of their effective temperatures, were then compared with the models to constrain the WD mass, and the envelope mass and composition. These models were applied in the above manner to V1974 Cyg by Sala & Hernanz (2005a) and the WD properties for V1974 Cyg were determined.

Most recently Wolf et al. (2013) have performed multicycle evolutionary calculations of the post-outburst phase of novae using the MESA (Modules for Experiments in Stellar Astrophysics) code (Paxton et al. 2011, 2013). Their calculations covered a grid of WD masses from $0.6 M_{\odot}$ to $1.34 M_{\odot}$, accreting solar composition material. Given that the mass-loss mechanism in novae is still an unresolved issue, for their calculations Wolf et al. (2013) employed two mass-loss prescriptions, viz., super Eddington winds (SEW) and Roche lobe overflow (RLOF). In these prescriptions, the WD undergoes mass-loss until its photospheric luminosity (L) becomes less than an effective local Eddington luminosity (L_{Edd}) in the SEW case, or until its radius (R) becomes less than the Roche lobe radius (R_{RL}) in the RLOF case (see Wolf et al. 2013 for more details). Their results were found to agree with the measurements of effective blackbody temperature (T_{eff}) and turn-off time of the soft X-ray emission from novae observed in M31 (Henze et al. 2011, 2013) as well as Galactic sources (see references in Wolf et al. 2013). The ejecta masses predicted by their models were also consistent with the ones derived by Henze et al. (2011) for the observed novae in M31 based on their soft X-ray emission turn-on time. Moreover, Tang et al. (2014c) used the results of Wolf et al. (2013) to show that the supersoft phase of M31N 2008-12a was most consistent with nuclear burning on the surface of a WD in the mass range of $1.32 - 1.36 M_{\odot}$, a more precise result than the lower bound provided by the recurrence time alone.

On the observational front, much effort has been made following the work of Pietsch et al. (2005, 2007), which established the prominence of novae as the major class of SSSs in M31. Since then dedicated X-ray monitoring campaigns have been carried out with *XMM-Newton* and *Chandra* in order to search for X-ray counterparts of optically observed novae in the central region of M31. The results from these observations have been published by Henze et al. (2010, 2011, 2014b). The total number of such novae with detected X-ray counterparts stands now at 79 and 51 of them have their spectra classified as supersoft (Henze et al. 2014b). These observational results offer an unprecedented opportunity to study the nova population post-eruption.

In this chapter, we predict the number of post-nova SSSs in M31 theoretically and compare our predictions with observations. To this end, we use an extended set of multicycle post-nova evolutionary tracks from the calculations of Wolf et al. (2013), covering a much finer grid of the WD masses than in the original publication, ranging from $0.6 M_{\odot}$ to $1.36 M_{\odot}$. For the requisite WD mass distribution in novae, we derive four different forms, two based on observed optical nova statistics in M31 and two on simple theoretical considerations. With these two ingredients, we predict the population of post-nova SSSs in M31 and compute their luminosity function and the T_{eff} distribution. We also predict the number of these sources to be detected in the the dedicated *XMM-Newton* monitoring of M31 from Henze et al. (2010, 2011), and compare it with the observed number.

Table 4.1: Models of the WD mass distribution in novae

Model ID	Description
M-10	Distribution obtained using the t_2 distribution of optically observed novae in M31 (Fig. 3.2) and relation between t_2 and M_{WD} from Yaron et al. (2005), assuming WD core temperature of 10^7 K
M-30	Similar to the model M-10, but assuming the WD core temperature to be 3×10^7 K for Yaron et al. nova models
M-flat	Flat distribution
M-TL	Distribution from Truran & Livio (1986)

The chapter is organised as follows: in Sect. 4.2, we estimate the WD mass distribution in novae in M31. The post-outburst models of novae are presented in Sect. 4.3, and in Sect. 4.4 we derive the luminosity function and T_{eff} distribution of the post-nova SSSs in M31 and compare our results with observations in Sect. 4.5. This is followed by a discussion of the uncertainties of our calculations and the magnitude of their effects on our results in Sect. 4.6. We finally summarize and conclude in Sect. 4.7.

4.2 WD mass distribution in novae in M31

One of the direct observables for a nova is its decline time, generally reported as the time to decline by 2 or 3 mag (t_2 or t_3 , respectively) from the observed visual peak. In the 1-D nova theory, this property of the nova is determined by the WD mass (M_{WD}), its core temperature (T_c) and the mass accretion rate (\dot{M}) (see Prialnik & Kovetz 1995 and references therein). In real novae, the light curve shape is further affected by possible asymmetry of the explosion and by the interaction of the nova ejecta with the accretion disk and the donor star. These will also introduce orientation-dependent effects, among other consequences. These complications are not included in the currently existing multicycle nova models, and therefore accurate visual decline times for theoretical models are not available. However, it has been shown that the mass-loss timescale t_{ml} computed in the Prialnik & Kovetz (1995) and Yaron et al. (2005) models approximates rather well the t_3 time in observed novae (Prialnik & Kovetz 1995). We will therefore use t_{ml} as a proxy to t_3 in our calculations. We can then use the nova simulation results, giving $t_3 \approx t_{\text{ml}}(M_{\text{WD}}, T_c, \dot{M})$, to approximately map the observed decline time distribution of novae to their WD mass distribution. To do this, we will also have to make some assumptions about their mass accretion rates and the WD core temperatures, as discussed below.

Based on the observed orbital period distribution of novae, Townsley & Bildsten (2005) found that majority of the novae accrete at rate $10^{-9} M_{\odot} \text{yr}^{-1}$ driven by magnetic braking. Further, Townsley & Bildsten (2004) studied the thermal effects of accretion on the WD

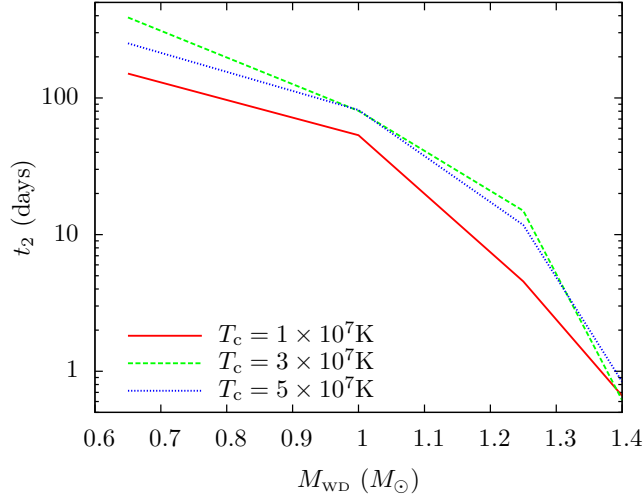


Figure 4.1: Theoretical decline time t_2 of novae as a function of the WD mass from Yaron et al. (2005) for mass accretion rate $\dot{M} = 10^{-9} M_{\odot} \text{ yr}^{-1}$ and different WD core temperatures as indicated in the legend.

undergoing nova outbursts and calculated self-consistently an equilibrium core temperature ($T_{c,\text{eq}}$) for the WD. This $T_{c,\text{eq}}$ is dictated mainly by the mass accretion rate and by the evolutionary timescale (also determined by \dot{M}); the latter characterising whether the WD core has reached the thermal equilibrium. For $\dot{M} = 10^{-9} M_{\odot} \text{ yr}^{-1}$, the WD core should be expected to nearly achieve the equilibrium temperature of $T_{c,\text{eq}} \approx 10^7$ K. The extended nova evolutionary tracks of Wolf et al. (2013) have been calculated for $\dot{M} = 10^{-9} M_{\odot} \text{ yr}^{-1}$ and $T_c = 3 \times 10^7$ K for all except the $1.36 M_{\odot}$ model where $T_c = 6 \times 10^7$ K was used, i.e., for a probably somewhat higher temperature than expected for the WD in this case. However, this difference is unimportant, as for the post-nova phase, the principal parameter is the envelope mass, and from Yaron et al. (2005) results for $\dot{M} = 10^{-9} M_{\odot} \text{ yr}^{-1}$ we see that the nova ignition masses in their Table 2 do not significantly depend on the core temperature in the considered range of temperatures.

In order to calculate the WD mass distribution in novae, we then obtain the decline time as a function of M_{WD} for $\dot{M} = 10^{-9} M_{\odot} \text{ yr}^{-1}$ from Yaron et al. (2005) by log-linearly interpolating their results between the grid values of the WD mass. For observed extragalactic novae t_2 is generally reported since it is easier to measure than t_3 . The t_2 time for the theoretical models from Yaron et al. (2005) is approximated by $t_{\text{ml}}/2.1$ for $t_{\text{ml}} < 50$ days and by $t_{\text{ml}}/1.75$ for $t_{\text{ml}} \geq 50$ days following Bode & Evans (2008). In Fig. 4.1, this decline time t_2 is shown as a function of M_{WD} for the three core temperatures Yaron et al. have used, i.e. 10^7 , 3×10^7 and 5×10^7 K. As is evident from the figure, the decline times of the novae for $T_c = 3 \times 10^7$ and 5×10^7 K agree within a factor of $\lesssim 2$. We will therefore only derive the WD mass distribution for two values of the temperature $T_c = 10^7$ and 3×10^7 K. As mentioned above, the post-nova evolution should not depend strongly on the core temperature, hence we use the same post-nova models for both T_c 's in our calculations. For the rest of the chapter we adopt the mass accretion rate of the novae to be $10^{-9} M_{\odot} \text{ yr}^{-1}$.

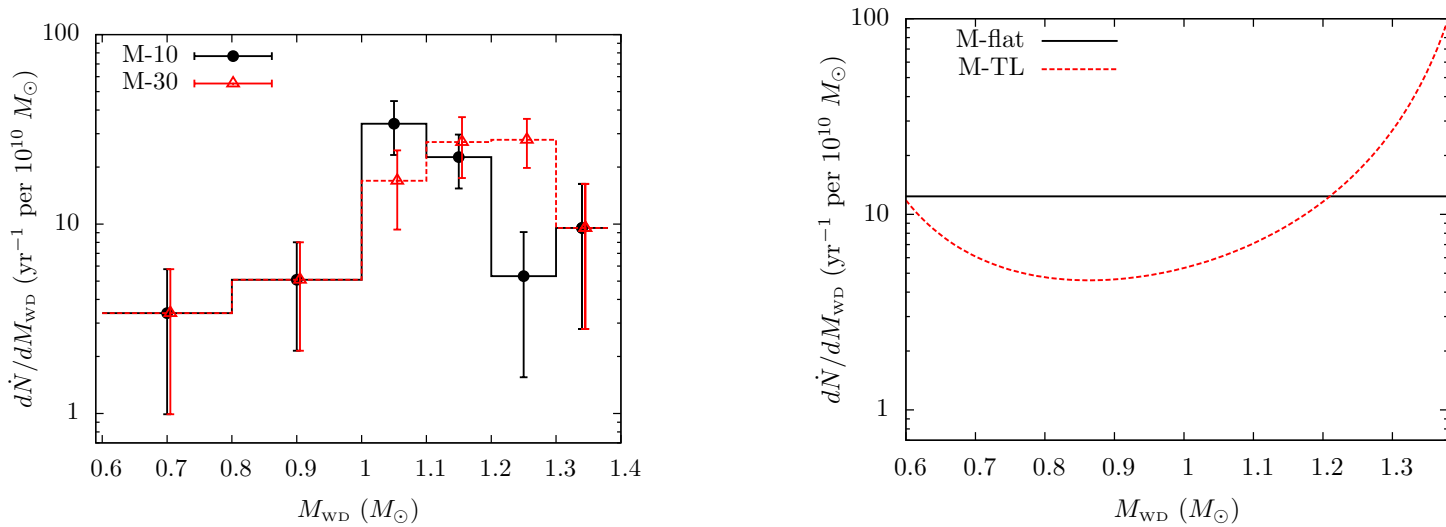


Figure 4.2: *Left panel:* The inferred WD mass distribution in novae in M31 normalized to $10^{10} M_{\odot}$, using the nova samples of Arp (1956) and Darnley et al. (2004) (cf. Sects. 3.3 and 3.4). The WD masses of the novae are derived based on their observed decline times (Fig. 3.2) using the results from Yaron et al. (2005) (see text for details). The corresponding mass distribution for WD $T_c = 10^7$ K (model M-10 in Table 4.1) is shown here in black, and that for $T_c = 3 \times 10^7$ K (model M-30) in red. The error bars have been derived via error propagation, assuming Poissonian error for the detected number of novae. *Right panel:* Assumed theoretical WD mass distributions in novae per $10^{10} M_{\odot}$ in M31. The black line shows the uniform distribution (model M-flat in Table 4.1) and the red dotted line represents the distribution from Truran & Livio (1986) (model M-TL).

We now use the observed t_2 distribution of the nova rate in M31 corrected for incompleteness (Fig. 3.2), which is described in the Sects. 3.3 and 3.4, with the results from Yaron et al. (2005) (Fig. 4.1) to deduce the corresponding WD mass distribution in novae. The result is shown in Fig. 4.2 (left panel). As one can see from the plot, the two mass distributions are qualitatively similar, except that for the higher WD temperature, its peak is shifted towards higher WD masses by about one mass bin.

In addition, we also explore two simple forms of WD mass distribution in novae, which are independent of the nova models from Yaron et al. (2005). Specifically, we consider the distribution from Truran & Livio (1986) as well as an ad hoc flat mass distribution. To derive the former, Truran & Livio (1986) assumed the Salpeter (1955) mass function for the WD progenitors and used the main-sequence mass – WD mass relation for single stars to obtain the distribution of WD masses. Furthermore, they assumed that the nova recurrence frequency ν is a function of only the WD mass, and using a simplified treatment of the nova explosion mechanism derived the $\nu = f(M_{\text{WD}})$. Finally, they determined the WD mass distribution in novae as a product of $\nu = f(M_{\text{WD}})$ and the WD mass function. Although this model is obviously oversimplified, it is not affected by the complexities of the multicycle nova evolution models and by the subtleties of the incompleteness correction of observed distributions. For this reason we used it, along with an ad hoc flat distribution, to investigate the dependence of our results on the assumed WD mass distribution.

We normalise both the flat mass distribution and that of Truran & Livio (1986) to the total nova rate in M31 of 106 yr^{-1} , same as our experimentally derived mass distribution (cf. Sect. 3.4). They are shown in Fig. 4.2 (right panel) and their properties are summarised in Table 4.1.

4.3 Post-outburst SSS phase of Novae

To explore the post-nova SSS phase, we use the nova evolutionary tracks from Wolf et al. (2013) recomputed on an extended grid of WD masses. These tracks were computed with MESA (Paxton et al. 2011, 2013) for WD masses 0.6, 0.7, 0.8, 0.9, 1.00, 1.05, 1.10, 1.15, 1.20, 1.25, 1.30, 1.32, 1.34 and $1.36 M_{\odot}$ with SEW mass-loss prescription. We will discuss our choice of the mass-loss prescription towards the end of this section. Using these tracks, we derive the evolution of the nova in the soft X-ray band 0.2–1.0 keV – the energy range used by Henze et al. (2010, 2011, 2014b) in their analysis of *XMM-Newton* data of X-ray monitoring of novae in M31. In computing the soft X-ray light curves of the post-nova SSSs we assume a blackbody emission spectrum. The impact of this assumption on our conclusions is further discussed in Sect. 4.6. The photospheric radius and bolometric luminosity are self-consistently computed at each time step of the nova tracks, from which the effective temperature is calculated using the Stefan-Boltzmann law (see Wolf et al. 2013 for details). With these quantities given, the 0.2–1.0 keV band luminosity can be straightforwardly computed for the assumed blackbody spectral energy distribution. Typical fractions of the bolometric luminosity emitted in the 0.2–1.0 keV band range from 0.03 for the lowest WD mass to 0.85 for the most massive WDs, i.e.,

under these assumptions, the bolometric correction for the X-ray band drops to nearly unity as the WD mass approaches the Chandrasekhar mass limit.

The (unabsorbed) soft X-ray light curves are shown in Fig. 4.3 (left), after aligning them with respect to the outburst time. Also shown in the right panel are the peak luminosities of these light curves, both unabsorbed as well as the absorbed ones. The latter is obtained by computing the light curves taking into account the Galactic foreground absorption, by assuming a hydrogen column density $N_{\text{H}} \approx 6.7 \times 10^{20} \text{ cm}^{-2}$ towards M31 (Stark et al. 1992) and using the Tuebingen-Boulder absorption model (Wilms et al. 2000). There is also a SSS phase during the TNR itself, but it lasts at most ~ 1 day for the luminosity range shown in Fig. 4.3, and is not plotted there. However, in our calculations we use the complete light curve. Shown in Fig. 4.4 is the corresponding evolution of the effective temperature T_{eff} .

Since the post-nova SSS phase results from the stable burning of the remnant hydrogen on the WD surface, we expect from nova theory (e.g., Prialnik & Kovetz 1995; Yaron et al. 2005) that more massive WDs, which require smaller ignition mass, will have a shorter SSS phase duration. This is evident in the light curves shown in Fig. 4.3. Also, since this phase of the nova is phenomenologically similar to the post-AGB phase of stellar evolution (see Sala & Hernanz 2005b and references therein), we expect from the core mass-luminosity relation the more massive WDs with their higher surface gravity to have higher luminosity and accordingly higher effective temperature than the less massive ones. This is demonstrated in the right panels of Figs. 4.3 and 4.4.

As mentioned earlier, we use the post-nova evolutionary models from Wolf et al. (2013), which employ the SEW mass-loss mechanism. It is known that the mass-loss process in novae is still not well understood. In fact, for novae with short recurrence period occurring on massive WDs, the dominant uncertainty in their modeling is probably the mass-loss prescription as compared to other uncertainties, such as mixing (see Sect. 4.6). In nova models, besides the SEW and RLOF mass-loss prescriptions (Sect. 4.1) used by Wolf et al. (2013), there are other prescriptions used by different groups that may or may not be more valid, such as the optically thick wind used by Kato & Hachisu (1994) or the hydrodynamic outburst followed by wind implemented by Prialnik & Kovetz (1995) and Yaron et al. (2005). The main effect of these different wind prescriptions on the post-nova SSS phase is that, for the same amount of ejected material, the faster winds will make the ejecta optically thin faster, revealing the SSS earlier. Alternatively, for the same mass-loss duration, some prescriptions will eject more material than the others, such as in the case of SEW versus RLOF (Wolf et al. 2013).

From the power law fits of Wolf et al. (2013) to the dependence of the turn-off time of post-nova SSS phase on the WD mass, the duration of this phase for the RLOF models is ~ 4 times that of the SEW models. This could have a significant impact on the results of our calculations. However, according to Wolf et al. (2013), the SEW models are more appropriate for novae occurring on massive WDs while the RLOF models are suitable for less massive ones. Given the typical sensitivity of the current X-ray observations, including those used for comparison later in this chapter, we should expect to observe mainly the bright post-nova SSSs, occurring on sufficiently massive WDs, $\gtrsim 1 M_{\odot}$ (Fig. 4.3).

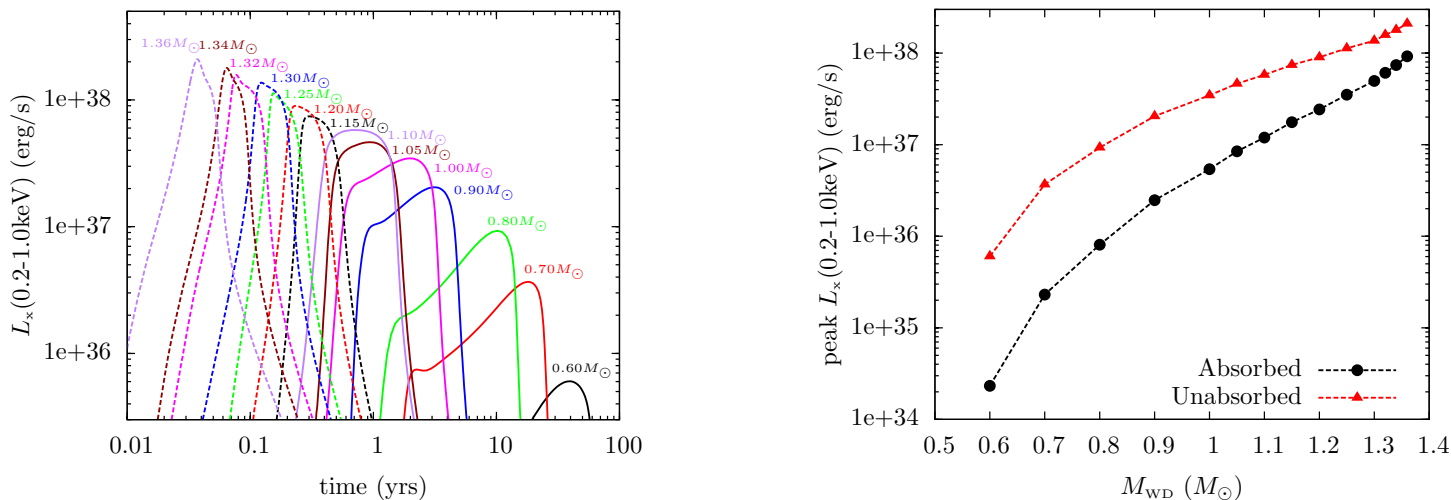


Figure 4.3: *Left panel:* Evolution of the post-nova (unabsorbed) soft X-ray luminosity in the 0.2-1.0 keV band for different WD masses, as indicated against the corresponding curve. These light curves have been aligned with respect to the outburst time. *Right panel:* Peak soft X-ray luminosity from the light curves in the left panel as a function of the WD mass. The black circles represent these luminosities with Galactic foreground absorption towards M31 ($N_{\text{H}} \approx 6.7 \times 10^{20} \text{ cm}^{-2}$) and the corresponding unabsorbed luminosities are shown as red triangles.

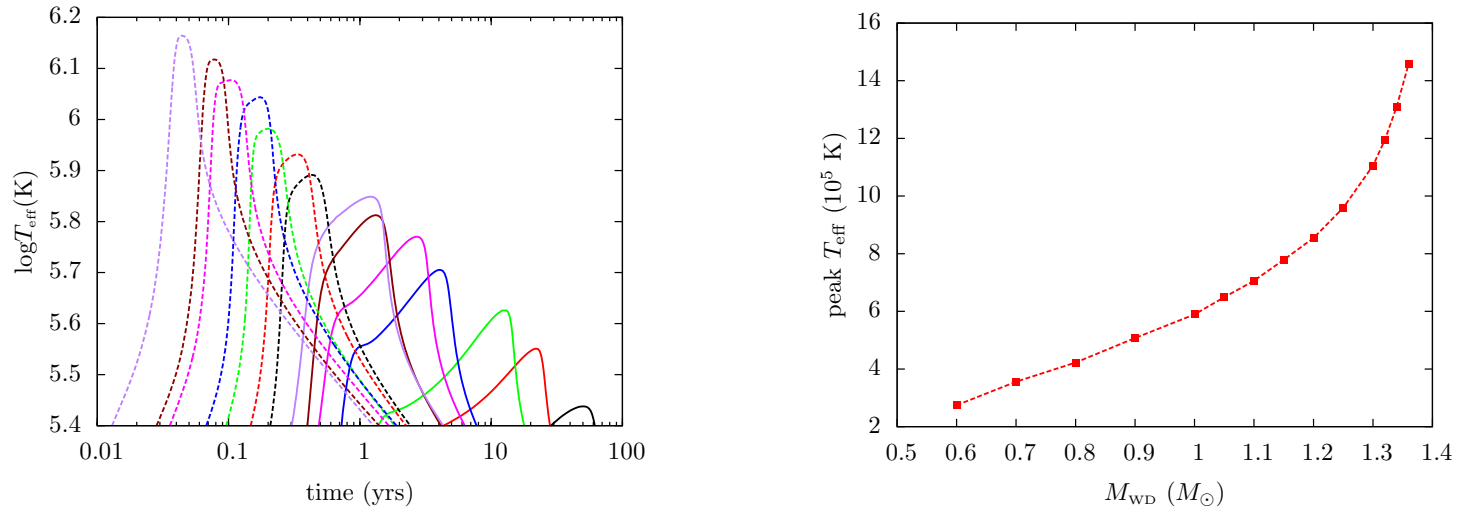


Figure 4.4: *Left panel:* Evolution of the effective temperature (T_{eff}) of post-nova SSSs from the nova evolutionary tracks of Wolf et al. (2013) computed using the Stefan-Boltzmann law (see Wolf et al. (2013) for details). The colour coding is the same as in Fig. 4.3. These T_{eff} curves have also been aligned with respect to the outburst time. *Right panel:* Peak effective temperature as a function of the WD mass.

Table 4.2: Theoretical nova rate for the different WD mass distribution models. Masses are in solar units and for each model, rates are given per year in the given WD mass interval range.

mass range	mid-mass	M-10	M-30	M-flat	M-TL
0.650 - 0.750	0.70	3.72	3.72	13.59	6.85
0.750 - 0.850	0.80	4.66	4.66	13.59	5.30
0.850 - 0.950	0.90	5.59	5.59	13.59	5.15
0.950 - 1.025	1.00	12.10	7.45	10.19	4.30
1.025 - 1.075	1.05	18.62	9.31	6.79	3.32
1.075 - 1.125	1.10	15.51	12.10	6.79	3.92
1.125 - 1.175	1.15	12.40	14.90	6.79	4.87
1.175 - 1.225	1.20	7.66	15.11	6.79	6.43
1.225 - 1.275	1.25	2.92	15.32	6.79	9.24
1.275 - 1.310	1.30	2.51	8.71	4.76	9.62
1.310 - 1.330	1.32	2.10	2.10	2.72	7.59
1.330 - 1.350	1.34	2.10	2.10	2.72	10.12
1.350 - 1.370	1.36	2.10	2.10	2.72	14.33

Therefore, between SEW and RLOF models, the use of those with SEW mass-loss prescription is justified.

4.4 Post-nova SSS population in M31

With the WD mass distribution in novae in M31 (Sect. 4.2) and the post-nova models (Sect. 4.3), we can compute the post-nova SSS population. Their luminosity function is given by

$$\frac{dN(L_x)}{dL_x} = \int_{M_{\text{low}}}^{M_{\text{ch}}} \frac{d\dot{N}(M_{\text{WD}})}{dM_{\text{WD}}} \phi(L_x, M_{\text{WD}}) dM_{\text{WD}}, \quad (4.1)$$

where M_{ch} is the Chandrasekhar mass, M_{low} is the lower limit of the WD mass. The first term inside the integral on the right hand side is the WD mass distribution in novae and the function $\phi(L_x, M_{\text{WD}})$ depends on the shape of the light curve as follows:

$$\begin{aligned} \phi(L_x, M_{\text{WD}}) &= \left(\frac{dL_x}{dt} \right)_{\text{rise}}^{-1} + \left(\frac{dL_x}{dt} \right)_{\text{decay}}^{-1}, & L_x < L_p \\ &= 0, & L_x \geq L_p \end{aligned}$$

where $L_x = L_x(t, M_{\text{WD}})$ is the (post-nova) soft X-ray light curve for the WD of mass M_{WD} and $L_p = L_p(M_{\text{WD}})$ is its peak luminosity. The derivatives are taken in the rising and declining parts of the light curve at the points in time when the luminosity equals L_x .

As can be seen from Fig. 4.3 (right panel), the peak (absorbed) soft X-ray luminosity L_x for WD masses below $\sim 0.65 M_\odot$ is less than 10^{35} erg/s, which is below the sensitivity limit for observation of M31 by the current X-ray satellites like *Chandra* and *XMM-Newton*. For our calculations we are interested in the bright sources, observable with these X-ray missions. We therefore set $M_{\text{low}} = 0.65$ in Eq. (4.1) and solve it using a Monte Carlo method. To this end, we divide the WD mass range $0.65 - 1.37 M_\odot$ into 13 bins and use the WD mass distribution derived in Sect. 4.2 to obtain the nova rate in each bin as given in Table 4.2. For each mass bin, we then seed novae randomly in time according to their corresponding rates and follow their luminosity (Fig. 4.3) and effective temperature evolution (Fig. 4.4). To minimise the Monte Carlo errors, we perform the simulations for a period of 5×10^4 yrs, taking 1000 snapshots separated by 50 yrs, a long enough interval for (absorbed) luminosity greater than 10^{35} erg/s to ensure that any post-nova SSS is captured in only one snapshot. In each snapshot, we register the number of SSSs with their luminosities and temperatures. Averaging over the snapshots, we calculate the instantaneous number of post-nova SSSs in M31 as a function of (unabsorbed) luminosity and T_{eff} . The results are discussed in the next two sections.

4.4.1 Luminosity function

The luminosity functions (LFs) of post-nova SSSs obtained under different assumptions about the WD mass distribution are shown in Fig. 4.5. The luminosity bin width is determined by the WD mass sampling of the post-nova evolutionary tracks (cf. Fig. 4.3). We used coarser bins for low luminosities where the tracks are sparser and finer bins for high luminosities where the tracks sample the WD mass with smaller step. Note that the functions are plotted against the unabsorbed luminosity, computed for the 0.2 – 1.0 keV band. The effects of interstellar absorption in M31 will be considered in Sect. 4.5.

As can be seen from Fig. 4.5, the LFs in all four cases have a cut-off at $L_x \approx 2 \times 10^{38}$ erg/s, which corresponds to the maximum unabsorbed soft X-ray luminosity achieved by the post-nova X-ray sources containing the most massive WDs (see Fig. 4.3 right). Accounting for bolometric correction, this cut-off luminosity exceeds marginally the Eddington limit for the most massive WDs ($1.36 M_\odot$) in the grid of post-nova models of Wolf et al. (2013) used in our calculations. The occurrence of luminosity L_x close to the Eddington limit in our results can be understood as follows. The post-nova models of Wolf et al. (2013) used in our calculations do not avoid super Eddington luminosities. In fact, as discussed in Sect. 4.3, the mass loss during the nova outburst is regulated by a wind triggered by the luminosity in excess of the Eddington limit (see Wolf et al. 2013 and Denissenkov et al. 2013 for details). This in turn acts to reduce the nuclear burning, which is driven by the pressure of the envelope acting at the base of the hydrogen layer, causing the luminosity to become sub-Eddington sooner than it would have in the absence of the wind. However, since the most massive WDs become transparent to soft X-rays sooner than the lower mass WDs (see Fig. 4.3 left), the occurrence of super Eddington luminosity during the post-nova SSS phase is possible for the former WDs. Also, as discussed in Sect. 4.3, the bolometric correction for the soft X-ray luminosity of the massive WDs is smaller than

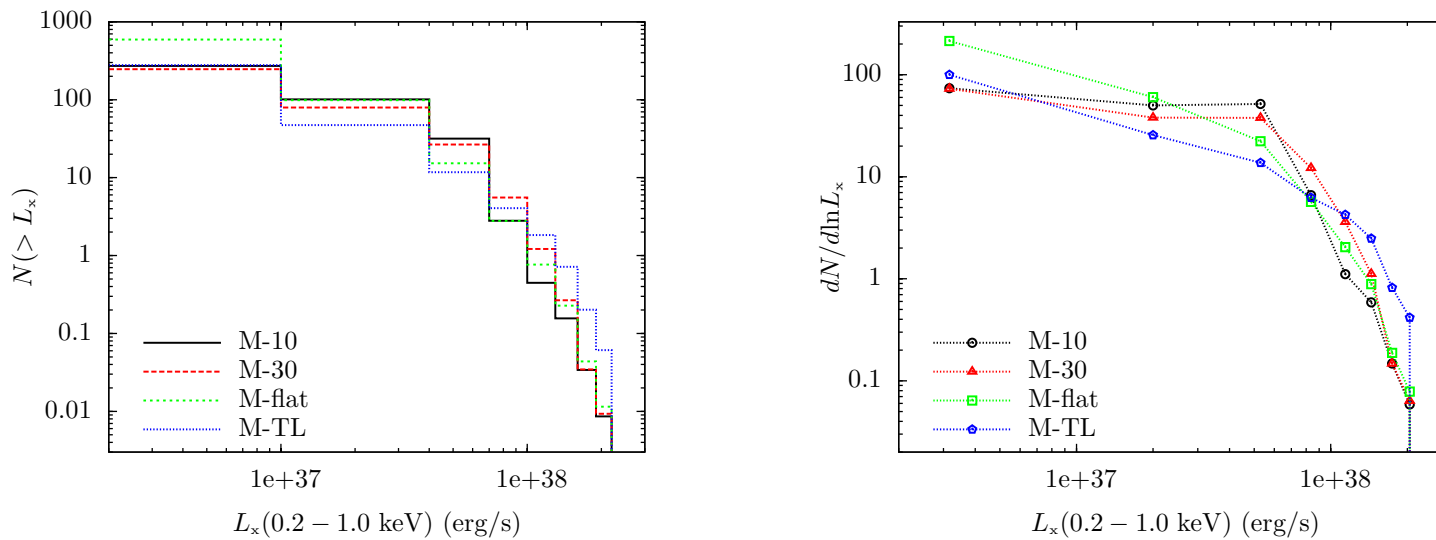


Figure 4.5: Cumulative (*left*) and differential (*right*) luminosity functions of the post-nova SSSs in M31 for the different WD mass distribution models. Note that the luminosity, L_x , shown in both plots is the unabsorbed luminosity. These functions are normalized to the total stellar mass of M31, which is $\approx 1.1 \times 10^{11} M_\odot$. The Monte Carlo errors are negligibly small and are not plotted.

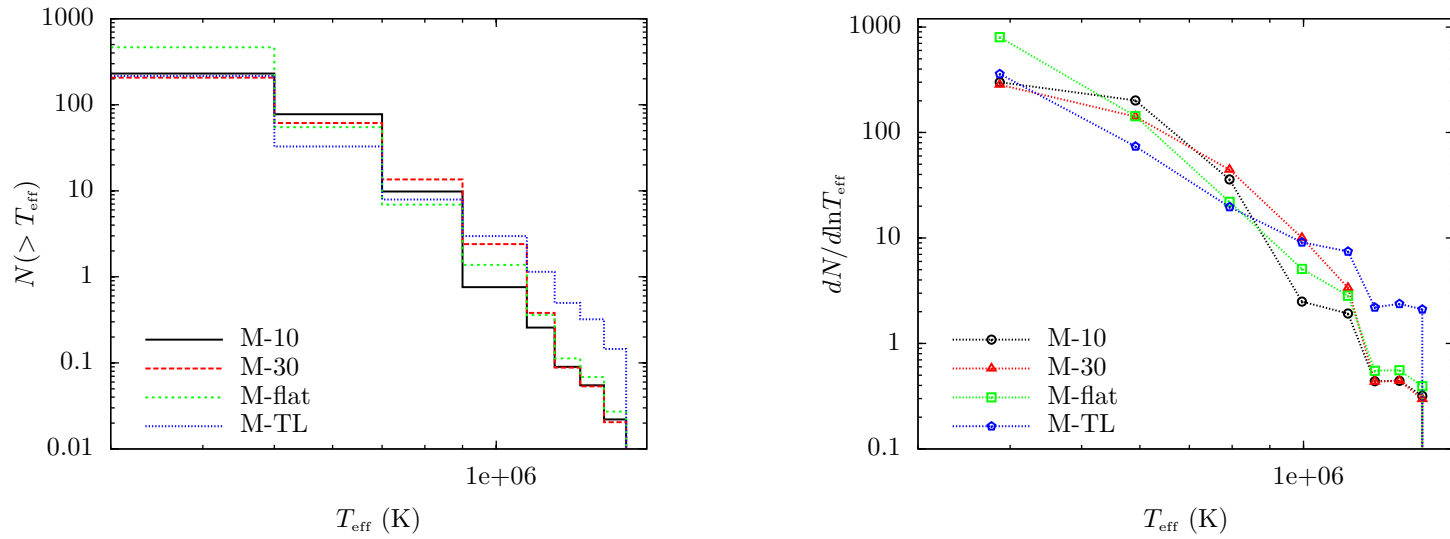


Figure 4.6: Cumulative effective temperature (T_{eff}) distribution of post-nova SSSs in M31 with unabsorbed luminosity $L_x \gtrsim 10^{36}$ erg/s (*left*) and the corresponding differential distribution (*right*). These distributions are normalized to the total stellar mass of M31, $1.1 \times 10^{11} M_{\odot}$.

that of the lower mass WDs. Therefore, the maximum L_x during the SSS phase for the post-nova models of massive WDs tend to be close to their Eddington limit (cf. Fig. 4.3 right).

From the cumulative luminosity function (Fig. 4.5 left), we compute the number of post-nova SSSs with (unabsorbed) $L_x \gtrsim 10^{36}$ erg/s at any given time in M31 for the various WD mass distribution models. These numbers, denoted as $n(L_x \gtrsim 10^{36}$ erg/s), are given in Table 4.3. We determine the contribution of bright sources to the computed values of $n(L_x \gtrsim 10^{36}$ erg/s) for the different mass distribution models. For model M-10, we find 7% of these sources have $L_x \gtrsim 5 \times 10^{37}$ erg/s and 37% have $L_x \gtrsim 10^{37}$ erg/s. The corresponding fractions for model M-30 are 7% and 32%, for model M-flat they are 2% and 17% and for model M-TL they are 3% and 17%. Finally, using the differential LFs, shown in Fig. 4.5 (right panel), we compute, for each WD mass distribution model, the combined unabsorbed luminosity of sources with $L_x \gtrsim 10^{36}$ erg/s. These results are also listed in Table 4.3.

From Eq. (4.1) it is clear that the general shape of the differential LFs is determined by low mass and high mass WDs at the low and high luminosity ends, respectively (cf. Fig. 4.3, right panel). The steep decline at the high luminosity end for the differential LFs is due to the short SSS duration for the massive WDs with higher peak luminosities, whereas the relatively gradual slope towards low luminosities is due to the longer SSS duration for the less massive WDs with lower peak luminosities. The models M-flat and M-TL have larger number of faint sources ($L_x \lesssim 10^{37}$ erg/s) than models M-10 and M-30, since the WD mass distributions for M-flat and M-TL have greater values than M-10 and M-30 at WD masses $\lesssim 0.8 - 1.0 M_\odot$ (cf. Fig. 4.2). On the other hand, for L_x in the range $\sim 10^{37} - 10^{38}$ erg/s, models M-10 and M-30 have larger number of sources (see above) as the WD mass distributions for these models attain their maximum at the WD mass values, $\sim 1.0 - 1.2 M_\odot$, having peak luminosities in $10^{37} - 10^{38}$ erg/s range (Figs. 4.2 and 4.3). Finally, beyond $1.3 M_\odot$, model M-TL has the largest values for the WD mass distribution (Fig. 4.2) and accordingly it has the largest number of sources above $\sim 10^{38}$ erg/s, where WDs with mass greater than $1.3 M_\odot$ have their peak luminosities, as observed for the recurrent nova M31N 2008-12a.

Given the remarkable nature of this M31 nova M31N 2008-12a, which apparently is “on” in soft X-rays for about two weeks every year (e.g., see Henze et al. 2014a; Tang et al. 2014c; Henze et al. 2015), we have used its X-ray observation results to obtain the range of its (blackbody) effective temperature and corresponding luminosity during its SSS phase. For the T_{eff} range $1 - 1.3 \times 10^6$ K and corresponding photospheric radius from Tang et al. (2014c), we find its (unabsorbed) luminosity in the 0.2–1.0 keV band to be in the range $1.0 - 3.0 \times 10^{38}$ erg/s during its “on” state (see also Henze et al. 2015). From the observed duration of its SSS phase, we infer the number of this system visible at any instant in M31 to be ≈ 0.04 with $L_x \gtrsim 10^{38}$ erg/s and $T_{\text{eff}} \gtrsim 10^6$ K.

Note that the LFs (Fig. 4.5) and T_{eff} distributions (see below; Fig. 4.6) are the predicted results for the whole M31 galaxy, not subjected to the selection biases of any survey. Further, besides M31N 2008-12a, there will also exist some number of novae in M31 hosting massive WDs, even if their recurrence time is not as short as one year of M31N 2008-12a

(cf. Fig. 4.2). As discussed above, these post-nova SSSs with massive WDs will have high luminosity as well as high T_{eff} (Sect. 4.4.2). The observation results from this single nova M31N 2008-12a then give a lower limit on the cumulative LF of the post-nova SSSs in M31 at $L_x \approx 10^{38}$ erg/s (Fig. 4.5 left) and also on their cumulative T_{eff} distribution at $T_{\text{eff}} \approx 10^6$ K (Fig. 4.6 left). To justify this further, in Henze et al. (2010), for example, one can find other post-nova SSSs in M31 observed with *XMM-Newton*, whose L_x (0.2–1.0 keV) obtained from blackbody spectral fitting is $\gtrsim 10^{38}$ erg/s.

4.4.2 Effective temperature distribution

We also determine the effective temperature distribution of the post-nova SSSs, whose LFs were obtained in the previous section. The resulting cumulative and differential T_{eff} distributions for sources with (unabsorbed) $L_x \gtrsim 10^{36}$ erg/s are shown in Fig. 4.6.

The analytical expression for the differential T_{eff} distribution is similar to that of the differential luminosity function given by Eq. (4.1), but with $\phi(L_x, M_{\text{WD}})$ replaced with $\psi(T_{\text{eff}}, M_{\text{WD}})$ defined as

$$\begin{aligned} \psi(T_{\text{eff}}, M_{\text{WD}}) &= \left(\frac{dT_{\text{eff}}}{dt} \right)_{\text{rise}}^{-1} + \left(\frac{dT_{\text{eff}}}{dt} \right)_{\text{decay}}^{-1} && , T_{\text{eff}} < T_p \\ &= 0 && , T_{\text{eff}} \geq T_p \end{aligned}$$

where $T_p = T_p(M_{\text{WD}})$ is the peak value of the temperature curve $T_{\text{eff}} = T_{\text{eff}}(t, M_{\text{WD}})$ for the corresponding WD mass M_{WD} .

As can be seen from Fig. 4.6 (right), the differential T_{eff} distributions for all the four WD mass distribution models have a cut-off at $T_{\text{eff}} \sim 1.5 \times 10^6$ K. This cut-off value corresponds to the highest T_{eff} obtained from the evolutionary tracks (Fig. 4.4 right). Further, in close analogy with the LFs, at low T_{eff} values the differential distribution is determined by low mass WDs while at the high T_{eff} end, it is determined by the massive WDs (cf. Fig. 4.4 right). The short timescale of the T_{eff} evolution for massive WDs (see Fig. 4.4) leads to smaller SSS numbers in the differential T_{eff} distribution at high T_{eff} end, while the longer duration for the less massive ones leads to higher SSS numbers at low T_{eff} values.

Finally, in Fig. 4.7, we plot the distribution of the post-nova SSSs on the effective temperature – luminosity plane. Fig. 4.7 shows this distribution for the M-10 model; for other WD mass functions this distribution looks qualitatively similar. As could be expected, the left bottom corner of the $T_{\text{eff}} - L_x$ parameter space, i.e., low luminosity and low effective temperature, is relatively more populated.

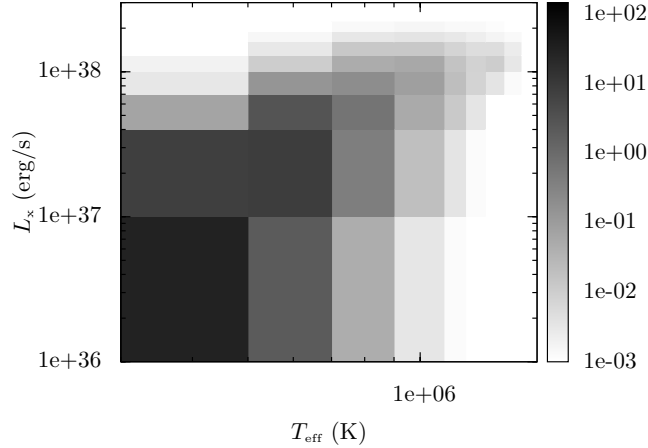


Figure 4.7: Effective temperature–luminosity plot for the post-nova SSSs in M31 corresponding to the model M-10. The respective plot for the other three models (M-30, M-flat and M-TL) look qualitatively similar. The gray scale indicates the absolute number of SSSs per bin. Note that L_x is the integrated unabsorbed luminosity in the 0.2–1.0 keV band.

Table 4.3: Monte Carlo simulation results for the different models of WD mass distribution in novae in M31

Model	n^a	L_{total} (erg/s) ^b	$N_{XMM-Newton}^c$	ΔN_{H} (10^{21}cm^{-2}) ^d
M-10	271	3.97×10^{39}	65–74	1.70–2.35
M-30	247	3.44×10^{39}	57–65	2.05–2.75
M-flat	592	4.67×10^{39}	48–63	1.25–1.85
M-TL	277	2.51×10^{39}	33–40	1.45–2.05

^aNumber of post-nova SSSs with unabsorbed $L_x \gtrsim 10^{36}$ erg/s at any instant in M31.

^bTotal luminosity from the $n(L_x \gtrsim 10^{36}$ erg/s) post-nova SSSs.

^cNumber of post-nova SSSs predicted for the *XMM-Newton* observations from Henze et al. (2010, 2011). The first value corresponds to the threshold (unabsorbed) luminosity $L_x = 5 \times 10^{36}$ erg/s and the second value to $L_x = 3 \times 10^{36}$ erg/s (cf. Sect. 4.5).

^dNeutral hydrogen column density of the circumstellar material required to reduce the predicted number of sources for the *XMM-Newton* observations to 16 that were observed (cf. Sects. 4.5 and 4.6). The first value is for threshold (unabsorbed) luminosity $L_x = 5 \times 10^{36}$ erg/s and the second value for $L_x = 3 \times 10^{36}$ erg/s.

4.5 Comparison with *XMM-Newton* observations of M31

Our knowledge of the statistics of novae detected in the post-outburst SSS phase has improved significantly in the past years, especially thanks to extended *XMM-Newton* monitoring campaign of M31. We therefore take this opportunity to compare our theoretical predictions with observational results. In particular, we use the results of Henze et al. (2010, 2011) based on *XMM-Newton* observations of the central region of M31. This monitoring program comprised three campaigns – June 2006 to March 2007, November 2007 to February 2008 and November 2008 to February 2009. In total there were 15 observations, all pointed at the center of M31, with typical exposure time of around 10-20 ksec each. Details of these observations are given in Henze et al. (2010, 2011).

In order to account for the limited spatial coverage of M31 in these observations, we normalize the nova rate in our simulations to the mass contained within the FOV of *XMM-Newton*. To determine this mass we use the Spitzer 3.6 micron image of M31 from Barmby et al. (2006) and approximate the *XMM-Newton* FOV by a circular region centered at the nucleus of M31 with a diameter of 30'. We then compute the stellar mass enclosed in the same manner as in Sect. 3.4. These M31 *XMM-Newton* observations suffer from source confusion in the innermost region (Henze et al. 2010, 2011, 2014b). Following Henze et al. (2014b), we subtract from the calculated total stellar mass within the FOV, the stellar mass enclosed in a rectangular region of dimensions 3.3' \times 3.3' centered at the nucleus of M31. We thus obtain a value of $\approx 3 \times 10^{10} M_{\odot}$, which is used to normalize the nova rate.

We repeated the Monte Carlo simulations described in Sect. 4.4 with the WD mass distribution renormalised according to the nova rate within the *XMM-Newton* FOV. However, now we placed the snapshots in time according to the pattern of *XMM-Newton* observations. We obtain a catalog of the sources appearing in these snapshots, registering their luminosities and effective temperatures. We then filter this catalog using the detection sensitivity of *XMM-Newton* (see below) to obtain the actual number of sources “detected” in these simulations. To minimise the Monte Carlo errors, we repeated the simulations multiple number of times.

According to Henze et al. (2011), the detection sensitivity of *XMM-Newton* in a typical individual observation from the M31 monitoring program is around a few times 10^{36} erg/s in the 0.2-1.0 keV band. We therefore ran two sets of simulations with the sensitivity limit of 3×10^{36} and 5×10^{36} erg/s. The quoted limiting luminosity from Henze et al. (2011) is the unabsorbed luminosity of the source derived assuming a 50 eV blackbody spectrum and Galactic foreground absorption. We used PIMMS¹ to recompute it for the given value of the effective temperature (different for different sources “detected” in our simulations) and for the hydrogen column density N_{H} taking into account the spatially varying intrinsic absorption in M31.

To incorporate the latter, we use the HI map from Brinks & Shane (1984) (see also Nietten et al. 2006). We construct a grid over the *XMM-Newton* FOV with cell size 2' \times 2'

¹<http://heasarc.gsfc.nasa.gov/docs/software/tools/pimms.html>

and use the HI map to calculate the total N_{H} in each cell, including the Galactic foreground value of $6.7 \times 10^{20} \text{ cm}^{-2}$. In each grid cell, for each source temperature from the above catalog of simulated sources we determine the detection threshold and thereby compute the total number of sources, whose luminosity exceeds the detection threshold. As the source catalog was derived for the entire *XMM-Newton* FOV, the number of sources in the given grid cell is scaled down according to the stellar mass contained in the cell. This procedure is carried out for all the cells and the results are summed up to calculate the total number of “detected” sources. The results of these calculations for various WD mass distribution models are summarised in Table 4.3, from which we can see that according to our calculations, about $\approx 30 - 80$ post-nova SSSs should be detected in the *XMM-Newton* monitoring campaign.

Henze et al. (2010, 2011) found 16 SSSs in total from these observations, located within the FOV we have considered, 13 of which have been identified with previously registered optical novae. Given the incompleteness of the optical nova surveys, it is not unlikely that the remaining 3 SSSs are also associated with novae. From Table 4.3, we thus see that our predictions agree with *XMM-Newton* observations within a factor of $\approx 2 - 5$. These results are discussed further in the following section.

4.6 Discussion

Given the number and magnitude of uncertainties involved in modeling the post-nova supersoft X-ray phase, the factor of $\approx 2 - 5$ disagreement between the predicted number of post-nova SSSs and the result of *XMM-Newton* observations is remarkably modest. Moreover, it is comparable to the spread (about a factor of ~ 2) between the results obtained for different models of the WD mass distribution in novae. Below we discuss how these results depend on various uncertainties and assumptions involved in our calculations.

The main simplification of the calculations presented in this chapter is the assumption of blackbody spectrum for the post-nova SSSs. This assumption is commonly made in SSS studies; it is motivated, at least partly, by the fact that the observed spectral energy distribution (SED) of the continuum emission in SSSs can be often represented by the simple blackbody spectrum (e.g, Skopal 2015). However, it is obvious that spectral formation in SSSs is much more complex. Indeed, a number of emission and absorption lines and absorption edges are observed in the spectra taken with better sensitivity and energy resolution, with some evidence that orientation effects may play a significant role (Ness et al. 2013). Currently, no theoretical model can describe the entire complexity of SSS spectra. However, the existing static NLTE WD atmosphere calculations may serve as a useful first approximation to gauge the magnitude of the effect on our results from using more realistic spectral models. To this end, we used the publicly available TMAP models (Rauch & Werner 2010) provided by the TheoSSA service (<http://dc.g-vo.org/theossa>). For the range of interesting WD masses ($0.90-1.25 M_{\odot}$) and their peak effective temperatures ($5 \times 10^5 - 10^6 \text{ K}$), we compare the 0.2–1.0 keV luminosity of a blackbody spectrum with that from the NLTE models with the same effective temperature. We find

the NLTE (unabsorbed) luminosities to be lower than the blackbody ones typically by a factor of ~ 2 . Because of the rather flat shape of the luminosity distribution of the post-nova SSSs (Fig. 4.5) in the luminosity range of interest, $\log(L_x) \sim 36 - 37$, this does not have a significant effect on the total number of sources. From Fig. 4.5, we estimate that this will decrease the predicted number of post-nova SSSs in Table 4.3 by a factor of ≈ 1.3 . Comparing the *absorbed* blackbody and NLTE luminosities, computed using a total N_H of $2 \times 10^{21} \text{ cm}^{-2}$ from the Galactic foreground ($6.7 \times 10^{20} \text{ cm}^{-2}$) and the interstellar medium in M31 (typically $\sim 10^{21} \text{ cm}^{-2}$), we now find a factor of 1.2 – 1.7 difference between the two for the above WD parameters. We therefore conclude that the use of NLTE models will reduce the discrepancy between our predictions and the *XMM-Newton* observations.

It should be noted however that the stationary TMAP NLTE models do not quite reproduce the entire complexity of the observed SSS spectra, in particular the significant orientation effects and the blue shifts of absorption lines seen in X-ray grating spectra of Galactic post-nova SSSs (Ness 2010; Ness et al. 2013). The blue shifts indicate the presence of an expanding nova shell (van Rossum & Ness 2010), which is not accounted for in TMAP models as they assume plane parallel geometry and hydrostatic equilibrium. This restriction has been lifted in the wind model of van Rossum & Ness (2010) and van Rossum (2012). The latter used the wind models to fit the observed grating spectra of nova V4743 Sgr 2003 during its SSS phase. They obtained a slightly different T_{eff} than Rauch et al. (2010) based on TMAP model. Direct application of the wind models of van Rossum (2012) to our calculations is not straightforward however, as the parameters required for the wind models, specifically the expansion velocity and mass outflow rate, necessitate their consistent integration with the post-nova modeling, which is beyond the scope of this work. This will be pursued in future as a follow-up to this work. On the other hand, the results of Skopal (2015) suggest that the spectral energy distribution of many SSSs is nevertheless broadly consistent with the blackbody spectrum, i.e., the above mentioned effects should not affect the bolometric correction significantly, especially for the higher mass WDs.

Regarding the uncertainties in modeling the post-nova SSSs, there are two main elements relevant to our calculations. Firstly, it is the issue of mixing between the accreted matter with the WD core, the mechanism of which is still largely an unresolved issue in nova theory. Mixing is not accounted for in the MESA models of Wolf et al. (2013) that we have used, and therefore our results are insensitive to the WD core composition. Nevertheless, as evident from the analysis of the ejecta composition of observed novae, some level of mixing between the core and the envelope should occur in novae. The resulting metal enrichment in the nuclear burning shell enhances the burning rate of hydrogen during the CNO cycle, in turn increasing the burning temperature and also the kinetic energy of the ejecta (e.g., Starrfield et al. 1972; Glasner et al. 2012). This produces a more violent nova eruption, reducing the remnant hydrogen mass that powers the SSS phase. The effect of mixing on the post-nova SSS phase is thus to shorten its duration. For example, Sala & Hernanz (2005b) have computed using hydrostatic nova envelope models, typical evolutionary timescales for the post-nova phase. They expressed this timescale in terms of the time interval required for T_{eff} to increase by 10 eV near the peak. We find the

corresponding time interval from the MESA models to be larger by a factor between $\sim 10 - 20$ than their models with the highest metal enrichment (ONe75 in their paper) and by a factor of $\lesssim 3$ than their models with the least metal enhancement (ONe25 in their paper). This indicates that mixing may be an important factor in explaining the discrepancy between our predictions and observation of the post-nova SSSs. Alternatively, observations of post-nova SSSs could be used to constrain the mixing in novae. For example, our results demonstrate that the *XMM-Newton* observation results would be incompatible with the most metal enhanced ONe75 model of Sala & Hernanz (2005b), since the much shortened SSS phase from such metal enhancement would have reduced our predicted number of sources by about the same factor of $\sim 10 - 20$. On the other hand, their ONe25 model with less metal enhancement may be quite compatible with our calculations. Furthermore, for novae occurring on massive WDs with very short recurrence time, convection is weak and particle diffusion inefficient to allow for a strong mixing between the WD core and envelope, such that mixing may not be as significant as for the novae on less massive WDs.

Another open issue is the amount of circumstellar absorption produced by the nova ejecta itself or by the mass-loss from the system in general. In order to gauge the importance of this factor, we calculate the neutral hydrogen column density ΔN_{H} required to reduce the predicted number of post-nova SSSs in Sect. 4.5 to the observed value of ≈ 16 . The results are listed in the last column of Table 4.3. As one can see, a moderate absorption by the circumstellar material, at the level of $\sim (1 - 2) \times 10^{21} \text{ cm}^{-2}$ is sufficient to reconcile our predictions with the observed number from *XMM-Newton*. Since the detection of the post-nova SSSs is most likely around the time of their soft X-ray peak luminosities (Eq. 4.1, Fig. 4.3), the effect of circumstellar absorption is therefore most relevant around that time. There are, indeed, results from X-ray observations of novae that indicate the presence of circumstellar N_{H} around the time of their peak soft X-ray emission. For example, Page et al. (2010) carried out spectral fitting of the X-ray observations of V2491 Cyg using blackbody model and Kahabka et al. (1999), that of U Sco using NLTE model and obtained the evolution of N_{H} during their supersoft phase. They find the value of N_{H} for these systems around their peak emission time to be in excess from the interstellar medium by $\sim 10^{21} \text{ cm}^{-2}$. Thus, we see that the ΔN_{H} values that we have found (see Table 4.3) is quite compatible with the observed values.

Further, our predictions are also dependent on the assumptions regarding the shape of the WD mass distribution in novae. One can see from Table 4.3 that in terms of the total number of post-nova SSSs, the dependence is not very strong, the largest difference being of a factor of ~ 2 . Therefore, our comparison of the predicted number of sources with observations is not strongly dependent on the assumed WD mass function in novae. Dependence of the slope of the luminosity function and of the effective temperature distribution, however, is more significant and can strongly affect the number (or probability of occurrence) of luminous and/or high temperature sources, by upto an order of magnitude in the extreme case. Thus, more detailed analysis of the luminosity function and temperature distribution of post-nova SSSs could, in principle, help in placing constraints on the mass distribution of WD in novae. This, of course, requires that other uncertainties of the models are dealt with.

4.7 Summary and conclusions

We have computed the expected population of post-nova SSSs in M31 using the multicycle nova evolutionary models of Wolf et al. (2013), under various assumptions regarding the WD mass distribution in novae. For the latter, we consider the mass distributions obtained from the observed nova statistics in M31, a simple theoretical distribution from Truran & Livio (1986) and an ad hoc flat distribution. Our calculations predict that depending on the assumed WD mass function, there should be about ~ 250 – 600 post-nova SSSs in M31 with intrinsic (unabsorbed) luminosity in the $0.2 - 1.0$ keV band exceeding 10^{36} erg/s, and with combined luminosity of $\sim (2 - 4) \times 10^{39}$ erg/s (Table 4.3). Results obtained for different WD mass distributions are consistent with each other within a factor of ~ 2 . The luminosity functions for all four WD mass distribution models exhibit a cut-off at $L_x \approx 2 \times 10^{38}$ erg/s, which corresponds to the maximum soft X-ray luminosity predicted by the post-nova evolutionary tracks. In a similar manner, the differential T_{eff} distributions for these models have a cut-off at $T_{\text{eff}} \approx 1.5 \times 10^6$ K, corresponding to the highest T_{eff} achieved by the evolutionary tracks.

We compare our predictions with the results of dedicated monitoring of the central part of M31 with *XMM-Newton* (Henze et al. 2010, 2011). Using Monte Carlo simulations and taking into account varying intrinsic absorption in M31 within the *XMM-Newton* FOV, we estimated the total number of post-nova SSSs which should have been detected by *XMM-Newton* in the course of these observations, to be of the order $\approx 30 - 80$. This exceeds by a factor of $\approx 2 - 5$ the actual number of detected sources of ≈ 16 . Taking into account the number and magnitude of uncertainties involved in modeling post-nova SSSs and possible incompleteness of the observed SSS statistics, we consider this as a good agreement. Furthermore, there are several uncertainties and simplifications in our calculations, which tend to overestimate the number of SSSs. Most important among these are the following. The blackbody assumption used for the post-nova SSSs tends to overestimate the soft X-ray luminosity as compared to the NLTE WD atmosphere models. The mixing of the WD core material with the accreted envelope material can shorten the SSS phase and, correspondingly, reduce the number of post-nova SSSs. Finally, the presence of circumstellar material, at an average level of $N_H \sim 10^{21}$ cm $^{-2}$, would fully resolve the discrepancy.

Chapter 5

A novel method for transient detection in high-cadence optical surveys and its application for a systematic search for novae in M31

5.1 Introduction

In time-domain astronomy, the difference imaging (DI) technique (Tomaney & Crotts 1996; Alard & Lupton 1998; Alard 2000) provides an efficient way for source detection. In particular, as compared to the former conventional method of catalog cross-matching, DI provides a more effective strategy for finding variable/transient sources¹ in crowded stellar fields. Such fields, as difficult as they are to access, hold equally rich opportunities for astrophysical studies. DI has thus become the staple choice as is evidenced by its implementation in the majority of the data analysis pipelines of modern time-domain surveys, e.g., the intermediate Palomar Transient Factory (iPTF) survey (see Laher et al. 2014).

The basic principle of DI is to match the point-spread function (PSF) and the background, both of which often vary spatially, between a reference image and an input/science image. This match is accomplished by convolving one of the images, generally the reference image with better seeing and higher signal-to-noise ratio, with the optimal kernel. The determination of the latter forms the most important step for any DI technique (e.g., Alard & Lupton 1998). DI is generally implemented in automated pipelines, particularly for large-scale surveys. Its execution, however, in almost all cases is subject to too many false positives/artifacts compromising the quality of the resulting difference image, especially for the automated case. A multitude of reasons may make the difference images susceptible to artifacts – improper PSF and/or background matching, edges of defective/bad pixels,

¹Here we use the terms variable and transient interchangeably (unless otherwise noted), since the distinction is not important for the major part of this chapter.

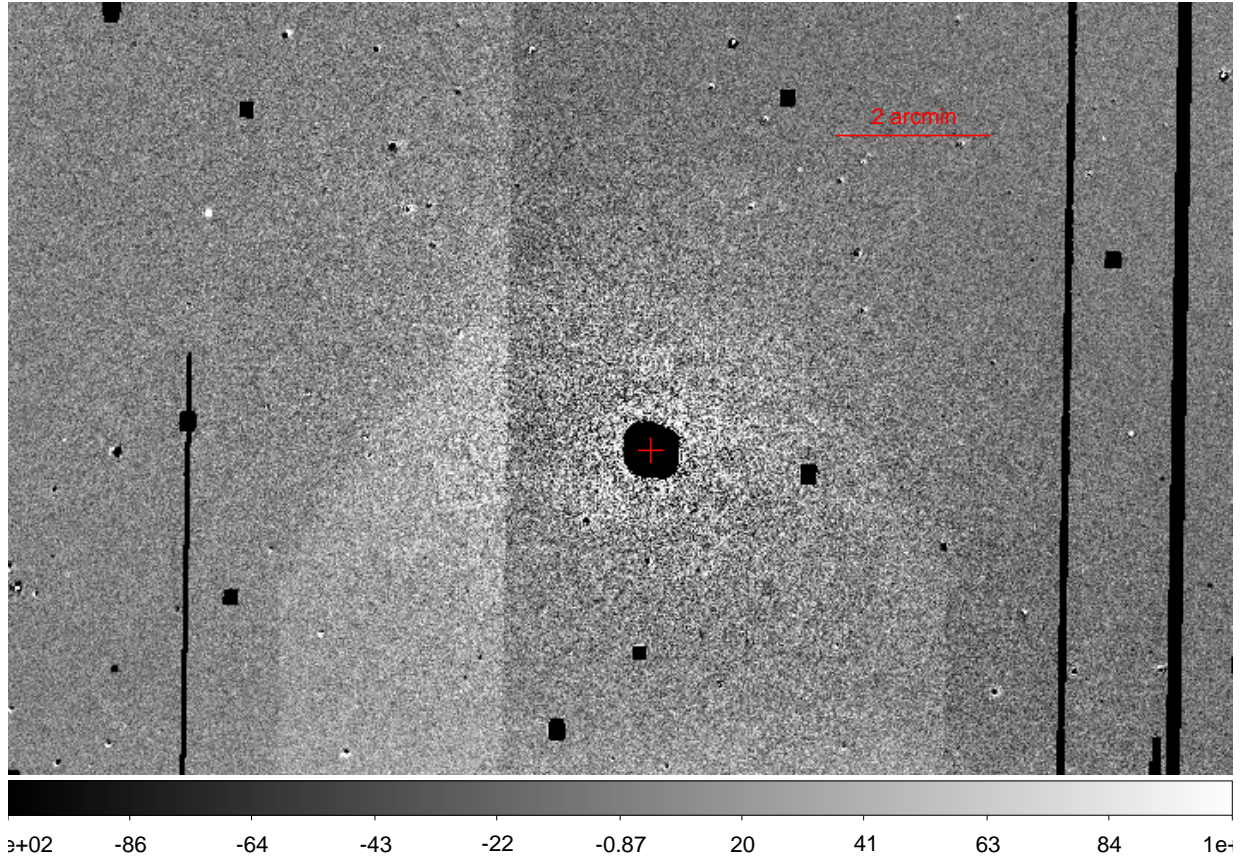


Figure 5.1: A section of a typical M31 field difference image from the iPTF pipeline, containing the bulge. The center of M31 is marked by the cross and the masked areas are assigned large negative values. North is upward and east is left. The vertical sharp edge seen left of the center arises from the boundary of blocks that have been used to match the background before the image subtraction in the iPTF DI pipeline.

cosmic rays, etc. Consequently, the catalogs of sources detected in the difference images generally become contaminated, in fact dominated, by artifacts (see for example Bloom et al. 2012).

Furthermore, when dealing with a field containing a background that is spatially varying and bright, such as the bulge of M31, the DI quality tends to suffer (Kerins et al. 2010). To illustrate this, we zoom in on two parts of a typical difference image of M31 generated by the iPTF DI pipeline (Frank et al., in prep), the bulge part and an outer part about half a degree northward of the center of M31, as shown in Figs. 5.1 and 5.2, respectively. It is clearly evident comparing the two sections of the same difference image, that the residuals in the bulge part have much higher amplitudes than the outer part. As such the bulge part is even more sensitive to artifacts. Thus, the artifact-contamination in the difference image catalogs for such fields worsens toward the bulge.

In this chapter, using iPTF M31 observations, we present a novel method to efficiently

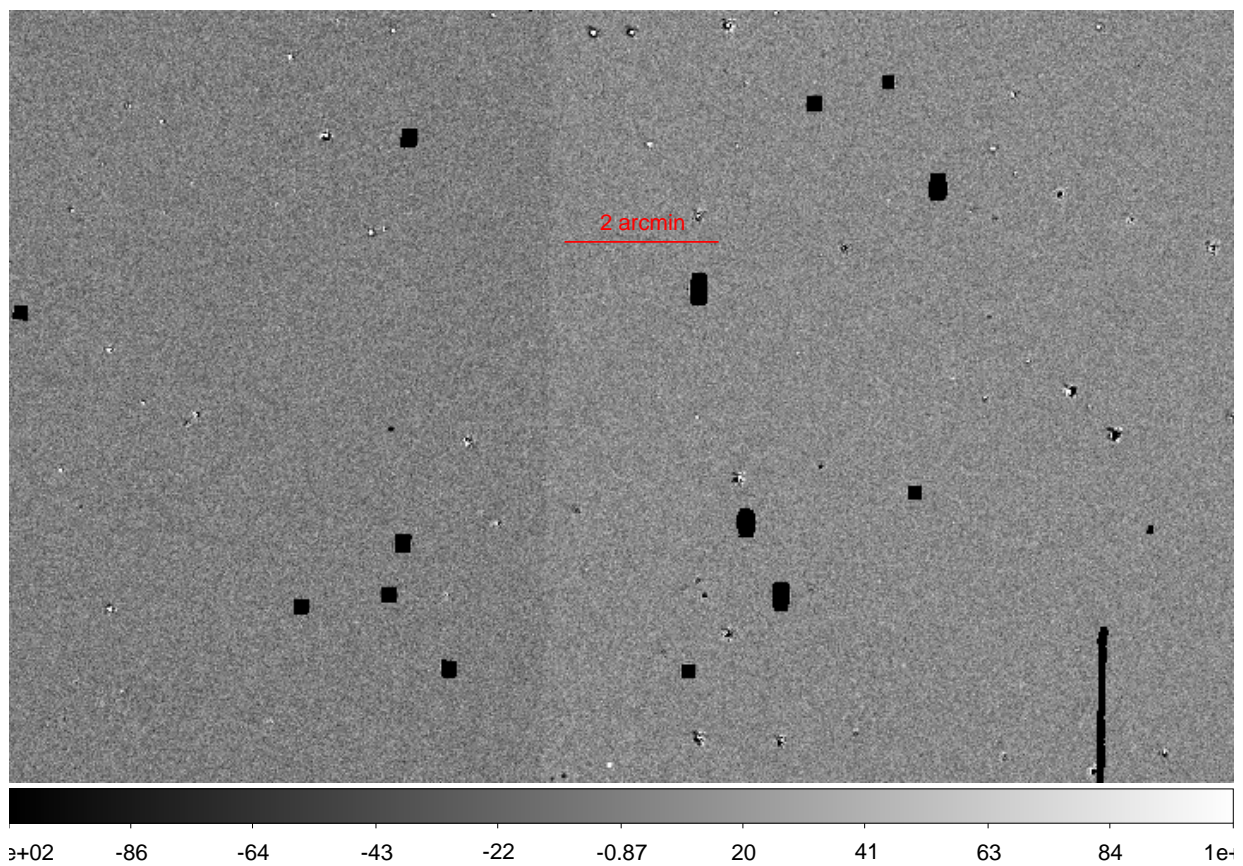


Figure 5.2: The outer part of the same M31 field difference image in Fig. 5.1, about half a degree northward of the center of M31. The masked areas are assigned large negative values. North is upward and east is left. The sharp edge seen in this image is for the same reason as mentioned in the caption of Fig. 5.1.

identify candidates for variable sources and recover candidates even from the bulge, where the DI quality is likely to be low. We then make use of the method to conduct a systematic search for novae in M31. Even if we describe our procedure using iPTF observations, the issues described above are generic and therefore our method is equally applicable to other surveys and other fields. The method involves mapping the sources detected from difference images onto a blank image of the corresponding field, thereby storing their spatial and recurrence information. We call the resulting image as *spatial recurrence image*. In this image, the candidates for variable sources appear as clusters of points over a background of artifacts, which are random and approximately follow Poisson distributions (see Sect. 5.4.2). In this latter aspect of the image, it becomes analogous to an X-ray image. Thus, exploiting the approximately Poissonian nature of the background, we make use of image analysis tools for source detection developed in X-ray astronomy, to obtain a list of unique candidates for variable sources, significantly less contaminated by artifacts. In particular, we use the wavelet-based tool WAVDETECT (Freeman et al. 2002) from the *Chandra* Interactive Analysis of Observations (CIAO; Fruscione et al. 2006) software package. Once the candidates for variable sources are obtained, we then follow the fairly standard practice of searching for novae – we construct the lightcurves for the candidates and then apply cuts based on expected properties of novae.

5.2 iPTF M31 data

The M31 field analyzed here, covering $\approx 1 \times 0.5 \text{ deg}^2$ and including the bulge, was observed by iPTF, which is the successor of the Palomar Transient Factory (Law et al. 2009; Rau et al. 2009), between September 2013 and January 2014, comprising 201 epochs. The exposure time for every observation was 60 seconds. The distribution of the observation epochs is shown in Fig. 5.3.

DI was performed for these epochs by the iPTF DI pipeline, which among other things performs the image convolution for psf-matching using a technique developed by the iPTF team (Frank et al., in prep). The pipeline outputs as primary products photometric tables containing information (celestial coordinates, differential fluxes, etc.) on the sources detected in the difference images. Users are responsible for further characterization of bona fide sources and the subsequent selection of objects of interest. The number of detections against the difference image number is shown in Fig. 5.4. Given that these detections are not artifact-free and thus are to be further cleaned, we here refer to these detections as *raw detections*. The typical number of raw detections per epoch extracted from the difference images by the iPTF pipeline is ~ 1000 , and the total for this season is $\sim 2.5 \cdot 10^5$. The latter value of course includes multiple detections from any single source.

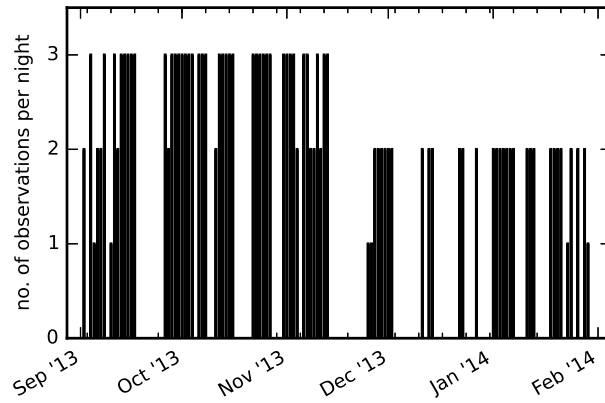


Figure 5.3: Distribution of the observation epochs of the iPTF M31 data analyzed in this chapter. The minor ticks correspond to a week interval. Note that the vertical axis shows the number of observation epochs per night.

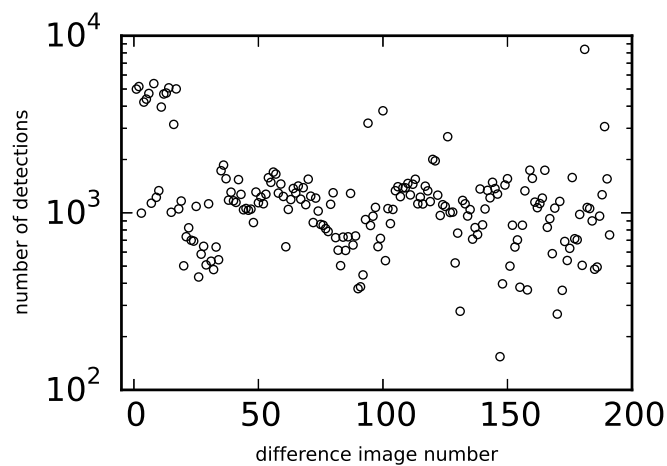


Figure 5.4: The number of sources detected by the iPTF pipeline against the difference image number for the M31 field analyzed here.

5.3 Spatial recurrence map of the raw detections

With the goal of identifying unique variable sources, we construct a spatial recurrence map of all the $\sim 2.5 \cdot 10^5$ raw detections from Sect. 5.2. To this end, we create a blank image of the same M31 field, sampling the pixels at the iPTF scale of $1.01''$ (Law et al. 2009). We then plot all the raw detections in this image, marking their positions with crosses. The resulting image, zoomed in on the bulge and on the outer part, is shown in Figs. 5.5 and 5.6, respectively.

The raw detections from individual sources cluster at the respective positions of the sources on the spatial recurrence image. These clusters can be clearly seen in a sea of single raw detections in the outer part of the M31 field in Fig. 5.6. These give the locations of the candidates for variable as well as transient sources appearing during the observation season, in the M31 field. This procedure thus provides an opportunity to identify unique variable source candidates at one go, without the need for cross-matching the catalogs of raw detections from the DI pipeline. The bulge is, however, swamped by detections (see Fig. 5.5). This is the cumulative effect of the low-quality DI at the bulge (cf. Sect. 5.1). Particularly for large-scale surveys in the time domain, the bulge part of a galaxy is thus one of the main challenges, where the bulk of the candidates are lost using conventional methods of thresholding on the parameters of the raw detections or even via machine-learning algorithms. Our method presented in this chapter improves on this limitation of recovering candidates from the central parts of galaxies.

To facilitate further analysis, we first convert the spatial recurrence image (Figs. 5.5, 5.6) to a counts image, representing each raw detection as one count. In the resulting counts image, which we call here the *hits image*, the pixel value equals the total number of occurrences of a raw detection within the given pixel. This hits image is shown in Fig. 5.7. Certainly some of the non-zero pixels in the image will be sources and the rest artifacts; the artifact contamination is expected to be more drastic in the bulge as can be inferred from the increased crowding in that area.

5.4 The method

In this section, we describe our procedures for identifying candidates for variable sources in the M31 field analyzed. Only minimal information, namely the position of the raw detection in an epoch, is required for the implementation of our method, and this is conveniently stored in the form of the hits image (Fig. 5.7). On this hits image, we perform a series of wavelet transformations using the CIAO tool `WAVDETECT` (Sect. 5.4.1). In Sect. 5.4.2, we assess the applicability of this X-ray tool on the hits image. We analyze the output of `WAVDETECT` in the context of identification of variable source candidates from the products of an automated time-domain data pipeline in Sect. 5.4.3.

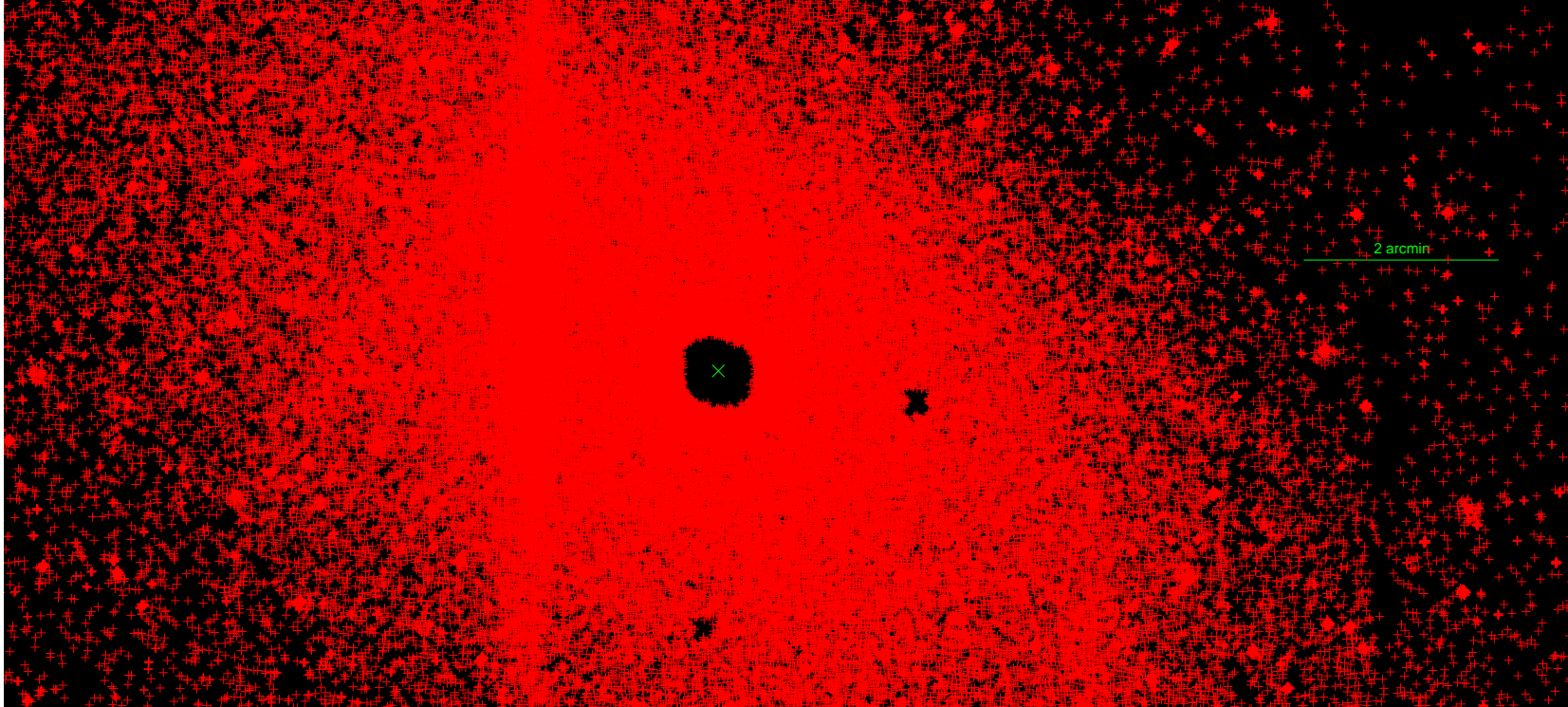


Figure 5.5: The spatial recurrence image zoomed in on the bulge of M31, obtained by projecting the raw detections as red crosses on the coordinate grid of a blank M31 image. The center of M31 is marked by the green cross. North is upward and east is left. Due to saturation close to the center of M31, there are no sources detected by the iPTF pipeline.

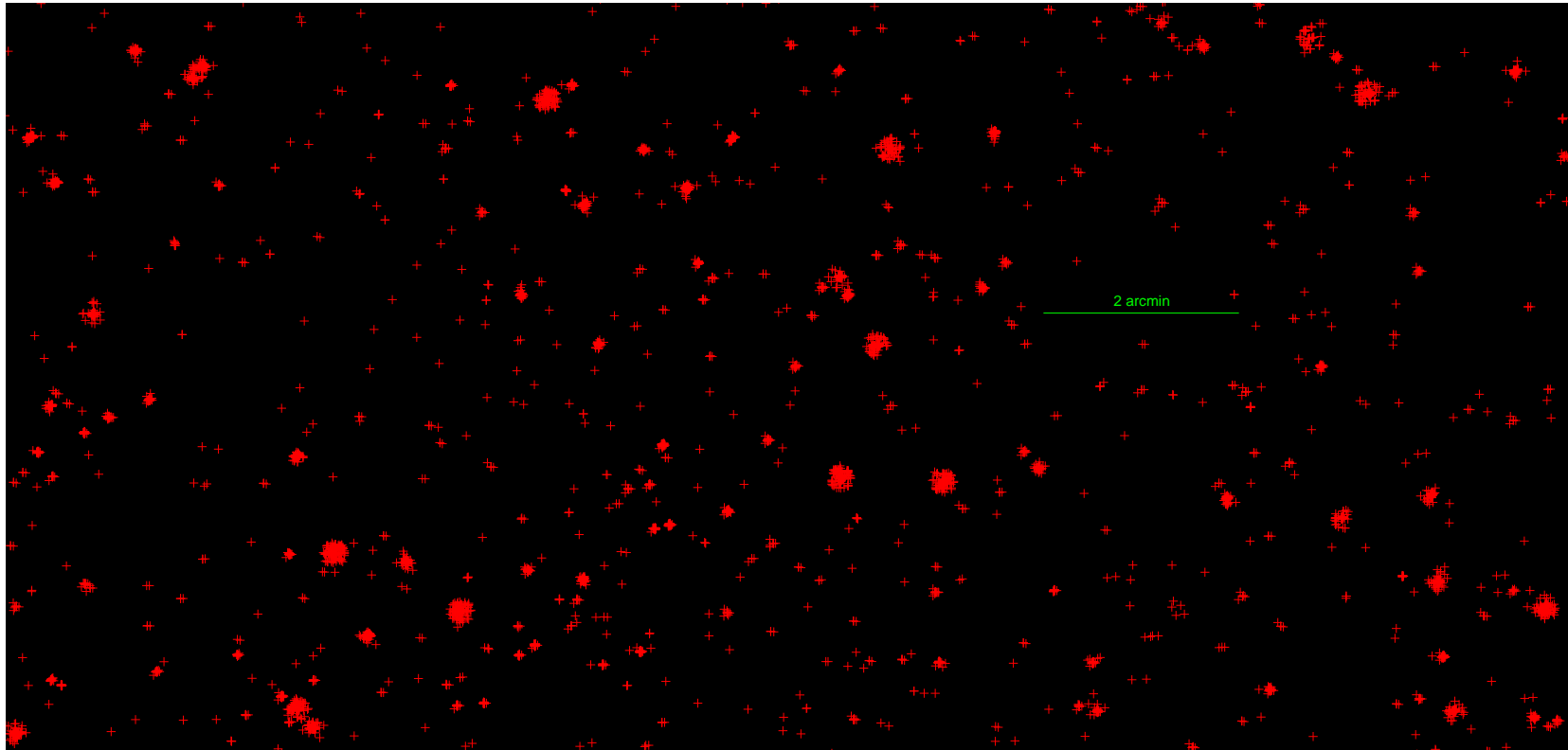


Figure 5.6: The outer part of the spatial recurrence image, about half a degree northward of the center of M31. North is upward and east is left. The red crosses are the projected raw detections.

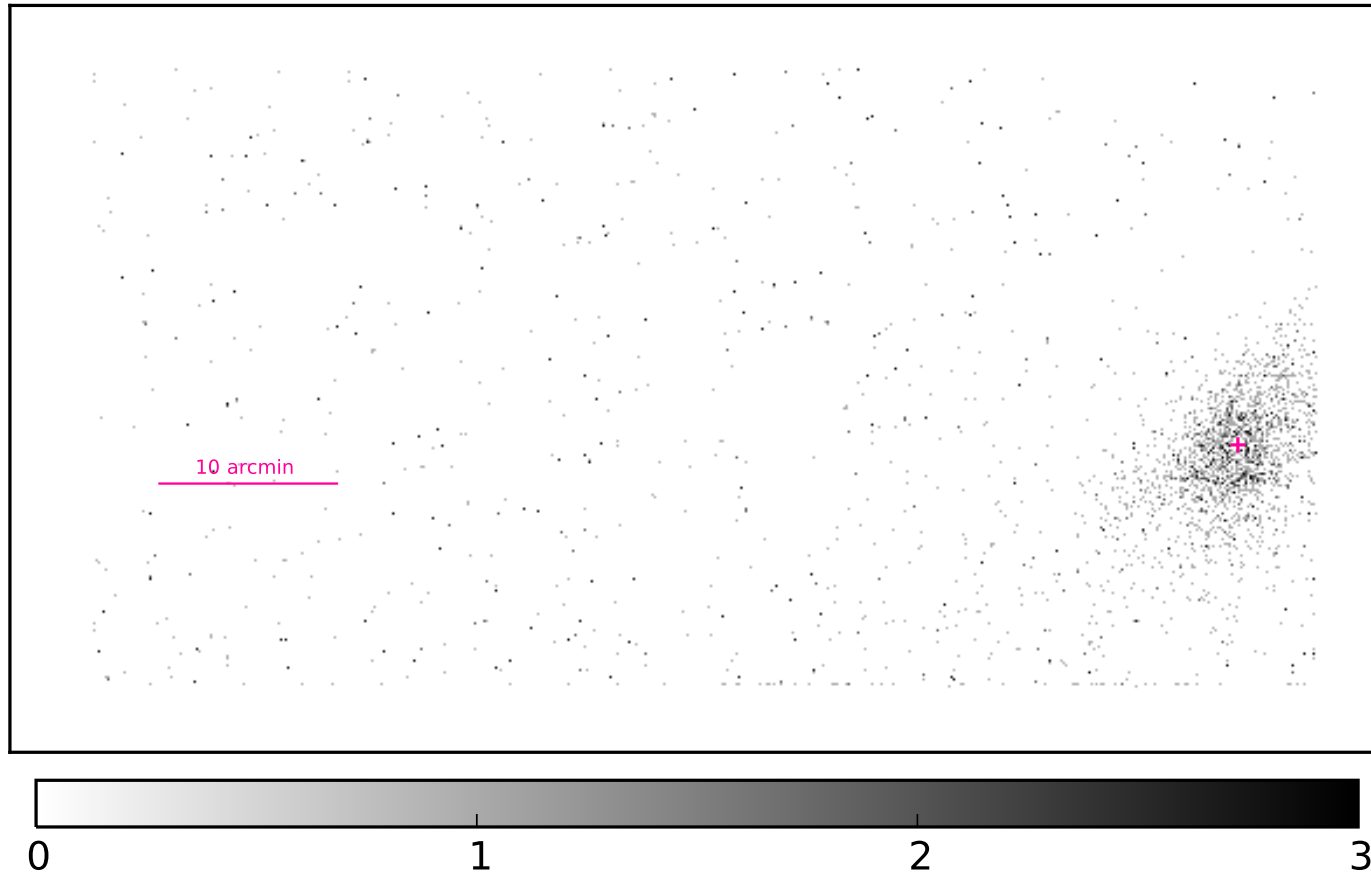


Figure 5.7: The hits image formed by registering the total number of occurrences of any raw detection in the M31 field from the iPTF DI pipeline (see text for details). The center of M31 is marked by the cross; north is toward the left and east is down. Note that the picture is in saturation, i.e., some pixels have values much larger than 3. There are no detections around the edges because we took a slightly larger blank image of M31 than the field analyzed to project the iPTF pipeline detections; however this does not have any effect in the further analysis. The zoomed-in bulge and outer parts of this image can be seen in Figs. 5.8 and 5.9, respectively.

5.4.1 Source detection using WAVDETECT

WAVDETECT is one of the most popular tools for X-ray source detection from the CIAO software package, based on wavelet analysis. In brief, it correlates the Mexican-hat wavelet function with the input image. At every pixel (i, j) , the local background $B_{i,j}$ is estimated using the negative annulus of the wavelet. Based on a user-defined significance value S (see Eq. 5.1), WAVDETECT computes a threshold correlation value ($C_{i,j,0}$) for the pixel. It then identifies source pixels exhibiting correlation coefficients greater than their corresponding thresholds, and then these pixels are grouped into individual sources (see below) thus producing a final list of sources. Mathematically, WAVDETECT determines $C_{i,j,0}$ as

$$S = \int_{C_{i,j,0}}^{\infty} p(C|B_{i,j})dC. \quad (5.1)$$

Here $p(C|B_{i,j})$ is the probability of obtaining the correlation value C for the given background $B_{i,j}$ at the pixel (i, j) . This probability distribution has been determined from simulations (see Freeman et al. 2002 for details), and the results are already encoded within the software. If the correlation value $C_{i,j}$ at pixel (i, j) is greater than $C_{i,j,0}$, then it passes through as a source pixel.

The correlation is performed at multiple wavelet scales defined by the user, where small (large) scales are sensitive to small (large) features. These scales σ define the size of the wavelet; the wavelet crosses zero at $\sqrt{2}\sigma$ and extends effectively up to 5σ . The sources themselves manifest as islands (also called source cells) with some net counts above a background of zero values when the image is smoothed with the positive part of the wavelet at the different scales. The detected pixels are then assigned to their corresponding sources, and the final list of sources is made. The two parameters, namely the significance value/threshold and the wavelet scales, are thus the main inputs for source detection in WAVDETECT.

In processing the hits image via WAVDETECT, we adopt nine different scales ranging from 1 to 16 pixels, in multiplicative steps of $\sqrt{2}$. For the threshold, we choose a value of $S = 10^{-6}$. The M31 field analyzed here encompasses $\sim 10^6$ pixels and therefore the above threshold implies an expectation value of one false positive if the model for $p(C|B_{i,j})$ is precisely correct (see Freeman et al. 2002). WAVDETECT finds 3981 sources in the hits image. Figures 5.8 and 5.9 show the sources found in the bulge and half a degree northward of the center, respectively, which are marked by the green ellipses. It is to be noted that the elliptical regions generated by WAVDETECT are only meant for visualization of the source locations, and do not affect the subsequent operation of WAVDETECT (CIAO; http://cxc.harvard.edu/ciao/download/doc/detect_manual/wav_ref.html).

The interpretation of the WAVDETECT result is that there are 3981 *different* variable source candidates that occurred in the M31 field during the five-month-long iPTF season. Of course, this number may still be contaminated by artifacts that are not modeled accurately by the model for $p(C|B_{i,j})$. However, the number is largely free of the background of single raw detections (cf. Sect. 5.3, Fig. 5.6), as shown in Sect. 5.4.3. Of course, some of these single raw detections may be genuine sources. However, within the cadence of the

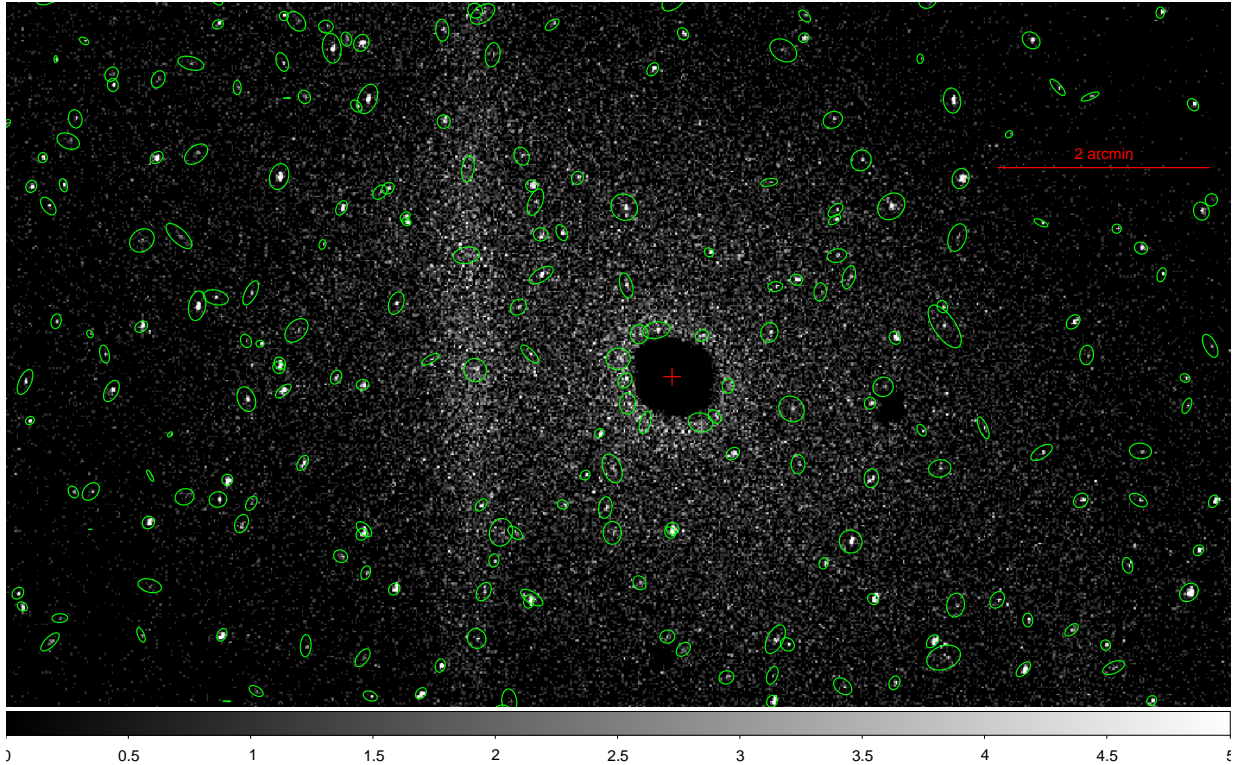


Figure 5.8: The hits image zoomed in on the bulge. Note that the grey-scale in Fig. 5.7 has been reversed here for better contrast with the green ellipses. The red cross marks the center of M31 and the green ellipses show the location of sources found by WAVDETECT in this region. North is upward and east is left. As the area around the center is masked upstream in the iPTF pipeline due to saturation, the corresponding pixels in the hits image have zero values. The stripe that can be seen left of the center arises from the border between blocks used to match the background in the iPTF DI pipeline (cf. Fig. 5.1).

particular observation season, with only a single detection, it is difficult to characterize the nature of such sources.

5.4.2 Applicability of WAVDETECT

In the formulation of the WAVDETECT algorithm, the statistics of the background are tied to the probability distributions of the wavelet correlation values, $p(C|B_{i,j})$ in Eq. (5.1). The algorithm by itself is quite versatile as it can be adapted for any given statistical characteristic of the background by computing the corresponding distribution of $p(C|B_{i,j})$. However, in the implementation of WAVDETECT within the CIAO software package, Poisson statistics for the background are assumed, as it is designed for X-ray data. In general for the algorithm, the statistics of the sources themselves do not come in the picture; what matters is only that they stand out above the Poissonian fluctuations of the background.

As mentioned in Sect. 5.4.1, the distributions for $p(C|B_{i,j})$ in WAVDETECT are computed

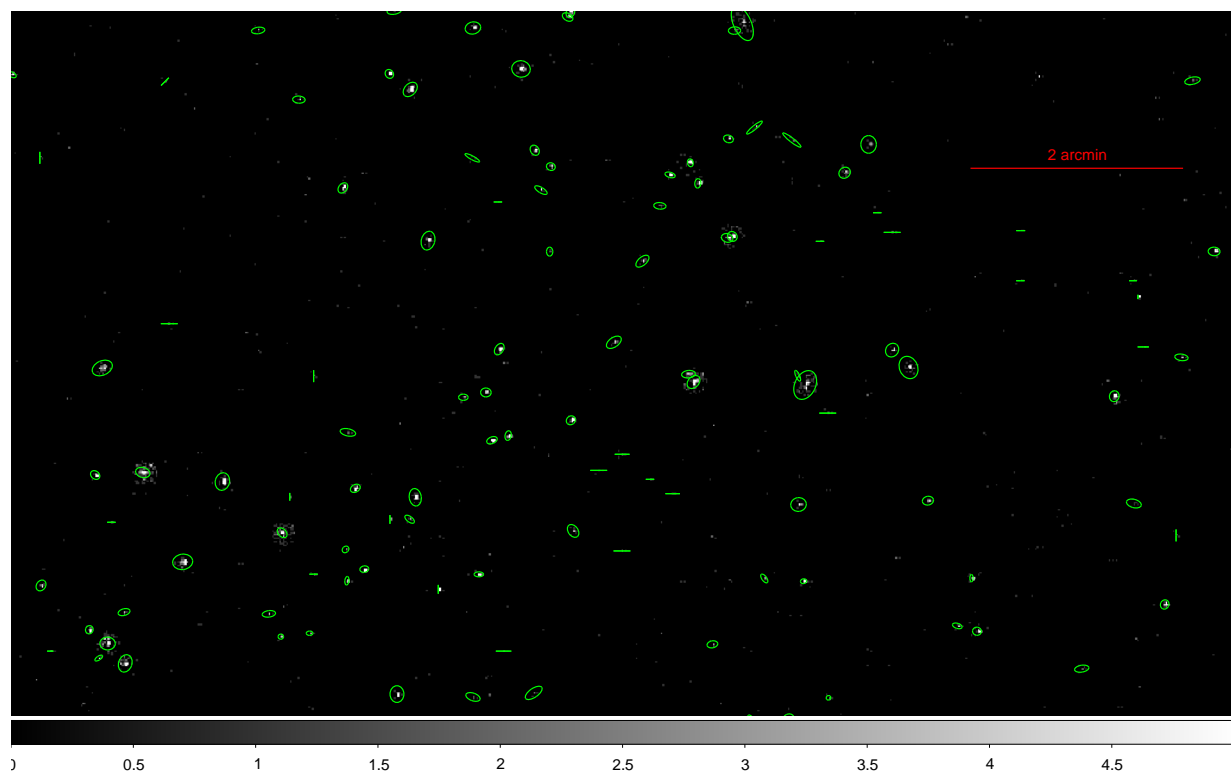


Figure 5.9: The outer part of the hits image, half a degree northward of the M31 center, with the green ellipses showing the location of sources found by WAVDETECT. The shape of the elliptical region characterizes the shape of the distribution of counts within the source cell. Some of these regions output by WAVDETECT may have a very small length along one of the axes, such that they appear like lines; these regions are however only meant for visualization (see text).

from simulations. These simulations assume the background to be sampled from the same Poisson distribution; that is the expectation value of the background is constant (Freeman et al. 2002). However, in real X-ray images, a constant background is definitely an idealization. In the execution of WAVDETECT, the background at a given pixel of the image is estimated from the region covered by the negative annulus of the wavelet centered at the pixel. Thus, the assumption of a constant expectation value for the background is effectively only made for a region of radius 5σ around each pixel. Therefore, as long as there are no sharp variations in the background, the efficacy of WAVDETECT is not affected (Freeman et al. 2002).

When using WAVDETECT on the hits image, we are thus implicitly assuming the above conditions about its background – that it follows Poisson statistics and that the mean values do not vary sharply. These assumed Poisson statistics of the background are incorporated in the background image (let us call it B') that WAVDETECT also outputs for the hits image. To analyze how accurate this assumption is, we compare the pixel value distribution of the actual background of the hits image with that expected based on B' . To this end, we mask out circular areas, each of radius $10''$ (≈ 10 pixels), centered on the sources detected by WAVDETECT to obtain the background of the hits image. For each value of $B'_{i,j}$, we obtain a distribution of pixel values sampled from the Poisson distribution whose expectation value is $B'_{i,j}$. We then sum these distributions and normalize it to the total number of pixels in the sources-masked hits image. The resulting distribution is then compared with the pixel value distribution of the hits image with masked sources. As discussed in Sects. 5.1 and 5.3, the DI quality is systematically inferior in the bulge as compared to the disc (Figs. 5.1 and 5.2). We would therefore expect the backgrounds in the bulge and disc to follow Poisson distributions, with markedly different means. We thus make the above comparison of the pixel value distributions separately for the bulge and disc. We define the bulge of the M31 field as an elliptical region of semi-major axis $6'$ and axis ratio 0.47, centered on the M31 nucleus. The results are shown in the left and right panels of Fig. 5.10, respectively.

As can be seen from Fig 5.10, the background of the hits image does not strictly comply with being Poissonian, but the deviations are not stark. Moreover, even if the background were strictly Poissonian, one might expect that there could be some sources that barely stand out above the background. Those sources may not be detected above the threshold of $S = 10^{-6}$ that we have applied. Thus, these sources would not be masked and they would distort the black histograms in Fig. 5.10. So even if the true background is exactly Poissonian and with a constant expectation value, the two histograms may not look precisely the same. In conclusion, the application of WAVDETECT on the hits image is justified to the accuracy sufficient for the purpose of this analysis.

5.4.3 Characteristics of WAVDETECT detections in the time-domain context

In this section, we explore the characteristics of detections made by WAVDETECT in the hits image (Fig. 5.7) in order to quantify its performance in the context of time-domain astron-

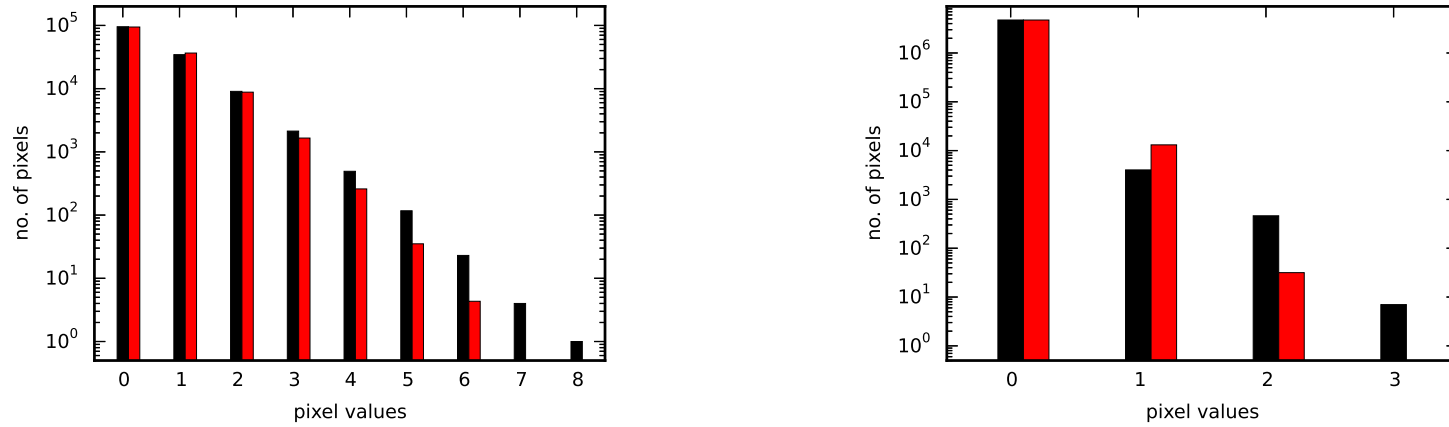


Figure 5.10: Comparison of the background pixel value distribution of the hits image, shown in black, with the distribution expected for Poissonian background, shown in red, obtained using the WAVDETECT output B' (see Sect. 5.4.2), for the bulge (*left*) and for the disc (*right*). It is to be noted that the red histograms have been shifted along the x-axis by pixel value=0.1 for clarity.

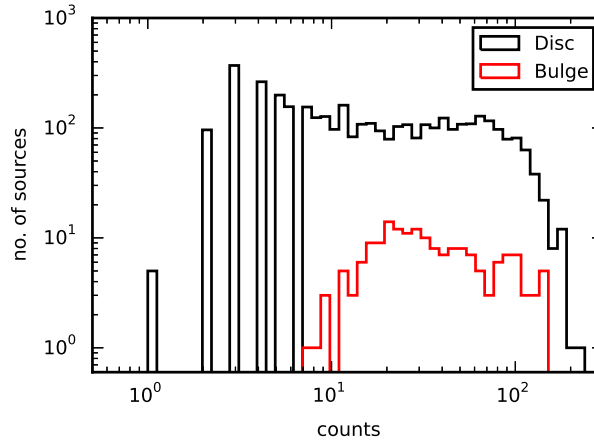


Figure 5.11: Distribution of counts in the source regions for the detections made by WAVDETECT in the bulge and the disc of the iPTF M31 field analyzed here. The five sources in the disc with one count passed through WAVDETECT due to their location in extensive empty areas.

omy. It is quite evident from the pixel value range in the distribution of the background pixel values of the hits image (Fig. 5.10) that the detection threshold ($C_{i,j,0}$ in Eq. 5.1) must be higher in the bulge than in the disc.

Besides the positions of the detected sources, WAVDETECT also includes in its output their counts – the sum of the pixel values in the corresponding source cells (see Sect. 5.4.1). However, these source counts are only crude estimates, since the tool is designed largely for detection and not for flux measurement (CIAO). Of course, the former is our sole objective for use of the WAVDETECT tool. These crude source counts nevertheless allow us to gauge the difference in the sensitivity of WAVDETECT between the bulge and the disc of the M31 field, or in general between fields with sparse and crowded distributions of raw detections from the DI pipeline. The distributions of source counts in the bulge and disc of the hits image are shown in Fig. 5.11. As can be seen, the threshold source count is 7 in the bulge. In the disc, there are five sources detected with just one count; this arises due to these sources being located in extensive void areas, and this is a known feature of WAVDETECT (CIAO). However, they represent only 0.1% of the total number of detections (5 detections in total), and are thus insignificant. Effectively, the threshold count in the disc is 2. The above discussion then implies — in the low background regions, with two counts within a source cell, WAVDETECT interprets it as a source; in the bulge region (Figs. 5.5 and 5.8), due to the high density of the hits, at least seven counts within a source cell are required for reliable detection. Note that these values are for the adopted significance of $S = 10^{-6}$ in running WAVDETECT (Sect. 5.4.1).

As discussed in Sect. 5.4.1, the 3981 sources detected by WAVDETECT in the hits image may not all be genuine sources. For instance, false positives may arise due to imperfect PSF-matching occurring persistently at the same position, for example at the position

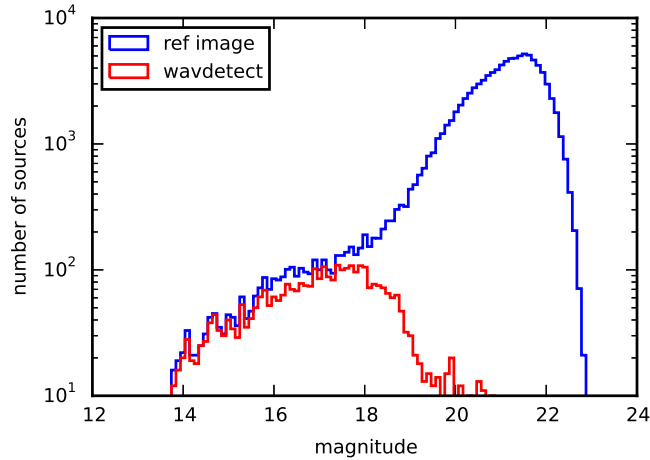


Figure 5.12: Distribution of the magnitudes for the sources detected in the reference image and those WAVDETECT sources with counterparts in the reference image. The magnitudes of these WAVDETECT sources are measured from the reference image.

of a bright star. There may also be WAVDETECT false detections in the regions of high artifact density, for example caused by the deviations of the background distribution from being Poissonian. The latter is particularly relevant for those WAVDETECT sources at the low-count end of the distribution in Fig. 5.11. To assess broadly the nature of possible artifact-contamination, in particular related to intrinsic factors such as imperfect psf and/or background matching, we cross-match the WAVDETECT sources with the sources detected in a deep reference image (co-add of 24 images) of the same field of M31. Out of 3981, we obtained matches for 3525 WAVDETECT sources in the reference image. A matching radius of $2''$ — the typical full width at half maximum (FWHM) for the iPTF observations — was used in the cross-matching. The total number of sources detected in the reference image down to $m_R \approx 23$ is $\sim 10^5$ sources. The typical magnitude limit for individual iPTF M31 observations is $m_R \approx 21$. Out of the 10^5 sources in the reference image, $4.4 \cdot 10^4$ are brighter than this magnitude. Further, of the latter number of sources, about 2000 are in the bulge. This gives 1 source per $\sim 80 \text{ arcsec}^2$ in the bulge; for the disc we obtain 1 source per 270 arcsec^2 . We thus find the probability for false-match in the bulge to be around 0.15 and that in the disc of M31 to be 0.05. With these values, the expected number of false matches is ~ 200 , which is only 5% of the total matches. The magnitude (in the R band) distribution for the matched sources is shown in Fig. 5.12, along with that of all the sources in the reference image. Note that the magnitudes of the matched WAVDETECT sources are those measured in the reference image itself. Quite interestingly, the bulk of the bright sources in the reference image are being detected in the difference images of the iPTF pipeline. Among these matches, some fraction may be genuinely variable stars, but some may be due to systematics in the iPTF DI pipeline caused by imperfect PSF and background matching procedure. Classification of artifacts from these sources is however beyond the scope of this work.

Table 5.1: Summary of WAVDETECT detections

Raw detections from iPTF pipeline (not necessarily unique sources)	254765
Number of unique sources obtained from WAVDETECT	3981
Total number of raw detections encompassed by the WAVDETECT sources	120287
Number of WAVDETECT sources with counterparts in the reference image	3525
Number of transient candidates	456

Further, the remaining 456 WAVDETECT sources are then candidates for transients (different from variable sources in this context). The factors that can cause artifact-contamination for this subset, if any, may include image edges, and imperfect background matching. The latter, however, have to occur persistently in the same location on the sky. Thus, for transients, our method efficiently scales down the search sample by three orders of magnitude from the raw detections of $\sim 10^5$ to a sample of $\sim 10^2$ candidates. In Table 5.1, we summarize the characteristics of the WAVDETECT detections.

5.5 A systematic search for novae in the iPTF M31 observations

With the set of unique candidates for variable sources obtained via WAVDETECT (Sect. 5.4.1), it becomes feasible to search for any class of objects of interest. Hereupon we simply need to resort to the routine procedure of constructing lightcurves and making the selection based on the expected behavior of the objects' lightcurves. With an efficient algorithm, the few thousand candidates obtained in Sect. 5.4.1 can be reduced to a set of a few (depending on the intrinsic population of the class of objects), optimized for the class of objects of interest. In particular, we make a systematic search for novae among the 3981 variable source candidates found above. We make use of all the candidates because we cannot rule out the possibility of a nova having a counterpart in the reference image before it erupted. Indeed, the reference image is quite deep, reaching $m_R = 23$ (Sect. 5.4.3), and the quiescence magnitudes of novae in M31 measured by Williams et al. (2014) reach values of $m_R \sim 22$. Our filtering procedures are described in the following subsections.

5.5.1 Lightcurve construction via forced photometry

Once the locations of the different candidate sources are identified, we proceed to construct their lightcurves using the whole set of raw images per candidate. In other words, we perform forced photometry at these positions, i.e., we measure the fluxes of the candidates at all epochs irrespective of whether or not they are detected in a given epoch by the iPTF DI pipeline. Of course, if the source did not appear at all at an epoch, we will not have a

flux measurement in its lightcurve at this epoch.

As the M31 field we are dealing with contains the crowded bulge, we have opted for profile-fitting photometry using DAOPHOT (Stetson 1987). In its routine execution, DAOPHOT performs a three-step procedure: 1) Find sources in a given image above a user-defined threshold relative to the background noise. The positions of the sources are stored in a source list. 2) Construct a model of the psf profile using some user-defined number of bright stars from these sources. 3) By fitting this profile, accounting for overlapping cases, improved positions and magnitudes relative to the psf profile (which we call *psf magnitudes*) are measured for all the sources. In our implementation for photometry of the variable source candidates, we add their coordinates obtained from WAVDETECT to the source list built by DAOPHOT for each image. The candidates are tracked using unique IDs that we create for them for inserting in the DAOPHOT source list. To avoid confusion, we remove any copies of the candidates in the initial DAOPHOT source list.

In cases where a candidate is not present at all, DAOPHOT will not return flux measurements for it. On the other hand, the forced photometry implementation within DAOPHOT, allows the search of the brightest source within a certain small region around the given position. This may lead to appearance of false detections. The brightness of such detections is near the sensitivity limit of iPTF, around $m_R \approx 21\text{--}22$.

After running DAOPHOT with the candidates included, we obtain their psf magnitudes as well as improved positions. The resulting psf magnitudes are then converted to calibrated magnitudes using DAOGROW (Stetson 1990) and the iPTF photometric calibration relation from Ofek et al. (2012). In this manner, we run DAOPHOT for all the images taken during the season and then construct the lightcurves for the candidates. Four examples of the obtained lightcurves are shown in Fig. 5.13. As can be seen in the figure, three of the lightcurves exhibit clear distinct features of periodic variability, whereas the remaining one is almost flat and featureless, and therefore may be an artifact.

5.5.2 Lightcurve filtering for novae

In this section, we devise an algorithm for carrying out a systematic search of novae in the iPTF M31 field using the candidates' lightcurves obtained in the previous subsection. Given that novae are eruptions, we build our selection algorithm targeting this type of lightcurves.

The steps implemented in our algorithm are based on simple statistical analyses of the lightcurves of the candidates. As a starting point, we are looking for lightcurves with a contiguous section of excess brightness; let us call it *flare section*. In order to make sure the flare section is real, we want to have at least 5 points within it. To define whether a point is in this section, a baseline is needed to compare against. We thus proceed to define the baseline magnitude by computing the mean of all the data points, excluding the flare section (see below), requiring that the lightcurve has at least 10 data points. We throw away all lightcurves with fewer than 10 data points.

To exclude possible contribution of any eruptive part in the lightcurve, the baseline is computed iteratively by clipping contiguous sections of five data points meeting the criteria

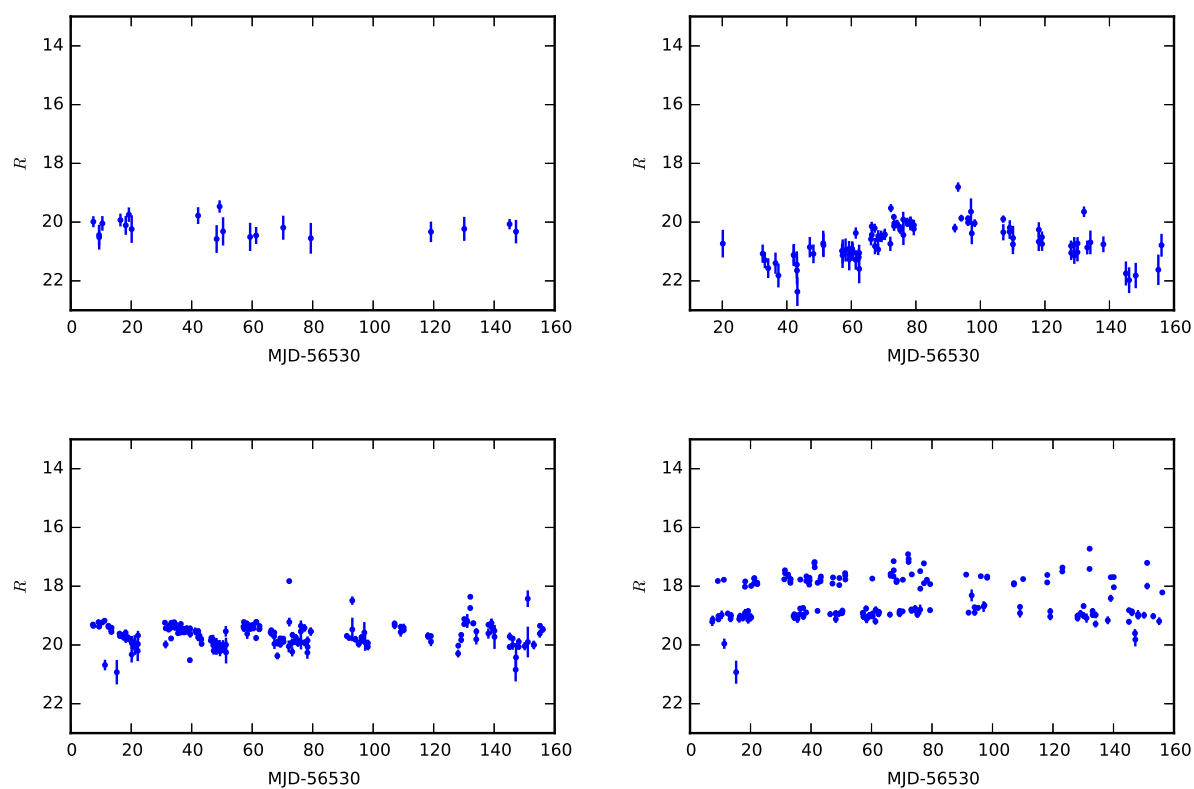


Figure 5.13: Examples of lightcurves of the candidates constructed via forced photometry using DAOPHOT (see Sect. 5.5.1 for details). The lightcurve in the top left panel is likely an artifact, while the one on top right appears to be that of a genuine variable source. Both lightcurves at the bottom panels are those of periodic variables.

listed below.

1. All five points are at least 1 sigma (the standard deviation) brighter than the present “baseline”.
2. The brightest of the five points is at least 2 sigma brighter than this “baseline”.

Then the following selection criteria are applied. It is to be noted that we fine-tuned the values of the parameters used below from a few runs of the selection algorithm. Visual examination of the resulting lightcurves from the first few runs essentially gave us some obvious novae that have been used as a training set.

1. There is a contiguous section of five or more data points, which are at least 1.5 sigma brighter than the baseline. Note that we used a lower value of sigma above in computing the baseline; this is because we want to avoid any bias from the rising part(s) of the lightcurves as far as possible.
2. The peak of the light curve, defined as the brightest point in the longest contiguous section (L) from step 1, is brighter than the baseline by at least 1 mag. We term this peak the *primary peak*.
3. The number of local peaks outside the section L, and whose magnitudes are within 1 mag from the primary peak, is less than half of the number of data points in the section L used to define the primary peak. This particular step is invoked to filter lightcurves that fulfill criteria defined in the above two steps, but contain additional isolated bright points, almost comparable in brightness to the primary peak.

After passing the 3981 candidate lightcurves (Sect. 5.5.1) through the above selection algorithm, we obtain a set of eight nova candidates.

5.6 Results

The lightcurves of the final eight nova candidates are shown in Fig. 5.14. From the M31 optical nova catalog maintained at MPE² (Pietsch et al. 2007), we are able to verify that all eight of them are indeed confirmed novae. The names of these candidates in the MPE catalog are M31N 2014-01a, M31N 2013-10c, M31N 2013-10h, M31N 2013-10a, M31N 2013-09a, M31N 2013-10g, M31N 2013-09c, and M31N 2014-01b, respectively, for candidates 1 to 8.

During the five months period between September 2013 and January 2014, when these data were taken, 13 novae (occurring in the field examined here) have been registered at the MPE catalog by different authors based on observations with different telescope facilities. We list the 13 novae in Table 5.2. Of these, we have recovered eight using our

²http://www.mpe.mpg.de/~m31novae/opt/m31/M31_table.html

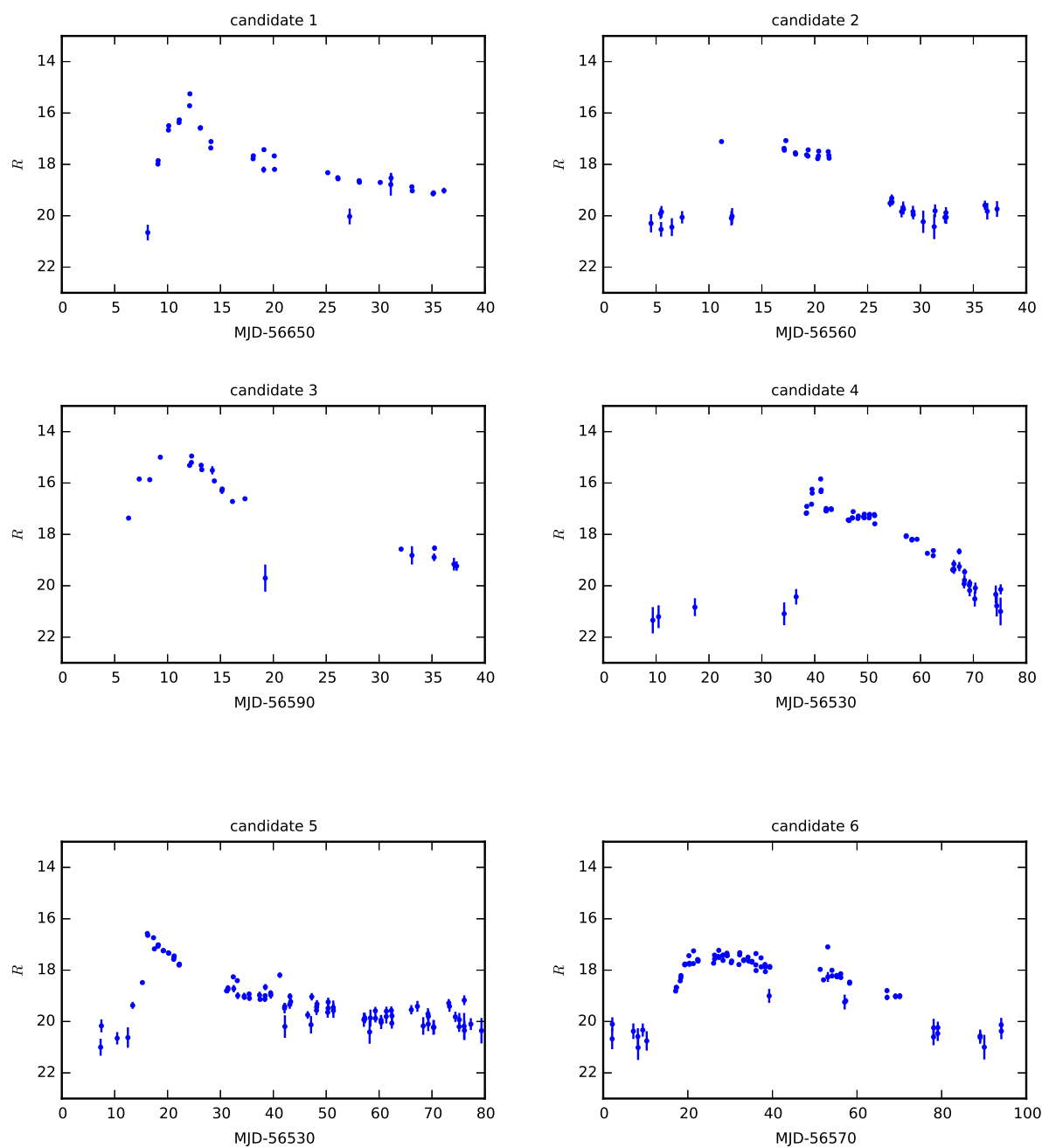


Figure 5.14: Lightcurves of the eight candidates obtained from the nova selection algorithm (see Sect. 5.5.2). It is to be noted that the faint magnitude ($R = 20-22$) measurements in the lightcurves are as produced by DAOPHOT at the location of the object and they need not necessarily represent quiescence magnitudes of the novae.

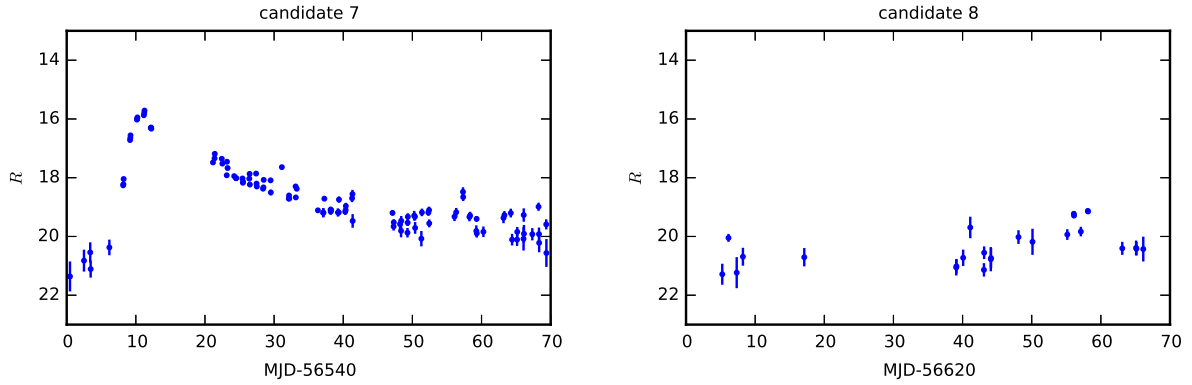


Figure 5.14: continued.

Table 5.2: iPTF recovery of M31 novae reported between 09/2013 and 01/2014

Nova name	Reference	Recovered?
M31N 2013-09a	Sturm et al. (2013b)	Yes
M31N 2013-09c	Hornoch et al. (2013)	Yes
M31N 2013-10a	Hornoch et al. (2013)	Yes
M31N 2013-10b	Hornoch & Vrstil (2013)	No
M31N 2013-10c	Hornoch et al. (2013)	Yes
M31N 2013-10e	Hornoch et al. (2013)	No
M31N 2013-10g	Tang et al. (2013)	Yes
M31N 2013-10h	Sturm et al. (2013a)	Yes
M31N 2013-12a	Sturm et al. (2013c)	No
M31N 2013-12b	Hornoch & Kucakova (2013)	No
M31N 2014-01a	Fabrika et al. (2014)	Yes
M31N 2014-01b	Tang et al. (2014b)	Yes
M31N 2014-01c	Hornoch & Kucakova (2014)	No

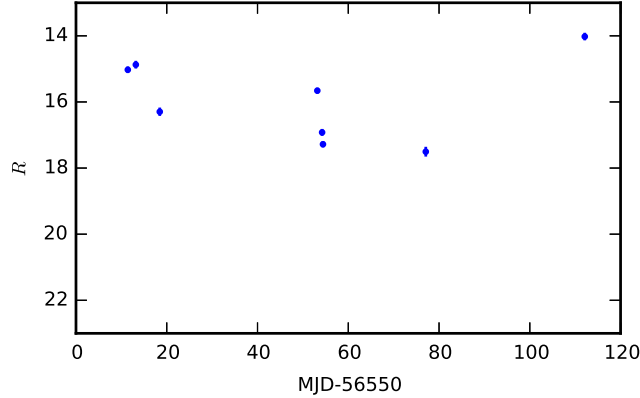


Figure 5.15: Lightcurve obtained using DAOPHOT for the candidate at the position of nova M31N 2013-10b. This nova, reported by Hornoch & Vrástil (2013), was missed by our selection algorithm given its erratic lightcurve. The latter is possibly due to the failure of DAOPHOT in deblending at its location with the extreme stellar density.

method. We have investigated the reasons for missing the remaining five. M31N 2013-10e was missed due to saturation of the pixels (which get masked early on in the iPTF data pipeline) during its eruption. M31N 2013-12a and M31N 2013-12b were missed due to gaps in the temporal sampling (i.e., no iPTF observations) during their eruptions. M31N 2014-01c occurred close to the center of M31 at the end of January 2014, which is near the end of the season analyzed here. The iPTF DI pipeline detected this nova only 5 times when it erupted. This value is, however, insufficient for its detection in the densely crowded bulge (cf. Fig. 5.8) by WAVDETECT, which requires at least 7 hits (see also Sect. 5.4.3). With data extending beyond January 2014, this nova would most likely have been detected by WAVDETECT. Finally, M31N 2013-10b, located closest to the center of M31 (within $1'$), exhibited an erratic non-eruptive-like lightcurve, which also contained less than 10 points (see Fig. 5.15). This candidate was detected by WAVDETECT, but did not pass the lightcurve filter. The magnitudes reported by Hornoch & Vrástil (2013) at its discovery (around modified Julian date 56570) are fainter from the values in Fig. 5.15 by ~ 2 mags. The nova nature of this object was based only on narrow-band H-alpha photometry (Hornoch et al. 2013) and not on spectroscopic data. This object, therefore, is open for further investigation.

The fact that the whole procedure involved in this search for novae is automated, makes it possible to quantitatively characterize any incompleteness in the sample. In fact, all the effects discussed above that have led to missing the five novae can be taken into account when computing the sample completeness. This is left for future work, following the analysis of a much larger iPTF data set of M31.

From the discussion above, the MPE nova catalog appears more complete than the iPTF nova sample obtained here. The former is mainly thanks to the many amateur astronomers

who made the discoveries of the individual novae. However, data from surveys are better-suited for statistical studies of the nova population, since surveys provide the advantage of uniform coverage in various aspects of the observations, for example detectors used, that allows a robust computation of the sample completeness (see also Sect. 5.7). These results thus demonstrate that the method we have presented in this chapter provides an efficient, yet simple, way to analyze the outputs of time-domain data pipelines. By suitably modifying the lightcurve selection algorithm (Sect. 5.5.2), the method can be easily applied for analyzing different kinds of variable sources, for example, periodic variables, cepheids, etc.

5.7 Discussion

We have adapted a wavelet-based tool for source detection in X-ray data for filtering out artifacts in optical time-domain data-pipeline products. Enforcing further a second stage of artifact-filtering based on lightcurve analysis, the data become completely cleaned, populated only by the object(s) of interest.

As shown in Sect. 5.4.2, the artifacts accumulated over all observations form a background following nearly Poissonian distributions in the spatial recurrence/hits image (Figs. 5.5, 5.6, 5.7), much like in an X-ray image, while the candidates for variable sources appear as clusters of points (cf. Fig. 5.6). Multi-scale wavelet analysis provides one of the most convenient means to detect structures/sources in X-ray images. We have thus chosen the popular wavelet-based tool `WAVDETECT` from the `CIAO` package (see Freeman et al. 2002) for the identification of the clusters in the hits image.

The method presented here is, in principle, well-suited for archival and not real-time time-domain data analysis. However, for the modern time-domain surveys (iPTF or the upcoming LSST), cadences for particular fields could range from hours to even minutes per night, such that the total number of visits during the night can sum up to $\gtrsim 2$. In such cases, our method can be straightforwardly implemented to obtain the unique candidates for variable sources near real-time.

Further, the prospects of this method are tremendous when it comes to investigating the *populations* of variable objects. It can successfully probe the variable sources even in the regions severely affected by low-quality DI, for example the bulge of M31 or the Galactic plane, which could not practically be achieved earlier in large-scale surveys. Without much effort, the method can be implemented within the automated DI pipeline of the surveys, which will then directly yield outputs ready for astrophysical studies.

We have demonstrated the procedures of our new method using five-month-long iPTF M31 observations and applied it to conduct a systematic search for novae by establishing a selection algorithm for the lightcurves of the candidates targeted toward novae. We have recovered 8 of 13 novae that were reported to occur during the period of these observations. We have verified that the remaining 5 were missed for legitimate reasons (Sect. 5.6) — one due to pixel-saturation, three due to time-coverage, and one was rejected by the lightcurve filtering. The latter is, however, open for further investigation to concretely establish the

nova nature. Of course the 13 novae need not represent a complete sample for the given period (see Sect. 5.6). However, the fact that all the procedures involved in analyzing the data for novae – from DI to final lightcurve filtering – are automated will allow to quantify the completeness of the results, as will be done in a future work with a larger sample. We can already make a crude estimate for the completeness of the present sample. From Sect. 3.4, the approximate nova rate for the whole M31 galaxy is 106/yr, free from any incompleteness effects. The iPTF M31 field analyzed here encloses roughly 40% of the total stellar mass of M31, and therefore we expect ~ 17 novae to occur during the five months period of the iPTF M31 observations used here. From our systematic search of novae in these data, we have obtained eight of them, which implies a completeness of the sample of $\sim 50\%$.

With the high cadence of the iPTF survey, we anticipate to obtain an M31 nova sample particularly containing those with short decline times. Fast novae are predicted by theories (e.g., Yaron et al. 2005) to occur on massive white dwarfs (WDs) and therefore are imperative for determining the WD mass distribution in novae toward the interesting massive end (see Soraisam et al. 2016). Furthermore, their significance for tightening further the constraints of the nova contribution to the supernova Ia rates has been detailed by Soraisam & Gilfanov (2015). However, their population is to date unconstrained for any galaxy. We have thus set out to apply our method for conducting a systematic search of novae in iPTF M31 observations. We are presently analyzing a much larger data set (covering two years from 2013 to 2015) than the 201 epochs used here, to obtain an iPTF M31 nova sample and to perform its statistical analysis, which will be published in follow-up papers.

5.8 Summary

We have presented a new efficient method for tackling the menace of artifacts contaminating the genuine sources detected by automated time-domain data pipelines. We have used a five-month-long iPTF observations of M31 covering its crowded bulge, with $\sim 10^5$ detections by the iPTF DI pipeline, to illustrate the methodology. The principal basis of our method is stacking the time-series of the spatial distribution of the raw detections made by the DI pipeline, thus obtaining a spatial recurrence image, or hits image after summing the number of detections per pixel (Sect. 5.3, Figs. 5.5, 5.6, 5.7). In such an image, the variable source candidates form clusters similar to X-ray sources and manifest a background following Poisson distributions (Sect. 5.4.2). As wavelet transformation is one of the most robust tools for identifying structures in images, we have imported one such wavelet-based tool for X-ray data analysis, called `WAVDETECT`, from the `CIAO` software package, for our analysis of the hits image. Running `WAVDETECT` on it, we obtained the unique candidates for variable sources appearing during the whole observation season at once, numbering $\sim 4 \cdot 10^3$. Moreover, this method is found to be efficient in handling the crowded bulge, which is generally affected by low-quality DI. For the threshold of `WAVDETECT` used in our analysis — a false positive rate of 1 in the whole field for the assumed Poisson statistics of the background — it is sensitive to variable sources in the bulge that have been detected at

least seven times by the DI pipeline; its sensitivity further improves in the disc, extending to sources detected at least two times by the DI pipeline.

Cross-matching the WAVDETECT sources with the source-catalog of a deep reference image of the same M31 field, we found that $\sim 90\%$ of these variable source candidates have counterparts in the reference image; in fact almost all of the sources at the bright end of the magnitude distribution (Fig. 5.12) of the reference image have been detected on the difference images. This may be due to some of the bright sources being genuinely variable and others due to some systematics in the DI pipeline against such sources. Only a mere ~ 450 candidates remained without counterparts among bright sources, thus representing transient candidates – a three order of magnitude reduction from the initial number of DI pipeline detections.

We then used the variable source candidates obtained via WAVDETECT to search for novae. To this end, we used the locations of the sources detected to construct lightcurves through forced photometry based on profile fitting. Then, applying an automated selection algorithm based on properties of novae, the lightcurves were filtered for nova candidates. We have obtained eight candidates, which we have verified to be confirmed novae from the MPE nova catalog. Given the automated nature of the entire procedure, any incompleteness can be easily computed. This will be done in the future, following the analysis of a larger iPTF data set of M31 spanning around two years. Our method can be applied to any survey of any field for probing any type(s) of variable sources by only making suitable cuts in selecting the lightcurves.

Chapter 6

Conclusions and outlook

With the progenitors of SNe Ia still eluding direct detections, various types of accreting WDs have been proposed as potential candidates. One of the possibilities are WDs undergoing unstable nuclear burning on their surfaces. Although observations and theoretical modeling of classical novae generally suggest that more material is ejected during the explosion than is accreted, there is growing evidence that in certain accretion regimes of novae, appreciable mass accumulation by the WD in the course of unstable nuclear burning is possible. We propose that statistics of novae in nearby galaxies may be a powerful tool to determine the role these systems play in producing SNe Ia. We use multicycle nova evolutionary models to compute the number and temporal distribution of novae that would be produced by a typical SN Ia progenitor before it reached the Chandrasekhar mass limit and exploded, assuming that it experienced unstable nuclear burning during its entire accretion history. We then use the observed nova rate in M31 to constrain the maximal contribution of the nova channel to the SN Ia rate in this galaxy.

The M31 nova rate measured by the POINT-AGAPE survey is $\approx 65 \text{ yr}^{-1}$. Assuming that all these novae will reach M_{ch} , we estimate the maximal SN Ia rate novae may produce, which is $\lesssim 0.1\text{--}0.5 \times 10^{-3} \text{ yr}^{-1}$. This constrains the overall contribution of the nova channel to the SN Ia rate to $\lesssim 2\text{--}7\%$. However, if all the POINT-AGAPE novae do eventually reach M_{ch} , a significant population of fast novae ($t_2 \lesssim 10$ days) originating from the most massive WDs is expected, with a rate of $\sim 200\text{--}300 \text{ yr}^{-1}$, which is significantly higher than currently observed. We point out that statistics of such fast novae can provide powerful diagnostics of the contribution of the nova channel to the final stage of mass accumulation by the SD SN Ia progenitors. To explore the prospects of their use, we investigate the efficiency of detecting fast novae as a function of the limiting magnitude and temporal sampling of a nova survey of M31 by a PTF class telescope. We find that a survey with the limiting magnitude of $m_R \approx 22$, observing at least every second night, will catch $\approx 90\%$ of fast novae expected in the SD scenario. Such surveys should be detecting fast novae in M31 at a rate on the order of $\gtrsim 10^3 \times f$ per year, where f is the fraction of SNe Ia that accreted in the unstable nuclear burning regime while accumulating the final $\Delta M \approx 0.1 M_{\odot}$ before the supernova explosion.

Given the possibility of a SN Ia progenitor to make excursions into the various mass-

accretion regimes (Fig. 1.2), we also derive constraints on the fraction of mass that can be accumulated by the progenitor in the different regimes. To this end, we obtain the observed WD mass distribution in novae. As the high-mass end of this distribution is probed by fast novae, which are not included in the POINT-AGAPE sample, we supplement this sample with fast novae from Arp’s survey of M31 (Arp 1956). For the latter sample, we perform an approximate incompleteness calculation based on the method developed in Chapter 2. We find that significant mass accumulation in the unstable nuclear burning regime, at the level of 10–60%, is only possible for WDs with mass $M_{\text{WD}} \lesssim 1.30 M_{\odot}$. More massive WDs can only accumulate 2% of the required mass without violating the nova statistics in M31. Thus, the final stage of the mass accumulation and the SN Ia explosion cannot occur at low \dot{M} , when the nuclear burning is unstable.

Following the nova explosion, the flux gets redistributed at shorter wavelengths. As a result, novae also undergo a supersoft X-ray phase of varying duration after the optical outburst. Such transient post-nova SSSs are the majority of the observed SSSs in M31. Using the post-nova evolutionary models of Wolf et al. (2013), we compute the expected population of post-nova SSSs in M31. We predict that depending on the assumptions about the WD mass distribution in novae, at any instant there are about 250–600 post-nova SSSs in M31 with (unabsorbed) 0.2–1.0 keV luminosity $L_x \geq 10^{36}$ erg/s. Their combined unabsorbed luminosity is of the order of $\sim 10^{39}$ erg/s. Their luminosity distribution shows significant steepening around $\log(L_x) \sim 37.7 - 38$ and becomes zero at $L_x \approx 2 \times 10^{38}$ erg/s, the maximum L_x achieved in the post-nova evolutionary tracks. Their effective temperature distribution has a roughly power-law shape with differential slope of $\approx 4-6$ up to the maximum temperature of $T_{\text{eff}} \approx 1.5 \times 10^6$ K. We compare our predictions with the results of the *XMM-Newton* monitoring of the central field of M31 between 2006 and 2009. The predicted number of post-nova SSSs exceeds the observed number by a factor of $\approx 2-5$, depending on the assumed WD mass distribution in novae. This is good agreement, considering the number and magnitude of uncertainties involved in calculations of the post-nova evolutionary models and their X-ray output. Furthermore, only a moderate circumstellar absorption, with hydrogen column density of the order of $\sim 10^{21}$ cm $^{-2}$, will remove the discrepancy.

Driven by the importance of fast novae, particularly in the SN Ia progenitor context and the distribution of massive WDs in novae, we have undertaken the analysis of the iPTF data of M31 to search for these events, whose population has not been constrained to date. In the process, we have formulated a new efficient method to identify the candidates for variable sources in the outputs of the difference imaging pipelines of optical time-domain surveys. In our method, we create an image that stores the spatial and recurrence information of the raw detections from the data pipeline, through their projection onto a blank image of the analyzed field. In the resulting spatial recurrence image, the source candidates appear as clusters over a background of artifacts that approximately follow Poisson statistics, in a way similar to an X-ray image. This allows us to import various convenient tools from the X-ray domain for analyzing the spatial recurrence image. In particular, we use the popular wavelet-based tool **WAVDETECT** from the **CIAO** software package. By applying **WAVDETECT** on the spatial recurrence image, we obtain the unique candidates for variable

sources. The method is illustrated in this thesis using iPTF M31 observations obtained between September 2013 and January 2014. The iPTF pipeline made $\sim 10^5$ detections on the difference images of these observations, which are not necessarily unique sources and which are unavoidably contaminated by artifacts. Applying our method, we obtain ≈ 4000 unique candidates for variable sources from these raw detections. When cross-matching these candidates with the source-catalog of a deep reference image of the same field of M31, we obtain matches for $\sim 90\%$ of these candidates, implying the remaining 10% are candidates for transient sources like supernovae Ia. Thus, with our method the number of transient candidates is reduced by three orders of magnitude from the initial raw detections of 10^5 .

We further use the ~ 4000 candidates to conduct a systematic search for novae. We opt to use all the candidates since it cannot be ruled out that some novae may have counterparts in the reference image during their quiescence, given the depth of the reference image (≈ 23 mag). After constructing the lightcurves for these candidates, we apply selection cuts based on the expected properties of novae. We finally obtain eight nova candidates, all of which we verified to be confirmed novae.

Given the automated nature of the whole procedure, from the difference imaging to the final lightcurve selection, it becomes possible to perform a comprehensive computation of the sample completeness, which is one of the future research plans. More specifically, we will be analyzing a much larger data set of M31 from iPTF, covering two years time between 2013 and 2015, to obtain an iPTF nova sample, in particular containing fast novae. This will be followed by a detailed completeness analysis of the sample. Subsequently, we will obtain more stringent constraints on the final stage of mass accumulation by the SN Ia progenitor in the nova regime, and also derive a more accurate WD mass distribution in novae, particularly for the massive WDs. In addition, employing our method on data of other galaxies from high-cadence optical surveys, we will be able to obtain nova samples, including fast novae, for various galaxies, allowing us to make comparisons of their nova populations.

Appendix A

A quick primer of the expansion of the universe

This primer is mainly based on Sullivan (2010) and lecture notes by Prof. Eiichiro Komatsu (Max Planck Institute for Astrophysics). The evolution of the universe is governed by the energy density and pressure of its constituents, broadly matter, radiation, and Dark Energy. Parameterizing the expansion of the universe by a dimensionless scale factor $a(t)$, the following equation relates $a(t)$ to $\rho_i(t)$ and $P_i(t)$, the energy density and pressure, respectively, of the i th component of the universe,

$$\frac{\ddot{a}(t)}{a(t)} = -\frac{4\pi G}{3} \sum_i [\rho_i(t) + 3P_i(t)]. \quad (\text{A.1})$$

Here G is Newton's gravitational constant.

In cosmology, a term called the Hubble expansion rate $H(t)$ is defined, which is the relative expansion rate of the universe as given by

$$H(t) = \frac{\dot{a}(t)}{a(t)}. \quad (\text{A.2})$$

To solve for the expansion rate of universe (Eq. A.1), we need to know how the energy density and pressure of its constituents depend on time. We have from the energy conservation equation

$$\sum_i \dot{\rho}_i(t) + 3\frac{\dot{a}(t)}{a(t)} \sum_i [\rho_i(t) + P_i(t)] = 0. \quad (\text{A.3})$$

Combining Eqs. (A.1) and (A.3), we obtain the Friedmann equation

$$\left(\frac{\dot{a}(t)}{a(t)}\right)^2 \equiv H^2(t) = \frac{8\pi G}{3} \sum_i \rho_i(t) - \frac{\kappa}{a^2(t)}, \quad (\text{A.4})$$

where κ is the integration constant, which parameterizes the spatial curvature. For a flat universe, $\kappa = 0$.

The equation of state of the i th component of the universe is expressed in the simple form

$$P_i = w_i \rho_i. \quad (\text{A.5})$$

Here w is known as the equation of state parameter. w is known for matter and radiation ($w_M \ll 1$ and $w_{\text{rad}} = 1/3$, respectively). For Dark Energy, which is responsible for the cosmic acceleration, w_{DE} provides a convenient parameterization. For constant w ,

$$\rho_i \propto a(t)^{-3(1+w_i)}. \quad (\text{A.6})$$

If w_{DE} is not assumed to be constant, we have for the dark energy density

$$\rho_{\text{DE}} \propto e^{-3 \int d \ln a(1+w_{\text{DE}}(a))}. \quad (\text{A.7})$$

Using these results for the energy densities in Eq. (A.4), we have the Friedmann equation for our flat universe,

$$\left(\frac{\dot{a}(t)}{a(t)} \right)^2 \equiv H^2(t) = \frac{8\pi G}{3} \left[\rho_M(t_0) \frac{a^3(t_0)}{a^3(t)} + \rho_{\text{rad}}(t_0) \frac{a^4(t_0)}{a^4(t)} + \rho_{\text{DE}}(t_0) e^{-3 \int_{a(t_0)}^{a(t)} d \ln a(1+w_{\text{DE}}(a))} \right]. \quad (\text{A.8})$$

We express Eq. (A.8) in a more convenient form by writing the different density components in terms of the so-called density parameters, Ω , defined as

$$\Omega_i \equiv \frac{\rho_i(t_0)}{\rho_c}. \quad (\text{A.9})$$

Here $\rho_c = 3H_0/8\pi G$, known as the critical density, is the total energy density of the current flat universe. Note that $H_0 \equiv H(t_0)$. One can then write the Friedmann equation in a compact form as

$$\frac{H^2(t)}{H_0^2} = \Omega_M \frac{a^3(t_0)}{a^3(t)} + \Omega_{\text{rad}} \frac{a^4(t_0)}{a^4(t)} + \Omega_{\text{DE}} e^{-3 \int_{a(t_0)}^{a(t)} d \ln a(1+w_{\text{DE}}(a))}. \quad (\text{A.10})$$

The scale factor $a(t)$ is measured via the redshift of the object z . They are related as

$$1 + z = \frac{a(t_0)}{a(t)}. \quad (\text{A.11})$$

This allows us to write Eq. (A.10) in the most commonly used form,

$$\frac{H^2(z)}{H_0^2} = \Omega_M(1+z)^3 + \Omega_{\text{rad}}(1+z)^4 + \Omega_{\text{DE}} e^{3 \int_0^z d \ln(1+z)(1+w_{\text{DE}}(z))}. \quad (\text{A.12})$$

Appendix B

Nova light-curve template

Many important properties of the nova outbursts are encoded in the light curves, which may be, however, vastly different from one system to the other. Nevertheless, in an effort to classify these light curves on the basis of their morphology, Strope et al. (2010) have proposed seven classes of nova light curves using a large sample of 93 well-observed Galactic novae. These are the Smooth (S), Plateau (P), Dust (D), Cusp (C), Oscillation (O), Flat-topped (F) and Jitter (J) classes. The S class is the most fundamental of all since the light curve shapes characterising the rest of the classes can be derived from the smooth shape by superposing it with certain features. With 85 novae out of 93 having an unambiguous classification, the largest fraction (38 %) also falls in the S class. Moreover, more than half of the novae with $t_3 \leq 21$ days (taking this value to define the fast novae of interest) belong to this class. We have, thus, adopted the S class light curves for generating the template curve. This is further justified by noting that most of the features marking the distinction between the various classes generally develop much later in time when the light curve has declined by ~ 3 mag or more from the peak. Since we are interested in calculating the incompleteness of high cadence optical surveys with respect to detection of ‘fast’ novae by measuring the t_2 time, we shall be looking only at the decline part within 2-3 magnitudes from the peak where the light curves generally have smooth morphology. It, thus, suffices to consider the smooth class light curves only.

In order to produce the scalable template light curve, we select all sufficiently well-sampled light curves from the S class using the tabulated data from Strope et al. (2010), who have compiled them by binning and averaging the original data mostly obtained from the American Association of Variable Star Observers (AAVSO). The binning and averaging process has been done in a conservative way to retain any fine detail in the light curve while at the same time reducing the statistical uncertainty and the surplus quantity of the data. In Fig. B.1, these light curves are shown with their peaks aligned after shifting linearly along the time axis. As can be seen, they have varied extent along the time axis as well as in magnitude.

We use the following transformation to co-align the light curves:

$$m(t) \rightarrow m'(t') = \Delta m + m[(t - t_p)s], \quad (\text{B.1})$$

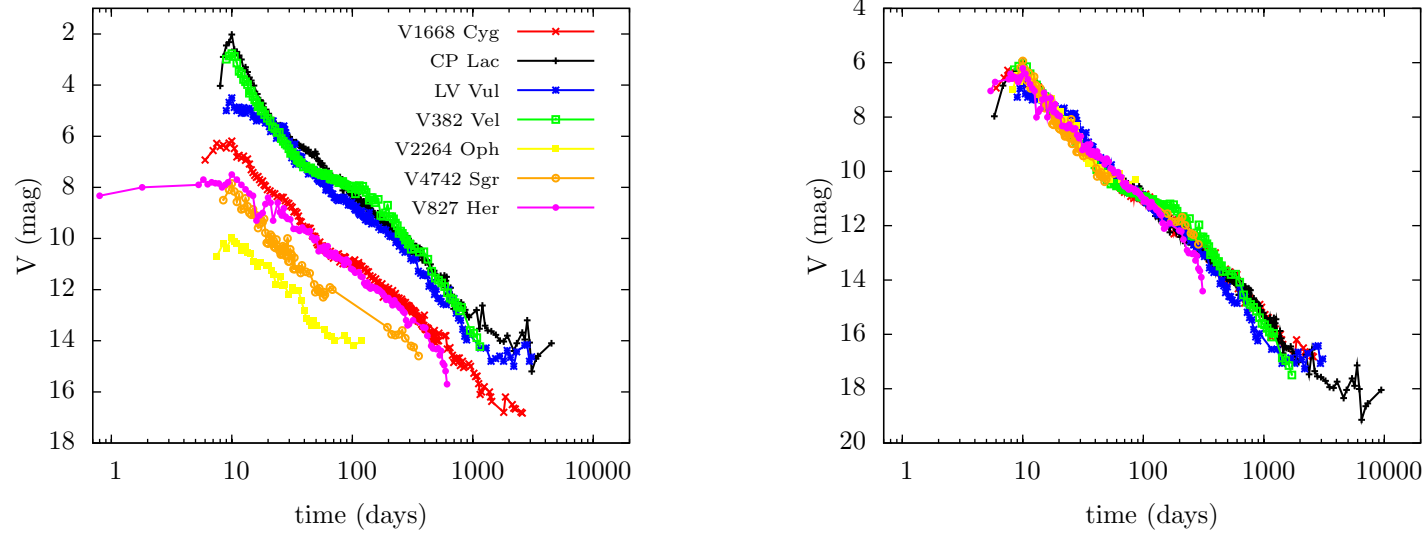


Figure B.1: Light curves of the sample selected from the S class of the catalog compiled by Strope et al. (2010) with all the peaks aligned at $t = 10$ days by a linear shift along the time axis (*left*) and the resulting transformed curves after stretching in time and shifting in magnitude with respect to the reference light curve of V1668 Cyg according to Eq. (B.1) (*right*).

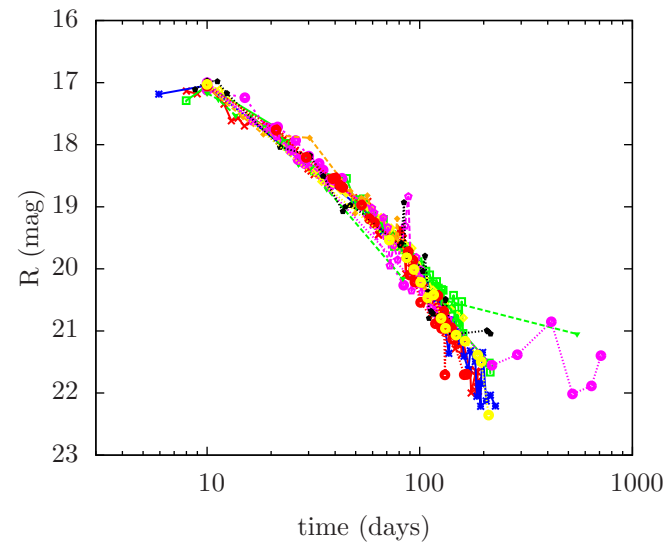
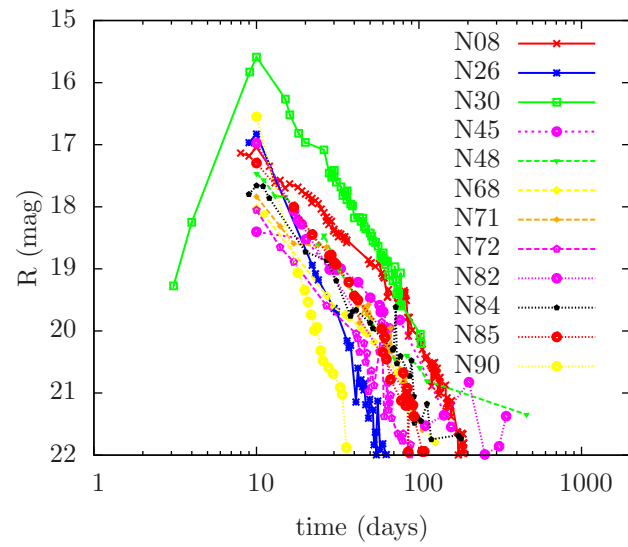


Figure B.2: Same as in Fig. B.1 but for the smooth class light curves from the WeCAPP sample. The event N08 was used as a reference.

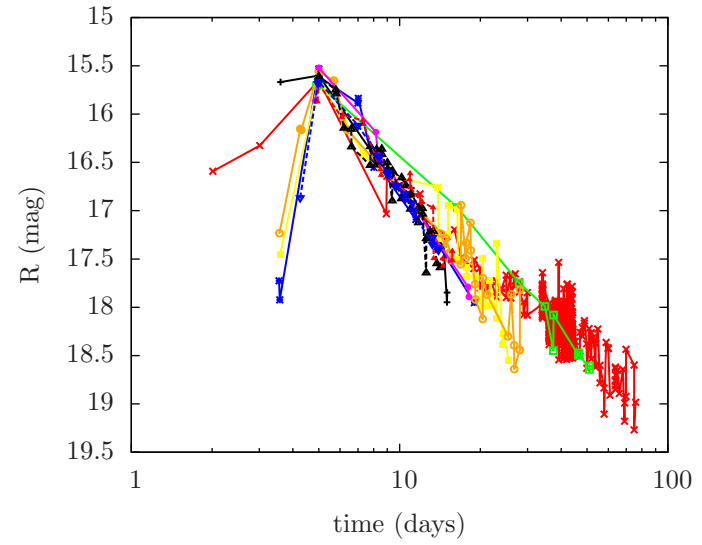
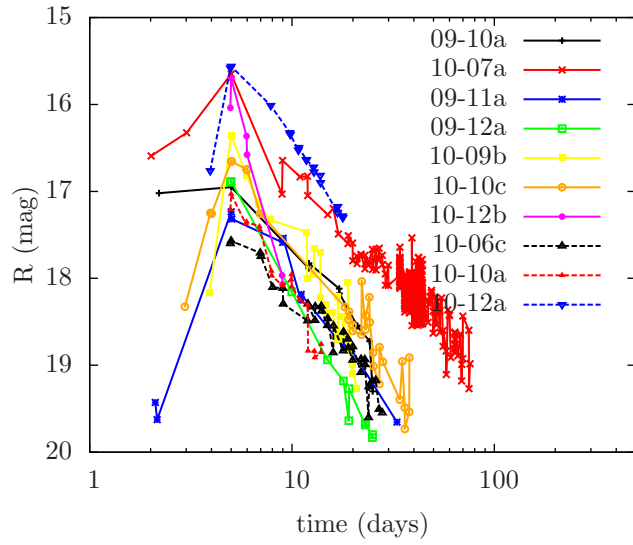


Figure B.3: Same as in Fig. B.1 but for the smooth class light curves from the PTF sample. The event 10-07a was used as a reference.

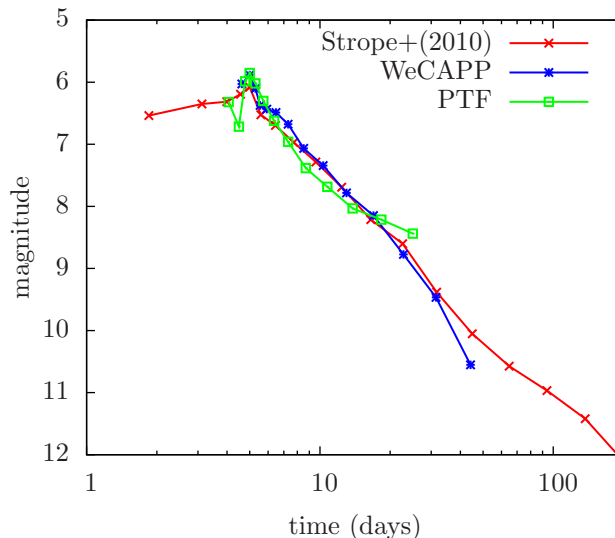


Figure B.4: Co-aligned template light curves from the three nova samples, viz., the Galactic sample from Strophe et al. (2010) and the M31 samples obtained from the WeCAPP and PTF nova catalogs.

where $m(t)$ is the magnitude in the frame t , $m'(t')$ is that in the transformed frame $t' = (t - t_p)s$, t_p is the time of the peak of the light curve, Δm the magnitude shift and s the time stretch factor.

The light curves are matched to the reference light curve, for which we have chosen V1668 Cyg. After aligning the peak of the light curve with the reference, we bin the light curves logarithmically (typically 5 bins or more per dex along time axis) and determine the magnitude in each bin by taking the average, weighted by the inverse square of the uncertainty in the individual magnitude measurement. The best fit parameters Δm and s of the transformation Eq. (B.1) are determined via minimizing the χ^2

$$\chi^2 = \sum_{i=1}^N \frac{(m'_i - m_{i,\text{ref}})^2}{\sigma_i^2 + \sigma_{i,\text{ref}}^2}, \quad (\text{B.2})$$

where N is the total number of bins in which both light curves have measurements, $m_{i,\text{ref}}$ is the magnitude of the reference curve and m'_i , that of the other curve after the transformation in the i -th bin, with corresponding uncertainties $\sigma_{i,\text{ref}}$ and σ_i . The result of this procedure is shown in the right panel in Fig. B.1. In all cases we are able to obtain a reasonably good agreement, with the values of the stretch factor ranging from ≈ 0.5 – 2 and the rms dispersion between the reference and individual light curves calculated down to 6 mag from the peak being in the range 0.18–0.33 mag. Finally, we average the resulting transformed curves by binning in time (logarithmically again) and weighting by the respective uncertainties to produce the template curve.

This template light curve is generated using a Galactic nova sample. Although we do not expect any significant difference from the M31 novae, for a consistency check we

compare our template with light curves from two different M31 nova samples. We apply the procedure described above to the selection of well-sampled light curves from the nova catalog of the WeCAPP (Riffeser et al. 2001), which have been classified as having smooth morphology (Lee et al. 2012), and to light curves from the PTF M31 survey in Cao et al. (2012). In these two cases, we are also able to obtain good light curve matches, with the rms dispersion (calculated down to 4 mag from peak) lower than ≈ 0.30 mag. Final template curves are generated using the same procedure as before. The resulting templates are shown in Fig. B.4 along with our default template based on Strobe et al. (2010) data. The plot shows that all three templates agree very well with each other. For our calculations, we use the template obtained based on the Strobe et al. (2010) data because it is the best sampled and covers the broadest magnitude range.

Appendix C

Peak magnitudes of novae

In this appendix, we produce an analog of the MMRD relation, with the goal of assigning appropriate peak magnitude for each simulated nova (Sects. 2.4, 3.3) Various forms of this relation have been obtained previously (for example, see della Valle & Livio 1995; Downes & Duerbeck 2000; Darnley et al. 2006; Shafter et al. 2011), although recently its existence has been questioned (Kasliwal et al. 2011). However, for the purpose of the study undertaken in this thesis, we are not concerned with the existence of the MMRD relation, instead we need to account for the full range of observed nova peak magnitudes in our simulations. We therefore collected a large sample of novae and determined their mean magnitudes and rms scatter in broad bins over t_2 as explained below.

We used the light curves from the PTF (Cao et al. 2012) and WeCAPP (Lee et al. 2012) nova catalogs with morphological classification available, the light curves from Shafter et al. (2011) that have been observed in the V band, the high-quality light curves from Capaccioli et al. (1989), and the sample of extragalactic novae discovered by P60-FasTING (Kasliwal et al. 2011). To this compilation, we added the recently discovered very fast recurrent nova M31N 2008-12a in M31 with the shortest known recurrence period of ~ 1 year (Shafter et al. 2012; Darnley et al. 2014; Henze et al. 2014a; Tang et al. 2014a). The PTF and WeCAPP light curves were converted from R band to V band using the color $(V - R)_\circ = 0.16$ (Shafter et al. 2009) after accounting for the foreground extinction of $A_R = 0.15$ (Shafter et al. 2009) estimated using a reddening of $E(B - V) = 0.062$ along the line of sight to M31 from Schlegel et al. (1998). The light curves from Capaccioli et al. (1989) were corrected for foreground extinction using $A_{pg} = 0.25$ (Shafter et al. 2009) and converted from the photographic band to V band using the colors $(B - m_{pg})_\circ = 0.17$ (Capaccioli et al. 1989; Arp 1956) and $(B - V)_\circ = 0.15$ (Shafter et al. 2009). The Kasliwal et al. (2011) light curves were converted from g band to V band using the transformation relation from Jordi et al. (2006). Apparent magnitudes were converted to absolute magnitudes using a distance modulus of 24.36 for M31 (Vilardell et al. 2010). Light curves from Shafter et al. (2011) were corrected for extinction and converted to absolute magnitude in the original publication. Except for the WeCAPP sample, we used the light-curve decline times (t_2) from the respective publications. For those novae in Kasliwal et al. (2011) whose t_2 times are not available, we approximated them by multiplying the decline times t_1 in their Table 5

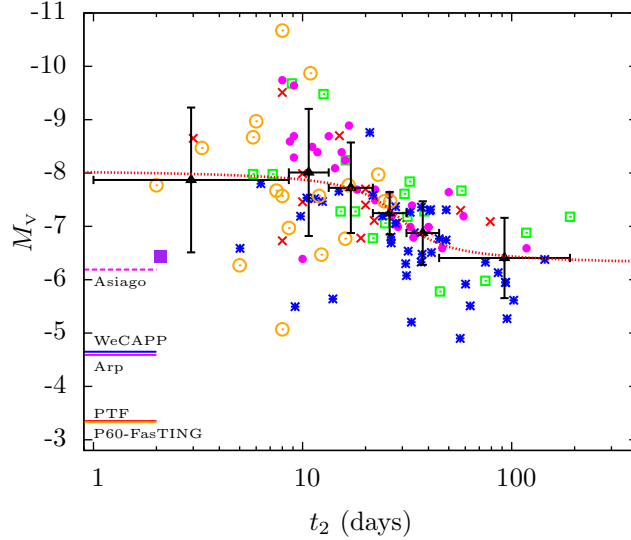


Figure C.1: Relation between the maximum magnitude and the rate of decline for extragalactic novae. The PTF data are shown by red x symbols, WeCAPP – blue stars, Shafter et al. (2011) data – green squares, Capaccioli et al. (1989) data – magenta filled circles, Kasliwal et al. (2011) data – orange open circles, and the purple square is the recurrent nova M31N 2008-12a in M31. The black triangles represent the averages in the bins, and the red dotted line is our fit. The line segments on the left side mark the approximate limiting magnitudes of the surveys (as shown by the legend).

by two. For the WeCAPP light curves we estimated their decline times ourselves by linearly interpolating between consecutive measurements.

The collected data are shown in Fig. C.1. To quantify the data in a statistical manner, we grouped them according to the decline times, with the bin-width adjusted to have equal number (19) of novae in each bin. For each bin, we computed the mean magnitude and its standard deviation. The values obtained are listed in Table C.1. We then fit the binned data with the functional form of the MMRD relation from della Valle & Livio (1995) to generate the analytical MMRD relation (Fig. C.1):

$$M_V = -7.17 - 0.58 \arctan\left(\frac{1.46 - \log t_2}{0.17}\right) \quad (\text{C.1})$$

As one can see from Fig. C.1, the MMRD relation is subject to significant scatter. This is taken into account in our incompleteness simulations (Sects. 2.4, 3.3). To this end, we use the observed dispersion in each MMRD bin (Table C.1), assigning the measured values to the bin centers, to perform linear interpolation to compute the dispersion in peak magnitude for a given value of the decline time. For decline times smaller than the decline time in the first bin or greater than the decline time in the last bin, we adopt the same standard deviation as that in the first and last bin, respectively.

As a final word of caution, the data used in computing Table C.1 are collected from a heterogeneous set of magnitude limited surveys. Therefore, our results should not be inter-

Table C.1: Mean nova peak magnitudes and their standard deviations

t_2 range (days)	$\langle M_V \rangle$ (mag)	σ (mag)
< 8.60	-7.87	1.36
$8.60 - 13.33$	-8.01	1.19
$13.33 - 21.70$	-7.72	0.85
$21.70 - 31.41$	-7.25	0.40
$31.41 - 44.98$	-6.88	0.59
> 44.98	-6.41	0.75

puted as an attempt to produce an updated version of the MMRD relation. Incompleteness of individual surveys could bias our calculations of mean magnitudes, shifting them upward. However, the magnitude limits of the majority of the surveys used here are deep enough (Fig. C.1), therefore our results should not be dramatically affected by such incompleteness.

To produce a light curve with a given t_2 time and corresponding peak magnitude, the template light curve generated in Sect. B is transformed using Eq. (B.1), with the time stretch factor and magnitude shift given by

$$s = t_2/t_{2,\text{temp}} \quad (\text{C.2})$$

and

$$\Delta m = m_p - m_{p,\text{temp}}. \quad (\text{C.3})$$

Here t_2 and $t_{2,\text{temp}}$ denote the decline time of the simulated nova and of the template, respectively, while m_p and $m_{p,\text{temp}}$ are the corresponding peak magnitudes. We interpolate the template light curve linearly between the consecutive data points in magnitude – log(time) space.

Bibliography

- Alard, C., Image subtraction using a space-varying kernel, *A&AS* **144** (Jun. 2000) 363–370
- Alard, C. & Lupton, R. H., A Method for Optimal Image Subtraction, *ApJ* **503** (Aug. 1998) 325–331, [astro-ph/9712287](#)
- Arp, H. C., Novae in the Andromeda nebula., *AJ* **61** (Feb. 1956) 15–34
- Barmby, P., Ashby, M. L. N., Bianchi, L., et al., Dusty Waves on a Starry Sea: The Mid-Infrared View of M31, *ApJ* **650** (Oct. 2006) L45–L49, [astro-ph/0608593](#)
- Barmby, P., Ashby, M. L. N., Bianchi, L., et al., Erratum: “Dusty Waves on a Starry Sea: The Mid-Infrared View of M31”, *ApJ* **655** (Jan. 2007) L61–L61
- Bath, G. T. & Shaviv, G., Classical novae - a steady state, constant luminosity, continuous ejection model., *MNRAS* **175** (May 1976) 305–322
- Battaner, E., Beckman, J. E., Mediavilla, E., et al., Near-infrared mapping of spiral galaxies. II - J, H, K profiles of M 31, *A&A* **161** (Jun. 1986) 70–74, ADS
- Bell, E. F. & de Jong, R. S., Stellar Mass-to-Light Ratios and the Tully-Fisher Relation, *ApJ* **550** (Mar. 2001) 212–229, [astro-ph/0011493](#)
- Bertin, E. & Arnouts, S., SExtractor: Software for source extraction., *A&AS* **117** (Jun. 1996) 393–404
- Bildsten, L., Shen, K. J., Weinberg, N. N., & Nelemans, G., Faint Thermonuclear Supernovae from AM Canum Venaticorum Binaries, *ApJ* **662** (Jun. 2007) L95–L98, [astro-ph/0703578](#)
- Blanton, M. R. & Roweis, S., K-Corrections and Filter Transformations in the Ultraviolet, Optical, and Near-Infrared, *AJ* **133** (Feb. 2007) 734–754, [astro-ph/0606170](#)
- Bloom, J. S., Richards, J. W., Nugent, P. E., et al., Automating Discovery and Classification of Transients and Variable Stars in the Synoptic Survey Era, *PASP* **124** (Nov. 2012) 1175–1196, [arXiv:1106.5491](#) [[astro-ph.IM](#)]
- Bode, M. F. & Evans, A. 2008, *Classical Novae*, 2nd Edition. Edited by M.F. Bode and A. Evans, Cambridge Astrophysics Series, No. 43, Cambridge University Press, UK

- Bogdán, Á. & Gilfanov, M., Unresolved X-ray emission in M31 and constraints on progenitors of classical novae, *MNRAS* **405** (Jun. 2010) 209–218, [arXiv:1002.3353](#) [[astro-ph.GA](#)]
- Brinks, E. & Shane, W. W., A high resolution hydrogen line survey of Messier 31. I Observations and data reduction, *A&AS* **55** (Feb. 1984) 179–251, [ADS](#)
- Brown, T. M., Smith, E., Ferguson, H. C., et al., The Detailed Star Formation History in the Spheroid, Outer Disk, and Tidal Stream of the Andromeda Galaxy, *ApJ* **652** (Nov. 2006) 323–353, [astro-ph/0607637](#)
- Cao, Y., Kasliwal, M. M., Neill, J. D., et al., Classical Novae in Andromeda: Light Curves from the Palomar Transient Factory and GALEX, *ApJ* **752** (Jun. 2012) 133, [arXiv:1201.2393](#) [[astro-ph.SR](#)]
- Capaccioli, M., della Valle, M., Rosino, L., & D’Onofrio, M., Properties of the nova population in M31, *AJ* **97** (Jun. 1989) 1622–1633
- Cassisi, S., Iben, Jr., I., & Tornambe, A., Hydrogen-accreting Carbon-Oxygen White Dwarfs, *ApJ* **496** (Mar. 1998) 376
- Chen, H.-L., Woods, T. E., Yungelson, L. R., Gilfanov, M., & Han, Z., Next generation population synthesis of accreting white dwarfs - I. Hybrid calculations using BSE+MESA, *MNRAS* **445** (Dec. 2014) 1912–1923, [arXiv:1404.4450](#) [[astro-ph.SR](#)]
- Churazov, E., Sunyaev, R., Isern, J., et al., Cobalt-56 γ -ray emission lines from the type Ia supernova 2014J, *Nature* **512** (Aug. 2014) 406–408, [arXiv:1405.3332](#) [[astro-ph.HE](#)]
- Colgate, S. A. & McKee, C., Early Supernova Luminosity, *ApJ* **157** (Aug. 1969) 623
- Darnley, M. J., Bode, M. F., Kerins, E., et al., Classical novae from the POINT-AGAPE microlensing survey of M31 - II. Rate and statistical characteristics of the nova population, *MNRAS* **369** (Jun. 2006) 257–271, [astro-ph/0509493](#)
- Darnley, M. J., Bode, M. F., Kerins, E., et al., Classical novae from the POINT-AGAPE microlensing survey of M31 - I. The nova catalogue, *MNRAS* **353** (Sep. 2004) 571–588, [astro-ph/0403447](#)
- Darnley, M. J., Williams, S. C., Bode, M. F., et al., A remarkable recurrent nova in M 31: The optical observations, *A&A* **563** (Mar. 2014) L9, [arXiv:1401.2905](#) [[astro-ph.SR](#)]
- Davé, R., Oppenheimer, B. D., & Finlator, K., Galaxy evolution in cosmological simulations with outflows - I. Stellar masses and star formation rates, *MNRAS* **415** (Jul. 2011) 11–31, [arXiv:1103.3528](#)

- de Vaucouleurs, G., de Vaucouleurs, A., Corwin, Jr., H. G., et al. 1991, Third Reference Catalogue of Bright Galaxies. Volume I: Explanations and references. Volume II: Data for galaxies between 0^h and 12^h . Volume III: Data for galaxies between 12^h and 24^h ., Springer, New York, NY, USA
- della Valle, M. & Livio, M., The Calibration of Novae as Distance Indicators, *ApJ* **452** (Oct. 1995) 704
- Denissenkov, P. A., Herwig, F., Bildsten, L., & Paxton, B., MESA Models of Classical Nova Outbursts: The Multicycle Evolution and Effects of Convective Boundary Mixing, *ApJ* **762** (Jan. 2013) 8, [arXiv:1210.5209](#) [[astro-ph.SR](#)]
- Devereux, N. A., Price, R., Wells, L. A., & Duric, N., Two views of the Andromeda Galaxy H-alpha and far infrared, *AJ* **108** (Nov. 1994) 1667–1673
- Downes, R. A. & Duerbeck, H. W., Optical Imaging of Nova Shells and the Maximum Magnitude-Rate of Decline Relationship, *AJ* **120** (Oct. 2000) 2007–2037, [astro-ph/0006458](#)
- Fabrika, S., Barsukova, E. A., Valeev, A. F., et al., Spectroscopy and photometry of the nova M31N 2014-01a at maximum, *The Astronomer’s Telegram* **5754** (Jan. 2014), [ADS](#)
- Fink, M., Röpke, F. K., Hillebrandt, W., et al., Double-detonation sub-Chandrasekhar supernovae: can minimum helium shell masses detonate the core?, *A&A* **514** (May 2010) A53, [arXiv:1002.2173](#) [[astro-ph.SR](#)]
- Fossey, S. J., Cooke, B., Pollack, G., Wilde, M., & Wright, T., Supernova 2014J in M82 = Psn J09554214+6940260, *Central Bureau Electronic Telegrams* **3792** (Jan. 2014), [ADS](#)
- Freeman, P. E., Kashyap, V., Rosner, R., & Lamb, D. Q., A Wavelet-Based Algorithm for the Spatial Analysis of Poisson Data, *ApJS* **138** (Jan. 2002) 185–218, [astro-ph/0108429](#)
- Fruscione, A., McDowell, J. C., Allen, G. E., et al., CIAO: Chandra’s data analysis system, in *Society of Photo-Optical Instrumentation Engineers (SPIE) Conference Series*, Vol. 6270, Society of Photo-Optical Instrumentation Engineers (SPIE) Conference Series. 2006, 62701V
- Fujimoto, M. Y., A Theory of Hydrogen Shell Flashes on Accreting White Dwarfs - Part Two - the Stable Shell Burning and the Recurrence Period of Shell Flashes, *ApJ* **257** (Jun. 1982) 767
- Gänsicke, B. T., Dillon, M., Southworth, J., et al., SDSS unveils a population of intrinsically faint cataclysmic variables at the minimum orbital period, *MNRAS* **397** (Aug. 2009) 2170–2188, [arXiv:0905.3476](#) [[astro-ph.SR](#)]
- Gehrz, R. D., Truran, J. W., Williams, R. E., & Starrfield, S., Nucleosynthesis in Classical Novae and Its Contribution to the Interstellar Medium, *PASP* **110** (Jan. 1998) 3–26

- Gil-Pons, P., García-Berro, E., José, J., Hernanz, M., & Truran, J. W., The frequency of occurrence of novae hosting an ONe white dwarf, *A&A* **407** (Sep. 2003) 1021–1028, [astro-ph/0306197](#)
- Gilfanov, M. & Bogdán, Á., An upper limit on the contribution of accreting white dwarfs to the type Ia supernova rate, *Nature* **463** (Feb. 2010) 924–925, [arXiv:1002.3359](#) [[astro-ph.CO](#)]
- Gilfanov, M. & Bogdán, Á., Progenitors of type Ia supernovae in elliptical galaxies, in *American Institute of Physics Conference Series*, Vol. 1379, American Institute of Physics Conference Series, ed. E. Göğüş, T. Belloni, & Ü. Ertan. 2011, 17–22, [arXiv:1103.3659](#) [[astro-ph.HE](#)]
- Glasner, S. A., Livne, E., & Truran, J. W., Convective overshoot mixing in Nova outbursts - the dependence on the composition of the underlying white dwarf, *MNRAS* **427** (Dec. 2012) 2411–2419
- Hachisu, I. & Kato, M., Recurrent Novae as a Progenitor System of Type Ia Supernovae. I. RS Ophiuchi Subclass: Systems with a Red Giant Companion, *ApJ* **558** (Sep. 2001) 323–350, [astro-ph/0104040](#)
- Hachisu, I., Kato, M., & Nomoto, K., A New Model for Progenitor Systems of Type IA Supernovae, *ApJ* **470** (Oct. 1996) L97
- Helder, E. A., Vink, J., Bassa, C. G., et al., Measuring the Cosmic-Ray Acceleration Efficiency of a Supernova Remnant, *Science* **325** (Aug. 2009) 719, [arXiv:0906.4553](#) [[astro-ph.GA](#)]
- Henze, M., Ness, J.-U., Darnley, M. J., et al., A remarkable recurrent nova in M 31: The X-ray observations, *A&A* **563** (Mar. 2014) L8, [arXiv:1401.2904](#) [[astro-ph.HE](#)]
- Henze, M., Ness, J.-U., Darnley, M. J., et al., A remarkable recurrent nova in M 31: The predicted 2014 outburst in X-rays with Swift, *ArXiv e-prints* (Apr. 2015), [arXiv:1504.06237](#) [[astro-ph.HE](#)]
- Henze, M., Pietsch, W., Haberl, F., et al., Supersoft X-rays reveal a classical nova in the M 31 globular cluster Bol 126, *A&A* **549** (Jan. 2013) A120, [arXiv:1211.4736](#) [[astro-ph.HE](#)]
- Henze, M., Pietsch, W., Haberl, F., et al., X-ray monitoring of classical novae in the central region of M 31 III. Autumn and winter 2009/10, 2010/11, and 2011/12, *A&A* **563** (Mar. 2014) A2, [arXiv:1312.1241](#) [[astro-ph.HE](#)]
- Henze, M., Pietsch, W., Haberl, F., et al., X-ray monitoring of classical novae in the central region of M 31. I. June 2006–March 2007, *A&A* **523** (Nov. 2010) A89, [arXiv:1009.1644](#) [[astro-ph.HE](#)]

- Henze, M., Pietsch, W., Haberl, F., et al., X-ray monitoring of classical novae in the central region of M 31. II. Autumn and winter 2007/2008 and 2008/2009, *A&A* **533** (Sep. 2011) A52, [arXiv:1010.1461](#) [[astro-ph.HE](#)]
- Hillman, Y., Prialnik, D., Kovetz, A., & Shara, M. M., Observational signatures of SNIa progenitors, as predicted by models, *MNRAS* **446** (Jan. 2015) 1924–1930, [arXiv:1411.0382](#) [[astro-ph.SR](#)]
- Hornoch, K. & Kucakova, H., Discovery of an Apparent Nova in M31, *The Astronomer's Telegram* **5671** (Dec. 2013), [ADS](#)
- Hornoch, K. & Kucakova, H., Discovery of an Apparent Nova in M31, *The Astronomer's Telegram* **5815** (Jan. 2014), [ADS](#)
- Hornoch, K., Manilla-Robles, A., Tudor, V., Vaduvescu, O., & Ramsay, G., H-alpha Confirmation of Six Novae in M31, *The Astronomer's Telegram* **5503** (Oct. 2013), [ADS](#)
- Hornoch, K. & Vrstil, J., Discovery of a Probable Nova in M31, *The Astronomer's Telegram* **5450** (Oct. 2013), [ADS](#)
- Howell, D. A., Type Ia supernovae as stellar endpoints and cosmological tools, *Nature Communications* **2** (Jun. 2011), [arXiv:1011.0441](#) [[astro-ph.CO](#)]
- Howell, D. A., Sullivan, M., Nugent, P. E., et al., The type Ia supernova SNLS-03D3bb from a super-Chandrasekhar-mass white dwarf star, *Nature* **443** (Sep. 2006) 308–311, [astro-ph/0609616](#)
- Howell, S. B. 2006, *Handbook of CCD Astronomy*, Cambridge observing handbooks for research astronomers, Vol. 5, Cambridge University Press, UK
- Hoyle, F. & Fowler, W. A., Nucleosynthesis in Supernovae., *ApJ* **132** (Nov. 1960) 565
- Hubble, E. P., A spiral nebula as a stellar system, Messier 31., *ApJ* **69** (Mar. 1929) 103–158
- Iben, Jr., I. & Renzini, A., Asymptotic giant branch evolution and beyond, *ARA&A* **21** (1983) 271–342
- Iben, Jr., I. & Tutukov, A. V., Supernovae of type I as end products of the evolution of binaries with components of moderate initial mass (M not greater than about 9 solar masses), *ApJS* **54** (Feb. 1984) 335–372
- Iben, Jr., I. & Tutukov, A. V., The evolution of low-mass close binaries influenced by the radiation of gravitational waves and by a magnetic stellar wind, *ApJ* **284** (Sep. 1984) 719–744
- Idan, I., Shaviv, N. J., & Shaviv, G., The fate of a WD accreting H-rich material at high accretion rates, *MNRAS* **433** (Aug. 2013) 2884–2892

- Iwamoto, K., Brachwitz, F., Nomoto, K., et al., Nucleosynthesis in Chandrasekhar Mass Models for Type IA Supernovae and Constraints on Progenitor Systems and Burning-Front Propagation, *ApJS* **125** (Dec. 1999) 439–462, [astro-ph/0002337](#)
- Johansson, J., Woods, T. E., Gilfanov, M., et al., Diffuse gas in galaxies sheds new light on the origin of Type Ia supernovae, *MNRAS* **442** (Aug. 2014) 1079–1089, [arXiv:1401.1344](#)
- Jordi, K., Grebel, E. K., & Ammon, K., Empirical color transformations between SDSS photometry and other photometric systems, *A&A* **460** (Dec. 2006) 339–347, [astro-ph/0609121](#)
- José, J. & Hernanz, M., Nucleosynthesis in Classical Novae: CO versus ONe White Dwarfs, *ApJ* **494** (Feb. 1998) 680–690, [astro-ph/9709153](#)
- Kahabka, P., Hartmann, H. W., Parmar, A. N., & Negueruela, I., Luminous supersoft X-ray emission from the recurrent nova U Scorpii, *A&A* **347** (Jul. 1999) L43–L46, ADS
- Kahabka, P. & van den Heuvel, E. P. J., Luminous Supersoft X-Ray Sources, *ARA&A* **35** (1997) 69–100
- Kamiya, Y., Tanaka, M., Nomoto, K., et al., Super-Chandrasekhar-mass Light Curve Models for the Highly Luminous Type Ia Supernova 2009dc, *ApJ* **756** (Sep. 2012) 191, [arXiv:1207.4648](#) [[astro-ph.HE](#)]
- Kashi, A. & Soker, N., A circumbinary disc in the final stages of common envelope and the core-degenerate scenario for Type Ia supernovae, *MNRAS* **417** (Oct. 2011) 1466–1479, [arXiv:1105.5698](#) [[astro-ph.SR](#)]
- Kasliwal, M. M., Cenko, S. B., Kulkarni, S. R., et al., Discovery of a New Photometric Sub-class of Faint and Fast Classical Novae, *ApJ* **735** (Jul. 2011) 94, [arXiv:1003.1720](#) [[astro-ph.SR](#)]
- Kato, M. & Hachisu, I., Optically thick winds in nova outbursts, *ApJ* **437** (Dec. 1994) 802–826
- Kato, M., Saio, H., Hachisu, I., & Nomoto, K., Shortest Recurrence Periods of Novae, *ArXiv e-prints* (Apr. 2014), [arXiv:1404.0582](#) [[astro-ph.SR](#)]
- Kerins, E., Darnley, M. J., Duke, J. P., et al., Difference image photometry with bright variable backgrounds, *MNRAS* **409** (Nov. 2010) 247–258, [arXiv:1004.2166](#)
- Knigge, C., The Evolution of Cataclysmic Variables, in *Astronomical Society of the Pacific Conference Series*, Vol. 447, *Evolution of Compact Binaries*, ed. L. Schmidtobreick, M. R. Schreiber, & C. Tappert. 2011, 3, [arXiv:1108.4716](#) [[astro-ph.SR](#)]

- Knigge, C., Baraffe, I., & Patterson, J., The Evolution of Cataclysmic Variables as Revealed by Their Donor Stars, *ApJS* **194** (Jun. 2011) 28, [arXiv:1102.2440](#) [[astro-ph.SR](#)]
- Kowal, C. T., Absolute magnitudes of supernovae., *AJ* **73** (Dec. 1968) 1021–1024
- Krautter, J., X-ray Observations of Novae, in American Institute of Physics Conference Series, Vol. 637, Classical Nova Explosions, ed. M. Hernanz & J. José. 2002, 345–354
- Kromer, M., Sim, S. A., Fink, M., et al., Double-detonation Sub-Chandrasekhar Supernovae: Synthetic Observables for Minimum Helium Shell Mass Models, *ApJ* **719** (Aug. 2010) 1067–1082, [arXiv:1006.4489](#) [[astro-ph.HE](#)]
- Laher, R. R., Surace, J., Grillmair, C. J., et al., IPAC Image Processing and Data Archiving for the Palomar Transient Factory, *PASP* **126** (Jul. 2014) 674–710, [arXiv:1404.1953](#) [[astro-ph.IM](#)]
- Law, N. M., Kulkarni, S. R., Dekany, R. G., et al., The Palomar Transient Factory: System Overview, Performance, and First Results, *PASP* **121** (Dec. 2009) 1395–1408, [arXiv:0906.5350](#) [[astro-ph.IM](#)]
- Lee, C.-H., Riffeser, A., Seitz, S., et al., The Wendelstein Calar Alto Pixellensing Project (WeCAPP): the M 31 nova catalogue, *A&A* **537** (Jan. 2012) A43, [arXiv:1109.6573](#) [[astro-ph.GA](#)]
- Li, W., Chornock, R., Leaman, J., et al., Nearby supernova rates from the Lick Observatory Supernova Search - III. The rate-size relation, and the rates as a function of galaxy Hubble type and colour, *MNRAS* **412** (Apr. 2011) 1473–1507, [arXiv:1006.4613](#) [[astro-ph.SR](#)]
- Liu, W.-M., Chen, W.-C., Wang, B., & Han, Z. W., Helium-star evolutionary channel to super-Chandrasekhar mass type Ia supernovae, *A&A* **523** (Nov. 2010) A3, [arXiv:1007.4751](#) [[astro-ph.HE](#)]
- Lorén-Aguilar, P., Isern, J., & García-Berro, E., High-resolution smoothed particle hydrodynamics simulations of the merger of binary white dwarfs, *A&A* **500** (Jun. 2009) 1193–1205
- MacDonald, J., The effect of a binary companion on a nova outburst, *MNRAS* **191** (Jun. 1980) 933–949
- Mannucci, F., Della Valle, M., Panagia, N., et al., The supernova rate per unit mass, *A&A* **433** (Apr. 2005) 807–814, [astro-ph/0411450](#)
- Maoz, D. & Mannucci, F., Type-Ia Supernova Rates and the Progenitor Problem: A Review, *PASA* **29** (Jan. 2012) 447–465, [arXiv:1111.4492](#) [[astro-ph.CO](#)]

- Maoz, D., Mannucci, F., & Nelemans, G., Observational Clues to the Progenitors of Type Ia Supernovae, *ARA&A* **52** (Aug. 2014) 107–170, [arXiv:1312.0628](#)
- Mazzali, P. A., Röpke, F. K., Benetti, S., & Hillebrandt, W., A Common Explosion Mechanism for Type Ia Supernovae, *Science* **315** (Feb. 2007) 825, [astro-ph/0702351](#)
- Mighell, K. J., Algorithms for CCD Stellar Photometry, in *Astronomical Society of the Pacific Conference Series*, Vol. 172, *Astronomical Data Analysis Software and Systems VIII*, ed. D. M. Mehringer, R. L. Plante, & D. A. Roberts. 1999, 317, ADS
- Mikolajewska, J., Symbiotic Novae, *ArXiv e-prints* (Nov. 2010), [arXiv:1011.5657](#) [[astro-ph.SR](#)]
- Milne, P. A., Foley, R. J., Brown, P. J., & Narayan, G., The Changing Fractions of Type Ia Supernova NUV–Optical Subclasses with Redshift, *ApJ* **803** (Apr. 2015) 20, [arXiv:1408.1706](#)
- Nariai, K., Nomoto, K., & Sugimoto, D., Nova Explosion of Mass-Accreting White Dwarfs, *PASJ* **32** (1980) 473, ADS
- Ness, J.-U., Observational evidence for expansion in the SSS spectra of novae, *Astronomische Nachrichten* **331** (Feb. 2010) 179–182, [arXiv:0908.4549](#) [[astro-ph.HE](#)]
- Ness, J.-U., Osborne, J. P., Henze, M., et al., Obscuration effects in super-soft-source X-ray spectra, *A&A* **559** (Nov. 2013) A50, [arXiv:1309.2604](#) [[astro-ph.GA](#)]
- Nieten, C., Neiningner, N., Guélin, M., et al., Molecular gas in the Andromeda galaxy, *A&A* **453** (Jul. 2006) 459–475, [astro-ph/0512563](#)
- Nomoto, K., Accreting white dwarf models for type I supernovae. I - Presupernova evolution and triggering mechanisms, *ApJ* **253** (Feb. 1982) 798–810
- Nomoto, K., Saio, H., Kato, M., & Hachisu, I., Thermal Stability of White Dwarfs Accreting Hydrogen-rich Matter and Progenitors of Type Ia Supernovae, *ApJ* **663** (Jul. 2007) 1269–1276, [astro-ph/0603351](#)
- Ofek, E. O., Laher, R., Law, N., et al., The Palomar Transient Factory Photometric Calibration, *PASP* **124** (Jan. 2012) 62–73, [arXiv:1112.4851](#) [[astro-ph.IM](#)]
- Olsen, K. A. G., Blum, R. D., Stephens, A. W., et al., The Star Formation Histories of the Bulge and Disk of M31 from Resolved Stars in the Near-Infrared, *AJ* **132** (Jul. 2006) 271–289, [astro-ph/0603793](#)
- Page, K. L., Osborne, J. P., Evans, P. A., et al., Swift observations of the X-ray and UV evolution of V2491 Cyg (Nova Cyg 2008 No. 2), *MNRAS* **401** (Jan. 2010) 121–130, [arXiv:0909.1501](#) [[astro-ph.HE](#)]

- Pagnotta, A. & Schaefer, B. E., Identifying and Quantifying Recurrent Novae Masquerading as Classical Novae, *ApJ* **788** (Jun. 2014) 164, [arXiv:1405.0246](#) [[astro-ph.SR](#)]
- Pakmor, R., Kromer, M., Taubenberger, S., et al., Normal Type Ia Supernovae from Violent Mergers of White Dwarf Binaries, *ApJ* **747** (Mar. 2012) L10, [arXiv:1201.5123](#) [[astro-ph.HE](#)]
- Patat, F., Chugai, N. N., Podsiadlowski, P., et al., Connecting RS Ophiuchi to [some] type Ia supernovae, *A&A* **530** (Jun. 2011) A63, [arXiv:1104.0506](#) [[astro-ph.SR](#)]
- Paxton, B., Bildsten, L., Dotter, A., et al., Modules for Experiments in Stellar Astrophysics (MESA), *ApJS* **192** (Jan. 2011) 3, [arXiv:1009.1622](#) [[astro-ph.SR](#)]
- Paxton, B., Cantiello, M., Arras, P., et al., Modules for Experiments in Stellar Astrophysics (MESA): Planets, Oscillations, Rotation, and Massive Stars, *ApJS* **208** (Sep. 2013) 4, [arXiv:1301.0319](#) [[astro-ph.SR](#)]
- Perlmutter, S., Aldering, G., Goldhaber, G., et al., Measurements of Omega and Lambda from 42 High-Redshift Supernovae, *ApJ* **517** (Jun. 1999) 565–586, [astro-ph/9812133](#)
- Phillips, M. M., The absolute magnitudes of Type IA supernovae, *ApJ* **413** (Aug. 1993) L105–L108
- Pietsch, W., Fliri, J., Freyberg, M. J., et al., Optical novae: the major class of supersoft X-ray sources in M 31, *A&A* **442** (Nov. 2005) 879–894, [astro-ph/0504321](#)
- Pietsch, W., Haberl, F., Sala, G., et al., X-ray monitoring of optical novae in M 31 from July 2004 to February 2005, *A&A* **465** (Apr. 2007) 375–392, [astro-ph/0612596](#)
- Prialnik, D., The evolution of a classical nova model through a complete cycle, *ApJ* **310** (Nov. 1986) 222–237
- Prialnik, D. 2000, *An Introduction to the Theory of Stellar Structure and Evolution*, Cambridge University Press, UK
- Prialnik, D. & Kovetz, A., An extended grid of multicycle nova evolution models, *ApJ* **445** (Jun. 1995) 789–810
- Rau, A., Kulkarni, S. R., Law, N. M., et al., Exploring the Optical Transient Sky with the Palomar Transient Factory, *PASP* **121** (Dec. 2009) 1334–1351, [arXiv:0906.5355](#) [[astro-ph.CO](#)]
- Rauch, T., Orio, M., Gonzales-Riestra, R., et al., Non-local Thermal Equilibrium Model Atmospheres for the Hottest White Dwarfs: Spectral Analysis of the Compact Component in Nova V4743 Sgr, *ApJ* **717** (Jul. 2010) 363–371, [arXiv:1006.2918](#) [[astro-ph.SR](#)]

- Rauch, T. & Werner, K., Non-LTE model atmospheres for supersoft X-ray sources, *Astronomische Nachrichten* **331** (Feb. 2010) 146
- Riess, A. G., Filippenko, A. V., Challis, P., et al., Observational Evidence from Supernovae for an Accelerating Universe and a Cosmological Constant, *AJ* **116** (Sep. 1998) 1009–1038, [astro-ph/9805201](#)
- Riffeser, A., Fliri, J., Gössl, C. A., et al., WeCAPP - Wendelstein Calar Alto pixellensing project I. Tracing dark and bright matter in M 31, *A&A* **379** (Nov. 2001) 362–373, [astro-ph/0104283](#)
- Ritter, H., Politano, M., Livio, M., & Webbink, R. F., The white dwarf mass distribution in classical nova systems, *ApJ* **376** (Jul. 1991) 177–185
- Rosswog, S., Kasen, D., Guillochon, J., & Ramirez-Ruiz, E., Collisions of White Dwarfs as a New Progenitor Channel for Type Ia Supernovae, *ApJ* **705** (Nov. 2009) L128–L132, [arXiv:0907.3196](#) [[astro-ph.HE](#)]
- Sala, G. & Hernanz, M., Envelope models for the supersoft X-ray emission of V1974 Cyg, *A&A* **439** (Sep. 2005) 1057–1060, [astro-ph/0502092](#)
- Sala, G. & Hernanz, M., Models for the soft X-ray emission of post-outburst classical novae, *A&A* **439** (Sep. 2005) 1061–1073, [astro-ph/0504353](#)
- Salpeter, E. E., The Luminosity Function and Stellar Evolution., *ApJ* **121** (Jan. 1955) 161
- Scalzo, R., Aldering, G., Antilogus, P., et al., A Search for New Candidate Super-Chandrasekhar-mass Type Ia Supernovae in the Nearby Supernova Factory Data Set, *ApJ* **757** (Sep. 2012) 12, [arXiv:1207.2695](#)
- Schlegel, D. J., Finkbeiner, D. P., & Davis, M., Maps of Dust Infrared Emission for Use in Estimation of Reddening and Cosmic Microwave Background Radiation Foregrounds, *ApJ* **500** (Jun. 1998) 525, [astro-ph/9710327](#)
- Shafter, A. W., Curtin, C., Pritchett, C. J., Bode, M. F., & Darnley, M. J., Extragalactic Nova Populations, in *Astronomical Society of the Pacific Conference Series*, Vol. 490, *Stell Novae: Past and Future Decades*, ed. P. A. Woudt & V. A. R. M. Ribeiro. 2014, 77, [arXiv:1307.2296](#) [[astro-ph.GA](#)]
- Shafter, A. W., Darnley, M. J., Hornoch, K., et al., A Spectroscopic and Photometric Survey of Novae in M31, *ApJ* **734** (Jun. 2011) 12, [arXiv:1104.0222](#) [[astro-ph.GA](#)]
- Shafter, A. W., Henze, M., Rector, T. A., et al., Recurrent Novae in M31, *ApJS* **216** (Feb. 2015) 34, [arXiv:1412.8510](#) [[astro-ph.SR](#)]
- Shafter, A. W., Hornoch, K., Ciardullo, J. V. R., Darnley, M. J., & Bode, M. F., Spectroscopic Observations of the Unusual Transient TCP J00452884+4154095 in M31, *The Astronomer's Telegram* **4503** (Oct. 2012) 1, ADS

- Shafter, A. W., Rau, A., Quimby, R. M., et al., M31N 2007-11d: A Slowly Rising, Luminous Nova in M31, *ApJ* **690** (Jan. 2009) 1148–1157, [arXiv:0809.1388](#)
- Shaviv, N. J., The theory of steady-state super-Eddington winds and its application to novae, *MNRAS* **326** (Sep. 2001) 126–146, [astro-ph/0008489](#)
- Shore, S. N., De Gennaro Aquino, I., Schwarz, G. J., et al., The spectroscopic evolution of the γ -ray emitting classical nova Nova Mon 2012. I. Implications for the ONe subclass of classical novae, *A&A* **553** (May 2013) A123, [arXiv:1303.0404](#) [[astro-ph.SR](#)]
- Silverman, J. M., Ganeshalingam, M., Li, W., et al., Fourteen months of observations of the possible super-Chandrasekhar mass Type Ia Supernova 2009dc, *MNRAS* **410** (Jan. 2011) 585–611, [arXiv:1003.2417](#) [[astro-ph.HE](#)]
- Sim, S. A., Röpke, F. K., Hillebrandt, W., et al., Detonations in Sub-Chandrasekhar-mass C+O White Dwarfs, *ApJ* **714** (May 2010) L52–L57, [arXiv:1003.2917](#) [[astro-ph.HE](#)]
- Skopal, A., Multiwavelength modelling the SED of supersoft X-ray sources I. The method and examples, *New A* **36** (Apr. 2015) 116–127, [arXiv:1401.1848](#) [[astro-ph.SR](#)]
- Skumanich, A., Time Scales for CA II Emission Decay, Rotational Braking, and Lithium Depletion, *ApJ* **171** (Feb. 1972) 565
- Sokoloski, J. L., Kenyon, S. J., Espey, B. R., et al., A “Combination Nova” Outburst in Z Andromedae: Nuclear Shell Burning Triggered by a Disk Instability, *ApJ* **636** (Jan. 2006) 1002–1019, [astro-ph/0509638](#)
- Soraisam, M. D. & Gilfanov, M., Constraining the role of novae as progenitors of type Ia supernovae, *A&A* **583** (Nov. 2015) A140, [arXiv:1401.6148](#) [[astro-ph.SR](#)]
- Soraisam, M. D., Gilfanov, M., Wolf, W. M., & Bildsten, L., Population of post-nova supersoft X-ray sources, *MNRAS* **455** (Jan. 2016) 668–679, [arXiv:1510.02649](#) [[astro-ph.SR](#)]
- Sparks, W. M., Starrfield, S., & Truran, J. W., CNO abundances and hydrodynamic models of the nova outburst. IV - Comparison with observations, *ApJ* **208** (Sep. 1976) 819–825
- Stark, A. A., Gammie, C. F., Wilson, R. W., et al., The Bell Laboratories H I survey, *ApJS* **79** (Mar. 1992) 77–104
- Starrfield, S., The accretion of solar material onto white dwarfs: No mixing with core material implies that the mass of the white dwarf is increasing, *AIP Advances* **4** no. 4, (Apr. 2014) 041007
- Starrfield, S., Sparks, W. M., & Truran, J. W., CNO abundances and hydrodynamic models of the nova outburst. II - 1.00 solar mass models with enhanced carbon and oxygen, *ApJS* **28** (Aug. 1974) 247–270

- Starrfield, S., Sparks, W. M., & Truran, J. W., CNO abundances and hydrodynamic models of the nova outburst. III - 0.5 solar mass models with enhanced carbon, oxygen, and nitrogen, *ApJ* **192** (Sep. 1974) 647–655
- Starrfield, S., Sparks, W. M., & Truran, J. W., Recurrent novae as a consequence of the accretion of solar material onto a 1.38 solar mass white dwarf, *ApJ* **291** (Apr. 1985) 136–146
- Starrfield, S., Truran, J. W., Sparks, W. M., & Kutter, G. S., CNO Abundances and Hydrodynamic Models of the Nova Outburst, *ApJ* **176** (Aug. 1972) 169
- Stetson, P. B., DAOPHOT - A computer program for crowded-field stellar photometry, *PASP* **99** (Mar. 1987) 191–222
- Stetson, P. B., On the growth-curve method for calibrating stellar photometry with CCDs, *PASP* **102** (Aug. 1990) 932–948
- Strope, R. J., Schaefer, B. E., & Henden, A. A., Catalog of 93 Nova Light Curves: Classification and Properties, *AJ* **140** (Jul. 2010) 34–62, [arXiv:1004.3698](#) [[astro-ph.SR](#)]
- Sturm, R., Haberl, F., Pietsch, W., & Greiner, J., Swift UVOT transient in M 31, *The Astronomer's Telegram* **5528** (Oct. 2013), [ADS](#)
- Sturm, R., Hofmann, F., Pietsch, W., & Greiner, J., Swift UVOT transient in M 31, *The Astronomer's Telegram* **5384** (Sep. 2013), [ADS](#)
- Sturm, R., Pietsch, W., & Greiner, J., Swift UVOT transient in M31, *The Astronomer's Telegram* **5669** (Dec. 2013), [ADS](#)
- Sullivan, M., Type Ia Supernovae and Cosmology, in *Lecture Notes in Physics*, Berlin Springer Verlag, Vol. 800, *Lecture Notes in Physics*, Berlin Springer Verlag, ed. G. Wolschin. 2010, 59–97
- Sullivan, M., Le Borgne, D., Pritchett, C. J., et al., Rates and Properties of Type Ia Supernovae as a Function of Mass and Star Formation in Their Host Galaxies, *ApJ* **648** (Sep. 2006) 868–883, [astro-ph/0605455](#)
- Taam, R. E. & Sandquist, E. L., Common Envelope Evolution of Massive Binary Stars, *ARA&A* **38** (2000) 113–141
- Tajitsu, A., Sadakane, K., Naito, H., Arai, A., & Aoki, W., Explosive lithium production in the classical nova V339 Del (Nova Delphini 2013), *Nature* **518** (Feb. 2015) 381–384, [arXiv:1502.05598](#) [[astro-ph.SR](#)]
- Tang, S., Bildsten, L., Wolf, W. M., et al., An Accreting White Dwarf near the Chandrasekhar Limit in the Andromeda Galaxy, *ApJ* **786** (May 2014) 61, [arXiv:1401.2426](#) [[astro-ph.SR](#)]

- Tang, S., Cao, Y., & Kasliwal, M. M., iPTF Discovery of an Apparent Nova in M31, *The Astronomer's Telegram* **5785** (Jan. 2014), ADS
- Tang, S., Cao, Y., & Kasliwal, M. M., Spectroscopic Confirmation of Three M31 Novae from iPTF, *The Astronomer's Telegram* **5852** (Feb. 2014), ADS
- Tang, S., Johansson, J., Tal, D., Cao, Y., & Kasliwal, M. M., iPTF Independent Discovery of an Apparent Nova in M31, *The Astronomer's Telegram* **5502** (Oct. 2013), ADS
- Tempel, E., Tuvikene, T., Tamm, A., & Tenjes, P., SDSS surface photometry of M 31 with absorption corrections, *A&A* **526** (Feb. 2011) A155, [arXiv:1012.3591](#) [[astro-ph.CO](#)]
- Thompson, T. A., Accelerating Compact Object Mergers in Triple Systems with the Kozai Resonance: A Mechanism for "Prompt" Type Ia Supernovae, Gamma-Ray Bursts, and Other Exotica, *ApJ* **741** (Nov. 2011) 82, [arXiv:1011.4322](#) [[astro-ph.HE](#)]
- Tomaney, A. B. & Crots, A. P. S., Expanding the Realm of Microlensing Surveys with Difference Image Photometry, *AJ* **112** (Dec. 1996) 2872, [astro-ph/9610066](#)
- Totani, T., Morokuma, T., Oda, T., Doi, M., & Yasuda, N., Delay Time Distribution Measurement of Type Ia Supernovae by the Subaru/XMM-Newton Deep Survey and Implications for the Progenitor, *PASJ* **60** (Dec. 2008) 1327–, [arXiv:0804.0909](#)
- Townsley, D. M. & Bildsten, L., Theoretical Modeling of the Thermal State of Accreting White Dwarfs Undergoing Classical Nova Cycles, *ApJ* **600** (Jan. 2004) 390–403, [astro-ph/0306080](#)
- Townsley, D. M. & Bildsten, L., Classical Novae as a Probe of the Cataclysmic Variable Population, *ApJ* **628** (Jul. 2005) 395–400, [astro-ph/0503556](#)
- Truran, J. W. & Livio, M., On the frequency of occurrence of oxygen-neon-magnesium white dwarfs in classical nova systems, *ApJ* **308** (Sep. 1986) 721–727
- Tuchman, Y. & Truran, J. W., Composition Influence upon the Core Mass-Luminosity Relation and Possible Implications for the Extinction Timescales of Classical Novae, *ApJ* **503** (Aug. 1998) 381–386
- van den Heuvel, E. P. J., Bhattacharya, D., Nomoto, K., & Rappaport, S. A., Accreting white dwarf models for CAL 83, CAL 87 and other ultrasoft X-ray sources in the LMC, *A&A* **262** (Aug. 1992) 97–105, ADS
- van Rossum, D. R., A Public Set of Synthetic Spectra from Expanding Atmospheres for X-Ray Novae. I. Solar Abundances, *ApJ* **756** (Sep. 2012) 43, [arXiv:1205.4267](#) [[astro-ph.HE](#)]
- van Rossum, D. R. & Ness, J.-U., Expanding atmosphere models for SSS spectra of novae, *Astronomische Nachrichten* **331** (Feb. 2010) 175, [arXiv:1001.1462](#) [[astro-ph.HE](#)]

- Verbunt, F. & Zwaan, C., Magnetic braking in low-mass X-ray binaries, *A&A* **100** (Jul. 1981) L7–L9, ADS
- Vilardell, F., Ribas, I., Jordi, C., Fitzpatrick, E. L., & Guinan, E. F., The distance to the Andromeda galaxy from eclipsing binaries, *A&A* **509** (Jan. 2010) A70, [arXiv:0911.3391](#) [[astro-ph.CO](#)]
- Walder, R., Folini, D., & Shore, S. N., 3D simulations of RS Ophiuchi: from accretion to nova blast, *A&A* **484** (Jun. 2008) L9–L12, [arXiv:0804.2628](#)
- Walterbos, R. A. M. & Kennicutt, Jr., R. C., Multi-color photographic surface photometry of the Andromeda galaxy, *A&AS* **69** (May 1987) 311–332, ADS
- Wang, B. & Han, Z., Progenitors of type Ia supernovae, *New A Rev.* **56** (Jun. 2012) 122–141, [arXiv:1204.1155](#) [[astro-ph.SR](#)]
- Warner, B., Cataclysmic variable stars., Cambridge Astrophysics Series **28** (1995), ADS
- Webbink, R. F., The evolution of low-mass close binary systems. I - The evolutionary fate of contact binaries, *ApJ* **209** (Nov. 1976) 829–845
- Webbink, R. F., Double white dwarfs as progenitors of R Coronae Borealis stars and Type I supernovae, *ApJ* **277** (Feb. 1984) 355–360
- Whelan, J. & Iben, Jr., I., Binaries and Supernovae of Type I, *ApJ* **186** (Dec. 1973) 1007–1014
- Williams, R. E., The formation of novae spectra, *AJ* **104** (Aug. 1992) 725–733
- Williams, S. C., Darnley, M. J., Bode, M. F., Keen, A., & Shafter, A. W., On the Progenitors of Local Group Novae. I. The M31 Catalog, *ApJS* **213** (Jul. 2014) 10, [arXiv:1405.4874](#) [[astro-ph.SR](#)]
- Wilms, J., Allen, A., & McCray, R., On the Absorption of X-Rays in the Interstellar Medium, *ApJ* **542** (Oct. 2000) 914–924, [astro-ph/0008425](#)
- Wolf, W. M., Bildsten, L., Brooks, J., & Paxton, B., Hydrogen Burning on Accreting White Dwarfs: Stability, Recurrent Novae, and the Post-nova Supersoft Phase, *ApJ* **777** (Nov. 2013) 136, [arXiv:1309.3375](#) [[astro-ph.SR](#)]
- Wood-Vasey, W. M. & Sokoloski, J. L., Novae as a Mechanism for Producing Cavities around the Progenitors of SN 2002ic and Other Type Ia Supernovae, *ApJ* **645** (Jul. 2006) L53–L56, [astro-ph/0605635](#)
- Woods, T. E. & Gilfanov, M., He II recombination lines as a test of the nature of SN Ia progenitors in elliptical galaxies, *MNRAS* **432** (Jun. 2013) 1640–1650, [arXiv:1302.5911](#) [[astro-ph.SR](#)]

-
- Woods, T. E. & Gilfanov, M., Emission-line diagnostics to constrain high-temperature populations in early-type galaxies, *MNRAS* **439** (Apr. 2014) 2351–2363, [arXiv:1311.1693](#) [[astro-ph.SR](#)]
- Woosley, S. E. & Weaver, T. A., Sub-Chandrasekhar mass models for Type IA supernovae, *ApJ* **423** (Mar. 1994) 371–379
- Yaron, O., Prialnik, D., Shara, M. M., & Kovetz, A., An Extended Grid of Nova Models. II. The Parameter Space of Nova Outbursts, *ApJ* **623** (Apr. 2005) 398–410, [astro-ph/0503143](#)

Acknowledgments

I am grateful to a number of people, who have contributed to the success of this thesis. The most important of all is my advisor Marat Gilfanov. I am thankful to him not just for the supervision of this thesis work, but also for inculcating in me during these three and a half years a more tangible and fulfilling approach to doing research. His support has been one of my strongest motivations during the difficult times I faced with my initial paper. I am grateful for the fact that he always gave me time whenever I wanted to discuss anything.

I thank Rashid Sunyaev for giving me the opportunity to be part of the High Energy Group at MPA, and more importantly, for being my official advisor. I am particularly grateful to him for his support for my project with the iPTF group at Caltech, giving me the opportunity to spend time at Caltech.

I would also like to thank former and present students in our group with whom I have had many fruitful discussions — Hai-Liang, Tyrone, Alex, Zhong-Li, and Filippos. I am extremely grateful to the administration staff at MPA, particularly Gabi, Sonja, Maria, Cornelia, and Stella, for being ever helpful in every matter — not just related to MPA, but even with finding an apartment in Munich.

Also thanks to the many scientific staff, postdocs, and other students at MPA, with whom I have interacted at some point or other. There are a particular few, whom I cannot help specifically mentioning here. Thanks to Xun, GuangXing, and Philipp for all the great times we spent together. Thanks to Richard, Nitya, Else, and Mei-Ling for being almost like a family to me, who have gone out of their way to help me with any problem that came up — from helping me debug codes to lending me their patient ears to nourishing me with fabulous home-cooked food. Last, and certainly not the least, thank you Niels for the mammoth help you have given me throughout these three years that has helped me shape this thesis. Thank you for being so patient with me; I cannot imagine this journey being so wonderful without you.